



**COMPARATIVE STUDY OF AERODYNAMIC INTERFERENCE DURING AFT
DISPENSE OF MUNITIONS**

THESIS

Matthew G. Burkinshaw, Captain, USAF

AFIT/GAE/ENY/07-J03

**DEPARTMENT OF THE AIR FORCE
AIR UNIVERSITY**

AIR FORCE INSTITUTE OF TECHNOLOGY

Wright-Patterson Air Force Base, Ohio

APPROVED FOR PUBLIC RELEASE; DISTRIBUTION UNLIMITED

The views expressed in this thesis are those of the author and do not reflect the official policy or position of the United States Air Force, Department of Defense, or the U.S. Government.

AFIT/GAE/ENY/07-J03

**COMPARATIVE STUDY OF AERODYNAMIC INTERFERENCE DURING AFT
DISPENSE OF MUNITIONS**

THESIS

Presented to the Faculty

Department of Aeronautics and Astronautics

Graduate School of Engineering and Management

Air Force Institute of Technology

Air University

Air Education and Training Command

In Partial Fulfillment of the Requirements for the
Degree of Master of Science in Aeronautical Engineering

Matthew G. Burkinshaw, BS

Captain, USAF

September 2007

APPROVED FOR PUBLIC RELEASE; DISTRIBUTION UNLIMITED

AFIT/GAE/ENY/07-J03

**COMPARATIVE STUDY OF AERODYNAMIC INTERFERENCE DURING AFT
DISPENSE OF MUNITIONS**

Matthew G. Burkinshaw, BS

Captain, USAF

Approved:

Raymond C. Maple, Lt Col, USAF (Chairman)

Date

Dr. Mark Reeder, (Member)

Date

Richard D. Branam, Maj, USAF (Member)

Date

Abstract

Based on forthcoming USAF needs, an investigation was launched to further the understanding of aft dispense of munitions in a high-speed environment. A computational fluid dynamics (CFD) study was performed followed by a wind tunnel experiment. The study consisted of a strut-mounted cone simulating a parent vehicle and a sting mounted cone-cylinder store situated directly behind the cone. The CFD modeled the test objects inside a supersonic wind tunnel in which the experiments took place. The CFD study consisted of evaluating a new strut designed to reduce asymmetry in the airflow aft of the cone. The CFD study also included predictions of axial loads acting on the store in various locations behind the cone. The experimental study consisted of implementing the new strut and introducing a miniature load cell for comparison to CFD load predictions. The CFD study indicated the newly designed strut increased the distance from the cone's base to the stagnation point by 27% and reduced transverse forces acting on the store by as much as 50% in two of the three locations evaluated. The experimental studies were successful in obtaining axial force coefficients that matched the CFD trend and were typically within 30% of the magnitudes. It was concluded that the load cell was generally adequate in measuring the axial loading on the store though its accuracy is less than that of a typical wind tunnel balance. The error trends indicate that the polymer store introduces the least amount of statistical error making it the most accurate representation of the results. Significant sources of error include transverse vibrations and axial buffeting observed in the wind tunnel tests.

Acknowledgements

I would like to express my sincere appreciation to my faculty advisors, Lt Col Maple and Dr. Reeder. Lt Col Maple sacrificed his time and effort to assist me with computational fluid dynamics, a considerable portion of this undertaking. His patience, guidance and support throughout the course of this thesis effort helped make it happen. Dr. Reeder's insight, experience and knowledge are greatly appreciated and contributed to the success of the experimental portion of this thesis effort. I would like to express my gratitude to these gentlemen for their patience, time, persistence, leadership and support.

Additional appreciation is extended to Mr. Rudy Johnson, AFRL/VAAI who sponsored this thesis project and Mr. John Hixenbaugh, the lab technician who helped make things happen. Without the effort of these individuals this thesis would not have happened.

Matthew Burkinshaw

"... for with God all things are possible."

Table of Contents

	Page
Abstract.....	iv
Acknowledgments.....	v
Table of Contents.....	vi
List of Figures.....	viii
List of Tables.....	xiii
List of Symbols.....	xiv
I. Introduction.....	1
1.1 Motivation.....	1
1.2 Objectives.....	2
1.3 Research Approach.....	6
1.4 Preview.....	6
II. Theory and Prior Research.....	7
2.1 Chapter Overview.....	7
2.2 Supersonic Flow Overview.....	7
2.3 Base Flow Overview.....	10
2.4 Experimental Methods.....	12
2.5 Computational Methods.....	19
2.6 Summary.....	24
III. Methodology.....	25
3.1 Chapter Overview.....	25
3.2 Planning and Preparation.....	25
3.3 Strut Design.....	29
3.4 Wind Tunnel Set-up.....	31
3.5 Computational Modeling.....	32
3.6 Experimental Procedures.....	41
3.7 Data Acquisition and Processing.....	51
3.8 Summary.....	67

	Page
IV. Results and Analysis Pertaining to the Strut.....	69
4.1 Chapter Overview.....	69
4.2 CFD Visualizations	69
4.3 Transverse Force Comparison.....	91
4.4 Cone and Strut	96
4.5 Cone Base Pressure	100
V. Results and Analysis of the Axial Loads	106
5.1 Chapter Overview.....	106
5.2 CFD Axial Force Coefficients.....	106
5.3 Experimental Axial Force Coefficients	109
VI. Conclusions and Recommendations	122
6.1 Chapter Overview.....	122
6.2 Conclusions	122
6.3 Recommendations	125
6.4 Summary.....	127
Appendix.....	128
Bibliography	152
Vita	156

List of Figures

	Page
Figure 1.1: AFIT wind tunnel test section	2
Figure 1.2: Wind tunnel inlets	4
Figure 2.1: Strut Disruption of Conical Shock	8
Figure 2.2: Depiction of Taylor-Maccoll.....	9
Figure 2.3: Diagram of “base conical flow”	11
Figure 2.4: Comparative reproduction of strut-mounted models	13
Figure 2.5: Depiction of Jung’s Experiment.....	15
Figure 2.6: Cone and Store Geometries	16
Figure 2.7: Jung’s PSP and Schlieren Images	17
Figure 2.8: Sample of Simko’s CFD-generated contour plots.....	20
Figure 2.9: Sahu’s cone and ejected store.....	22
Figure 3.1: Non-dimensionalization technique.....	25
Figure 3.2: Parent cone and store models	27
Figure 3.3: Sensotec Miniature Load Cell	28
Figure 3.4: Simko’s CFD analysis of swept strut	29
Figure 3.5: Comparative Synopsis of Original and New Struts.....	30
Figure 3.6: Depiction of AFIT Wind Tunnel System.....	31
Figure 3.7: Grids for redesigned strut, cone and store	33
Figure 3.8: Photos of Data Acquisition System.....	41
Figure 3.9: Support apparatus for load cell and extender rod.....	44

	Page
Figure 3.10: Photo of wind tunnel operating computer	45
Figure 3.11: Preliminary Configuration and result	46
Figure 3.12: Secondary Configuration.....	47
Figure 3.13: Tertiary Configuration	49
Figure 3.14: Photo of a typical experiment.....	50
Figure 3.15: Typical data plot recorded by oscilloscope	51
Figure 3.16a: 3-D Isometric view of Mach number	52
Figure 3.16b: 3-D Wind tunnel interior view of Mach number.....	53
Figure 3.17: Plot depicting ideal amplitude increase.....	55
Figure 3.18: Plot depicting less-than-ideal amplitude	56
Figure 3.19: Experimental Data post-processing procedure	57
Figure 3.20: Zoom-in of data plot generated by oscilloscope	61
Figure 3.21: Average Statistical Error (successive runs), longer extender.....	63
Figure 3.22: Standard Error of the Mean (single run), longer extender	66
Figure 4.1a: Original strut, stage 1, 2-D Side Contours of Mach number.....	71
Figure 4.1b: Original strut, stage 1, 2-D Top Contours of Mach number	71
Figure 4.2a: Original strut, stage 2, 2-D Side Contours of Mach number.....	73
Figure 4.2b: Original strut, stage 2, 2-D Top Contours of Mach number	73
Figure 4.3a: Original strut, stage 3, 2-D Side Contours of Mach number.....	75
Figure 4.3b: Original strut, stage 3, 2-D Top Contours of Mach number	75
Figure 4.4a: New strut, stage 1, 2-D Side Contours of Mach number.....	77

	Page
Figure 4.4b: New strut, stage 1, 2-D Top Contours of Mach number	77
Figure 4.5a: New strut, stage 2, 2-D Side Contours of Mach number	79
Figure 4.5b: New strut, stage 2, 2-D Top Contours of Mach number	79
Figure 4.6a: New strut, stage 3, 2-D Side Contours of Mach number	81
Figure 4.6b: New strut, stage 3, 2-D Top Contours of Mach number	81
Figure 4.7: Stage 1 Comparative Side Contours of Mach number	82
Figure 4.8: Stage 1 Comparative Top Contours of Mach number	83
Figure 4.9a: Original Strut, stage 1, side view colored by X-velocity vectors	84
Figure 4.9b: New Strut, stage 1, side view colored by X-velocity vectors	84
Figure 4.10: Stage 2 Comparative Side Contours of Mach number	85
Figure 4.11: Stage 2 Comparative Top Contours of Mach number	86
Figure 4.12a: Original Strut, stage 2, colored by X-velocity vectors	87
Figure 4.12b: New Strut, stage 2, colored by X-velocity vectors	87
Figure 4.13: Stage 3 Comparative Side Contours of Mach number	88
Figure 4.14: Stage 3 Comparative Top Contours of Mach number	89
Figure 4.15a: Original Strut, stage 3, colored by X-velocity vectors(m/s)	90
Figure 4.15b: New strut, stage 3, colored by X-velocity vectors (m/s)	90
Figure 4.16: Stage 3 comparison, side view colored by X-velocity vectors (m/s)	91
Figure 4.17: Plot of Y-component force imparted to store	92
Figure 4.18: Plot of Z-component force imparted to store	93
Figure 4.19: Comparative Plot of Y-component force imparted to store	94

	Page
Figure 4.20: Comparative Plot of Z-component force imparted to store.....	95
Figure 4.21: Pressure Sensitive Paint and CFD comparison of C_p	97
Figure 4.22: Original and New Strut comparison of C_p	99
Figure 4.23a: Original Strut, Base Pressure Plot ($x/D = 0.14$).....	102
Figure 4.23b: New Strut, Base Pressure Plot ($x/D = 0.14$).....	102
Figure 4.24a: Original Strut, Base Pressure Plot ($x/D = 0.80$)	103
Figure 4.24b: New Strut, Base Pressure Plot ($x/D = 0.80$).....	103
Figure 4.25a: Original Strut, Base Pressure Plot ($x/D = 1.61$).....	104
Figure 4.25b: New Strut, Base Pressure Plot ($x/D = 1.61$).....	104
Figure 4.26: Plot of Axial Force Coefficients	105
Figure 5.1: Axial Forces (C_F) from CFD for New Strut	107
Figure 5.2: Comparative plot of current and previous CFD results.....	108
Figure 5.3: Plot of Store-only Experimental Results.....	110
Figure 5.4: Time vs. Voltage Plot, Run 1 and 2 – short extender, metal store, 10psi ...	112
Figure 5.5: Time vs. Voltage Plot, Run 1 and 2 – long extender, metal store, 10psi	112
Figure 5.6: Time vs. Voltage Plot, Run 1 and 2 – long extender, poly. store, 10psi	112
Figure 5.7: Force Coefficients from Secondary Configuration	113
Figure 5.8: Force Coefficients from Tertiary Configuration	114
Figure 5.9: Cavity Analogy.....	116
Figure 5.10: CFD versus Experimental Data with Longer Extender.....	117
Figure 5.11: CFD versus Metal Store with longer extender	119

	Page
Figure 5.12: CFD versus Polymer Store with longer extender	119
Figure 5.13: CFD predictions and Tertiary Configuration	120
Figure 5.14: Data plot of CFD predictions and Tertiary Configuration	121

List of Tables

	Page
Table 5.1 Coefficients of Forces (C_F)	106

List of Symbols

a	Local Speed of Sound (m/s)
A_{ref}	Reference Area or equivalent cross-section area (m ³)
c	Speed of Sound (m/s)
C_D	Coefficient of Drag or Coefficient of Force
C_F	Coefficient of Force
C_P	Coefficient of Pressure
D	Diameter (mm)
γ	Gamma – ratio of specific heats
L	Standard Length (mm)
L_{ref}	Reference Length (mm)
M	Mach number
P	Pressure (Pa)
P_{∞}	Freestream (supersonic) Pressure (Pa)
P_{Tc}	Total pressure on cone (Pa)
R	Gas Constant (287.05 J/kg-K)
Re	Reynolds Number
T	Temperature (Kelvin)
T_C	Temperature on surface of cone (Kelvin)
t_i	Time (seconds)
T_{∞}	Freestream (Supersonic) temperature (Kelvin)
T_{Tc}	Total temperature of cone (Kelvin)

θ_s	Supersonic Shock wave angle (degrees)
θ_c	Cone half-angle (degrees)
u	Freestream velocity
V	Velocity (m/s) or Volts
W	Width (mm)
x/L	Non-dimensional designator for distance over length
y^+	Boundary Layer thickness

COMPARATIVE STUDY OF AERODYNAMIC INTERFERENCE DURING AFT DISPENSE OF MUNITIONS

I. Introduction

1.1 Motivation

Nations around the planet are developing their military and technological capabilities at an alarming rate. As terrorism and unorthodox combat methods continue to proliferate, a greater demand is placed on our military's intelligence, surveillance, reconnaissance and strike capabilities. The rapidly evolving battlefields and combat zones quickly diminish time-critical targets and opportunities. The concepts of stealth (i.e. F-117A), speed (i.e. B-1, F-22), altitude (i.e. B-2), range (i.e. B-52) and precision-strike (i.e. F-117A) currently exist in many parallel forms. Technological supremacy consists of engaging each of these parallel capabilities from a single or common platform. This common platform will be able to combine stealth, speed, altitude and precision-strike capabilities to produce "bombing anywhere on earth in less than two hours" [6].

Since the current methods of carrying and releasing stores for supersonic aircraft are not optimal, current research is working to develop and test an alternative design for store release at supersonic conditions [44]. One option involves releasing internal stores aft of the aircraft as opposed to the conventional underbody methods, thus avoiding ejection of a store through the aircraft shock-wave. Another advantage is avoiding ejection of a store through the shear layer generated from an open cavity (bomb bay) in high-speed flight regimes. The highly energetic shear layer formed by an open cavity can damage electronic components of a store [29, 37]. The advantages associated with aft

dispensing of munitions will maintain stealth, speed, altitude, range and precision capabilities [44]. The aft region of a supersonic or hypersonic vehicle consists of relatively benign separated flow providing a safer region for release and transition of stores away from the aircraft [3].

Finally, such a platform will well-satisfy the top priority General Lance Lord identified to the Senate Armed Services Committee on 16 March 2005 [39]. This top priority consists of advancing supersonic and hypersonic vehicles and their capabilities. This is the current vision for the near future of global reach capability and is expected to pave the way for further innovative research and development [6].

1.2 Objectives

The general objective of this study is to improve upon existing applicable research in the area of aft munitions dispense at supersonic conditions. Of the research reviewed, two researchers are highlighted because their studies are both based on the AFIT supersonic wind tunnel. Figure 1.1 depicts the AFIT supersonic wind tunnel and a

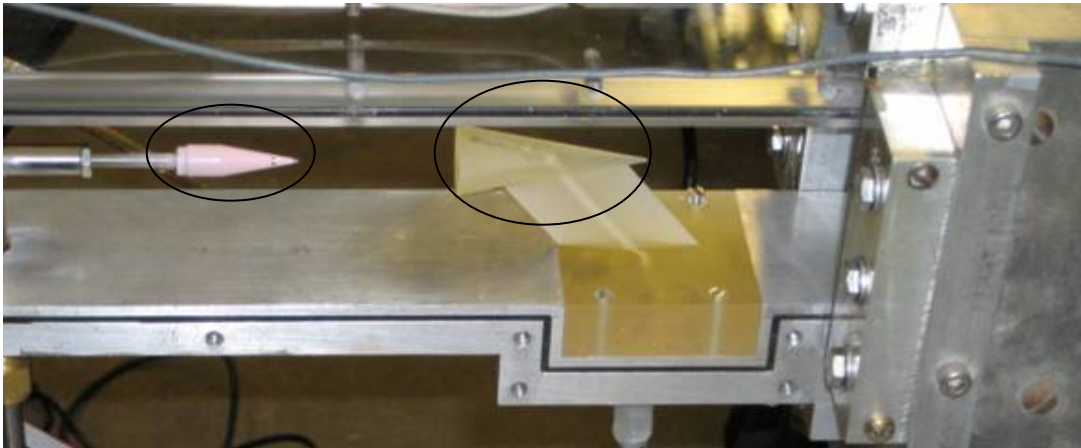


Figure 1.1: AFIT wind tunnel test section

generic representation of the previous experimental set-up which consisted of a cone-cylinder store placed behind a conical parent vehicle mounted on a swept diamond-shaped strut [21, 22]. In this study, pressure-sensitive-paint (PSP) was used to determine pressure coefficients and effects on the store. Schlieren images were used to provide visualizations of the supersonic flow field. In tandem, a study in computational fluid dynamics (CFD) was done to obtain load predictions on the store and flow field visualizations. Both studies identified important issues that need to be resolved. These issues include the mounting configuration for the parent vehicle, validating data obtained for the store and generating detailed visualizations associated with the findings.

Mounting Configurations One of the associated dilemmas encountered in this area of research is obtaining quality data without altering or disturbing the flow. Attaching any device to support or hold the test models will alter the flow field and disrupt supersonic phenomena such as shock waves. However, avoiding intrusive mounts or supports is fundamentally impossible due in part to the design of the wind tunnel itself. Studies performed by Dutton include the advantage of a 3-dimensional annular inlet nozzle that accommodated axis-symmetric mounting of the test object on a sting through the front as depicted in Figure 1.2 on the left. In these studies the wind tunnels were designed specifically for supersonic base flow experiments [7, 8, 15, 19, 23, 27]. The AFIT wind tunnel nozzle is depicted in Figure 1.2 on the right. The AFIT wind tunnel inlet nozzle is 2-dimensional and eliminates the option of using an axis-symmetric mount through the tunnel nozzle into the nose of the test object. Use of a support from

the rear of the test object is not possible due to the presence of the store directly aft of the test object [21]. As seen in Figure 1.1, the entire test section is enclosed by Plexi-glass

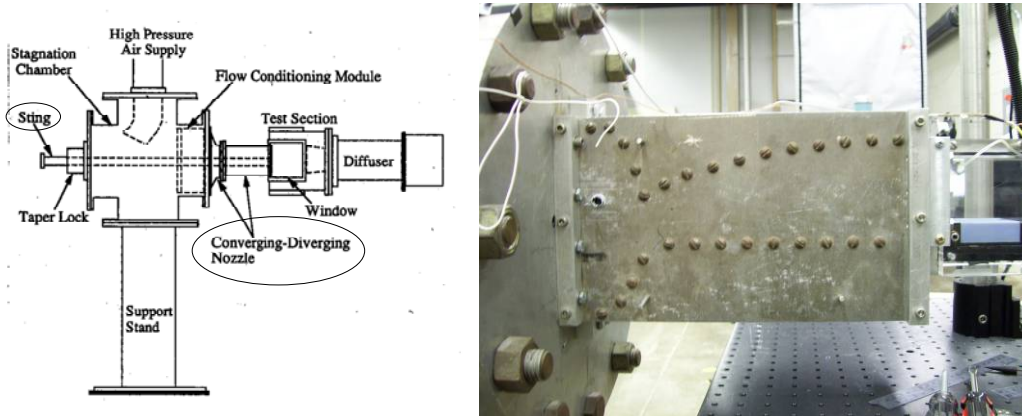


Figure 1.2: Wind tunnel inlets.

making it difficult, if not impossible, to attach the test object in any way other than via an underbody strut. Effectively, the underbody strut is the only valid option without redesigning the wind tunnel test section and inlet. An optimum strut should have negligible effects on the flow field adjacent to it. Although a comprehensive investigation on mounting methods is beyond the scope of this document, identification of a superior strut will contribute to resolving the parent vehicle mounting dilemma [21].

Aerodynamic Loads Currently there is limited experimental data available on the aerodynamic loads acting on an aft-released store. Such information is valuable in aft dispense predictions. In addition to the experiments performed in the AFIT wind tunnel, CFD was used to attempt to model the AFIT wind tunnel and predict the aerodynamic loads acting on the store [36]. Modifying the experimental set-up seen in Figure 1.1 in order to empirically obtain aerodynamic loads will generate quantifiable data for the store that will help validate CFD predictions for on-going research [21]. Typically in wind tunnel operations, a multiple-component balance is used to obtain aerodynamic data such

as lift and drag. Current research will use a much less expensive miniature load cell to obtain only the axial loads. This approach was expected to reduce cost, time, difficulty and complexity associated with data reduction.

Visualizations Previous researchers through the years have relied on a variety of visualization methods to identify specific areas of study. The advantage of CFD is various visualizations can quickly be generated for analysis and prediction. Although experimental visualizations present a more accurate picture based on real-world physics, the methods in which they are obtained can be intrusive or cumbersome. Generating visualizations will be very valuable for validation and prediction. The following objectives are identified to direct the scope of this research effort:

1. *Objective:* Reduce strut interference in the region aft of the cone.

Deliverable: A new strut from which to conduct research.

2. *Objective:* Determine and verify the axial loads acting on the store.

Deliverable: Comparative analysis of CFD predictions and experimental results.

3. *Objective:* Determine if the miniature load cell is suitable for obtaining axial load measurements.

Deliverable: Installation and evaluation of a miniature load cell balance for experimental determination of axial load data on the store.

The intent is to use the same or very similar parent cone and cone-cylinder store models circled in Figure 1.1. Appropriately modifying or updating various aspects of the set-up such as the struts, data recording devices or support mechanisms will aid in further study of the effects of aft store release from the parent cone at supersonic velocities. For

the remainder of the document the parent cone will be referred to as “cone” and the cone-cylinder store will be referred to as “store”.

1.3 Research Approach

The current effort includes both a computational and an experimental portion to complete the study. The commercial tools *Gridgen*, *SolidMesh*, *SolidWorks* and *Fluent* (version 6.2) were used for the CFD operations. The specific purpose of the CFD was two-fold: make predictions of the aerodynamic loads acting on the store at various locations aft of the parent cone, and generate flow visualizations for comparison and analysis of the strut. Once preliminary load predictions were accomplished via CFD, the AFIT wind tunnel was modified to experimentally obtain the aerodynamic loads acting on the store as modeled by the CFD.

1.4 Preview

Chapter 1 introduced the general topic and identified the objectives and present state of research. Chapter 2 presents some underlying theory, background discussions and a review of past research pertinent to the current objectives. Additionally, previous methodologies will be examined and evaluated. Chapter 3 will present the methods and procedures implemented in the current research. The details of the results will be presented and analyzed in comparative fashion in chapters 4 and 5. Chapter 6 will conclude the document with relevant findings and recommendations for further research.

II. Theory and Prior Research

2.1 Chapter Overview

The purpose of this chapter is to familiarize the reader with details of the relevant theory and research that has taken place to date. While many documents present information that is applicable to the current work in a general sense, only a select few documents present research and data directly applicable to the objectives outlined in chapter 1. These works will be referenced frequently to provide justification for decisions made and rationale for methods used. Highlighted items include overviews for supersonic and base flows, strut designs for base flow studies, experimental methods, and the use of CFD.

2.2 Supersonic Flow Overview

In current research, the phenomenon of supersonic base flow is of primary concern. Supersonic base flow is rooted in the effects of compressibility. Compressible flow is defined as flow that varies in density given the effects of temperature and pressure [2:4]. For both the CFD and the wind tunnel similar pressure ratios will be maintained in order to mitigate fluctuations in data caused by changes in density. This is done via the Perfect Gas Law identified in equation (2.1).

$$P = \rho RT \quad (2.1)$$

For a given pressure and temperature it is possible to calculate the density [2:13]. This important basic relation will be used in computing the experimental force coefficients from the raw measurements of force, pressure and temperature.

Naturally, the presence of the strut, cone and store will generate disruptions in the wind tunnel free stream flow. Of more specific concern are the shock and expansion waves and associated responses generated by these structures. Theory predicts a conical shock wave will propagate from the nose of the cone and an oblique shock wave will generate from the leading edge of the strut [2]. Jung [16], Simko [21] and de Feo & Shaw [36] demonstrate these shock waves propagating from the cone and support then reflect off the wind tunnel walls will not interfere with the near wake region directly aft of the cone where we intend to analyze the store. A more pressing concern is the direct interaction of the shock waves with the structures and the associated flow around them.

Figure 2.1 is a CFD Mach contour image produced by Simko [38]. It shows the support will interfere with the conical shock generated by the cone. Additionally, the support will interfere with the free stream air flow causing asymmetric flow in the tunnel, especially aft of the cone.

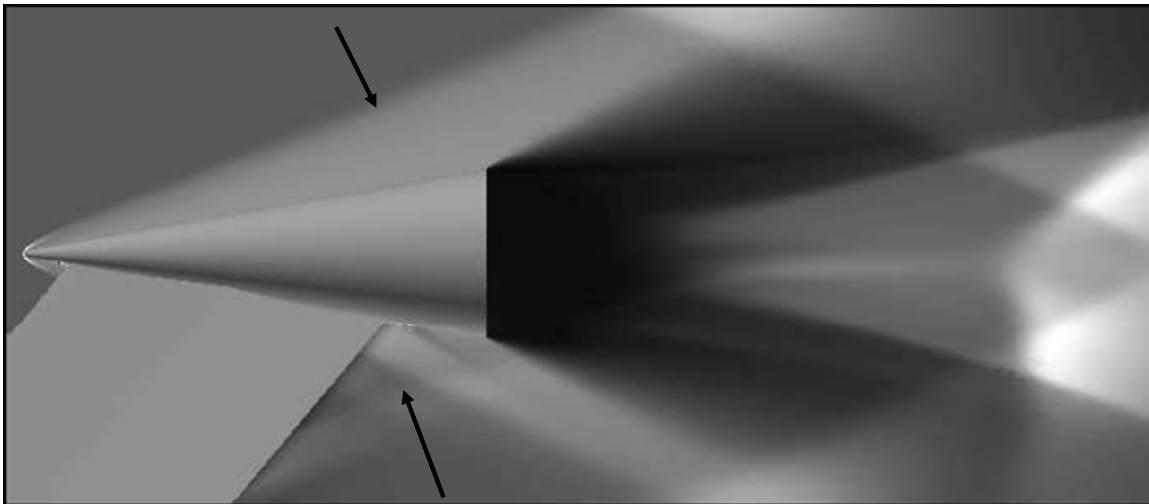


Figure 2.1: Strut Disruption of Conical Shock [38].

The basis for analyzing this comes from compressible supersonic flow theory.

The oblique conical shock generated by the cone can be analyzed using the Taylor-Maccoll equation (2.2).

$$\frac{\gamma-1}{2} [V_{\max}^2 - V_r^2 - (\frac{dV_r}{d\theta})^2] [2V_r + \frac{dV_r}{d\theta} \cot \theta + \frac{d^2V_r}{d\theta^2}] - \frac{dV_r}{d\theta} [V_r \frac{dV_r}{d\theta} + \frac{dV_r}{d\theta} (\frac{d^2V_r}{d\theta^2})] = 0 \quad (2.2)$$

Here, the irrotationality condition can be applied for axis-symmetric conical flow, which is the case for the CFD and wind tunnel experiments, neglecting the strut. The Taylor-Maccoll equation breaks out the radial and normal velocity components V_r and V_θ of the shock wave and their rates of change. This is done systematically from the shock wave, θ_s to the surface of the cone, θ_c . As θ is incremented, the associated value of $\frac{d^2V_r}{d\theta^2}$ is calculated until it reaches 0, at which $\theta = \theta_c$ which is the cone half-angle. A depiction can be seen in Figure 2.2. Pinpointing a numeric value is done using the Taylor-Maccoll

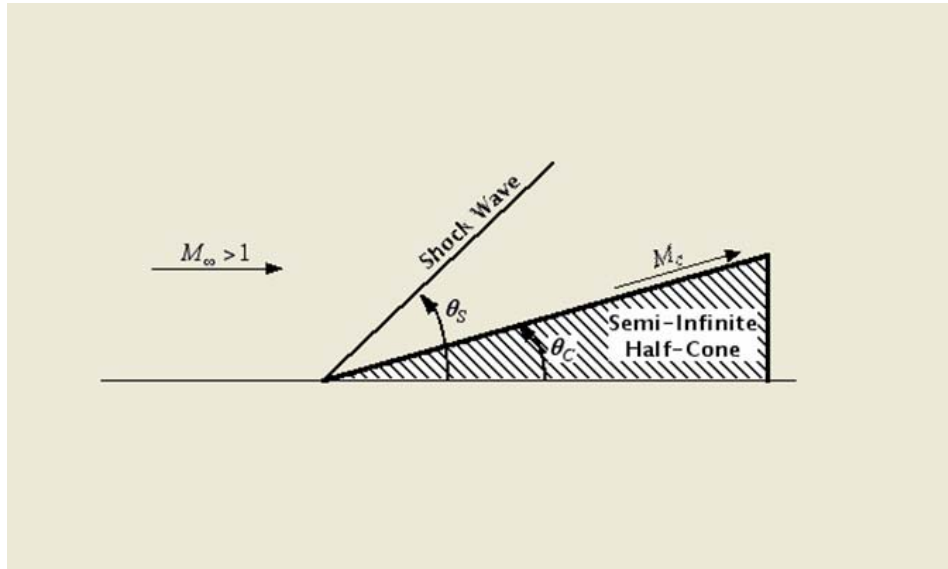


Figure 2.2: Depiction of Taylor-Maccoll [43].

equation, which must be solved numerically. To generate an aerodynamically sound strut, both the free stream flow and the conical shock wave will be accounted for in the

redesign of the strut. The benefits will be quantifiable in the changes seen in the base region.

2.3 Base Flow Overview

One of the objectives of current research is improving the cone's base region by introducing a new strut that will restore symmetry and structure to the flow field aft of the cone. A clear understanding of the base region is essential in order to comparatively determine which strut is better. As vehicles accelerate towards, through and then beyond the sound barrier, a significant amount of drag accumulates in three discernable forms: pressure or wave drag, viscous drag and base drag [10]. The base region of a high-velocity vehicle contains lower pressures with respect to the stagnation conditions and, as a result, generates base drag that can be as much as 67% of the total body drag experienced by the vehicle [15, 24, 35, 41]. This base drag can seriously impact range, trajectory, stability and base heating on the parent vehicle and these impacts will be imparted to a store released within the base region [15, 41]. At hypersonic speeds, these effects become the determining factors when studying aft dispense of stores from a parent vehicle [29].

A number of researchers have examined base flow dynamics. Figure 2.3 depicts a visual summary of the base flow dynamics as it applies to a cone at supersonic velocities [7, 8, 9, 10, 15, 16, 20, 24, 26, 27, 28, 30, 31]. After free stream air deflects through the conical shock wave, it traverses aft over the surface of the cone. Within the cone's boundary layer, viscous effects dominate and once the air reaches the base of the cone, it

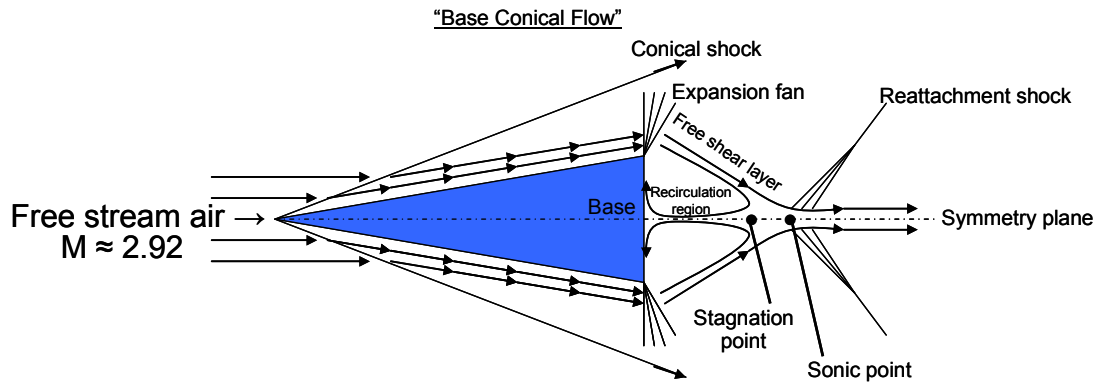


Figure 2.3: Diagram of “base conical flow”

accelerates through the expansion fans and into the separated recirculation region. Above the cone’s boundary layer, inviscid effects are prevalent. Air traverses the expansion fans into the free shear layer. The separated flow region (or near wake) typically includes the expansion fans, the free shear layer, the low pressure recirculation region, recompression shocks at the reattachment points, and concludes with the far or trailing wake [7, 8, 9, 15, 16, 30, 35, 42]. This separated flow region comprises the area of interest for prediction of the forces that will affect a separating store in supersonic flight [3]. The cases investigated will quantify the axial loads present on the store during various stages of aft departure from the parent cone. Previous research has identified and verified two related anomalies. The first is the presence of an adverse pressure gradient associated with the separated flow. The second is the presence of reversed flow with respect to free stream conditions [23, 21, 30, 35, 38]. The reversed flow is identified in Figure 2.2 as the recirculation region where the flow direction along the cone centerline is reversed with respect to free stream. It is expected that the adverse pressure gradient and reversed flow

produce small but quantifiable forces on the store as it emerges from the parent cone's base region [21, 36, 41].

2.4 Experimental Methods

Over the past 50 years several experiments have been performed to study base flow dynamics. A majority of experiments take place in a closed circuit supersonic blow-down style wind tunnel in which air is compressed and accelerated through the test section where the model is mounted. In most cases the wind tunnel is designed around the experiment in order to generate optimal conditions. Many studies, especially those performed by Herrin & Dutton, tend to focus on cylindrical afterbodies at Mach ~ 2.5 , with many at some angle-of-attack relative to the freestream airflow. Notable observations from these experiments include the use of various flow visualization techniques to locate the reattachment point [7, 8, 15, 17, 23].

Significant works completed by Blain Dayman include wire-mounted and free-flight models [11, 12, 13]. A free-flight model is ideal since intrusive mounting configurations are eliminated. Blain Dayman's studies consisted of mounting various spheres, cones, aerodynamic and blunt-bodies on thin wires. During the test, the wires were broken with an impulse load and the models were suspended in free-flight. In these studies, "spark" Schlieren images were taken before and after the models were released. This was very useful in optically demonstrating the interference the wires produced in the base region [12, 13]. Conclusions from these studies indicate as much as a 20% reduction in distance between the reattachment point and the base of the cone as a result of the wires [21:10]. A subsequent study performed by Dayman consisted of slender

cones mounted on tiny wires and subjected to hypersonic freestream conditions, again verifying that the wires significantly affected the accuracy of predictions in the base region [11]. Other experiments that pertain to mounting a test subject include Martellucci and Agnone's research with a 10° half-angle cone subjected to Mach 6 conditions and Burt, Miller and Agrell's research with an 8° half-angle cone-tipped cylinder (missile geometry) subjected to Mach 2 flow. Martellucci and Agnone performed studies with two configurations for mounting the cone in supersonic conditions. A depiction can be seen in Figure 2.4. Configuration A consisted of the strut mount and three 0.030-inches

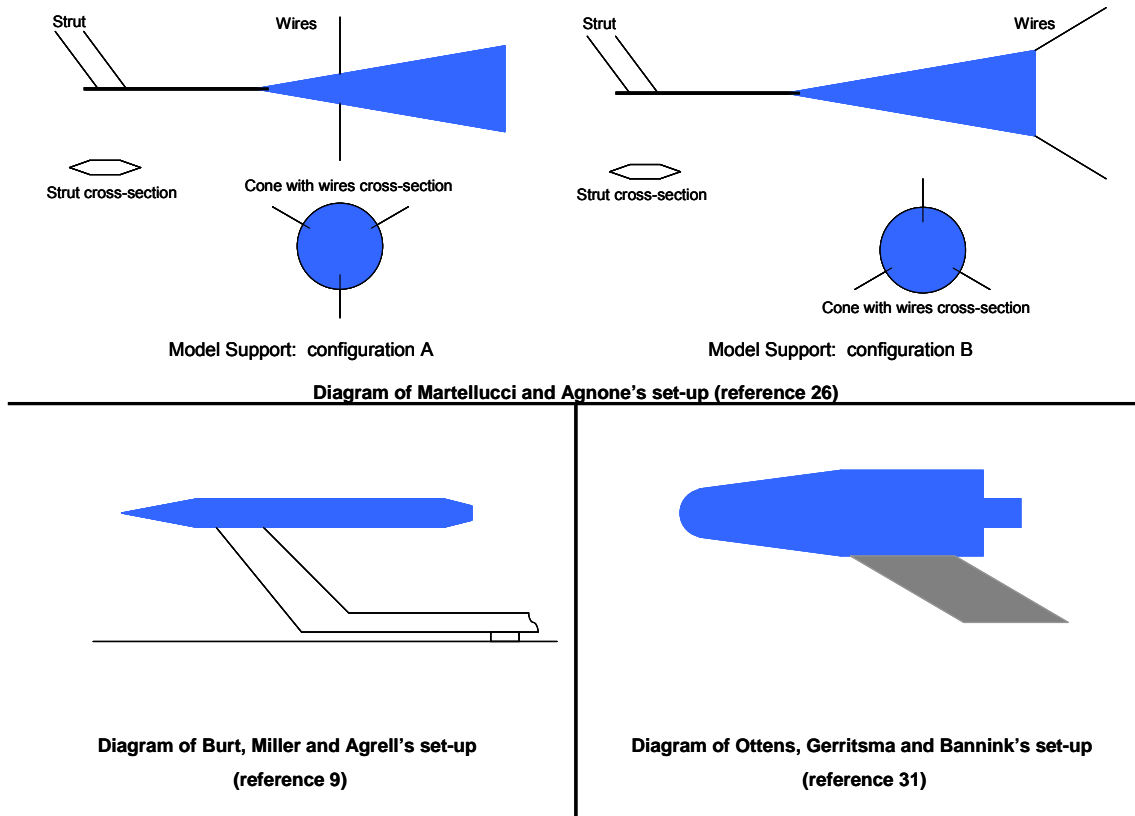


Figure 2.4: Comparative reproduction of strut-mounted models.

wires supporting the aft end of the cone. As expected, the wires in configuration A adversely affect the base pressure by drawing the reattachment point closer to the base of

the cone. This agrees with Dayman's findings. Configuration B consisted of "flattened" wires resembling smooth bands with sharp edges. This configuration was preferred as the sharp bands did not produce a wake and had less of an impact on the base region [26]. As depicted in the bottom left corner of Figure 2.4, Burt, Miller and Agrell later performed experimental studies of an "aero spike" vehicle simulating a rocket. Their primary intention was to study wake effects associated with an engine plume for CFD comparison. General observations indicated the strut adversely affected the base region however it was desired as the swept strut served to introduce bleed air into the wake region. A similar strut was analyzed in the CFD studies performed by Ottens, Gerritsma and Bannink. Conclusions from these studies indicate the swept strut reduced symmetry in the base region by impeding free stream airflow. This was acceptable as the studies focused on the wake influences of the engine plumes rather than symmetrical wake studies [9, 31].

Additional experimental studies of value are Dayman and Kurtz blunt fore body with a trailing drogue subjected to Mach 4, Eckert's studies with strut mounted aircraft and Jung's research in the AFIT wind tunnel with a 10° half-angle cone mounted on a strut with a smaller store mounted behind it [14, 17, 21, 22]. While Dayman and Kurtz obtained drag information on the trailing drogue, they used thin wires to attach the drogue to the aft of the parent vehicle. They did not verify any negative drag on the drogue and from Martellucci and Agnone's studies it can be concluded the drag accumulated by the wires in the base region will impact the drag associated with the drogue. Although Eckert provides interesting research in the way of sting mounted

models, most of his work deals with sub-sonic and transonic aircraft with more exotic mounting methods. Not surprisingly, the same difficulties arise in dealing with lift and drag interference as well as sting-model attachment dilemmas [17]. Of these studies performed, only Jung and Dayman & Kurtz include a following vehicle or store exposed to the base region of a parent vehicle. Naturally, Jung's work is most applicable and this study attempts to add to it.

The experiments that Jung performed are of particular interest for several reasons. Jung performed all his experiments in the Air Force Institute of Technology (AFIT) pressure-vacuum wind tunnel shown in Figure 2.5. This is important because the

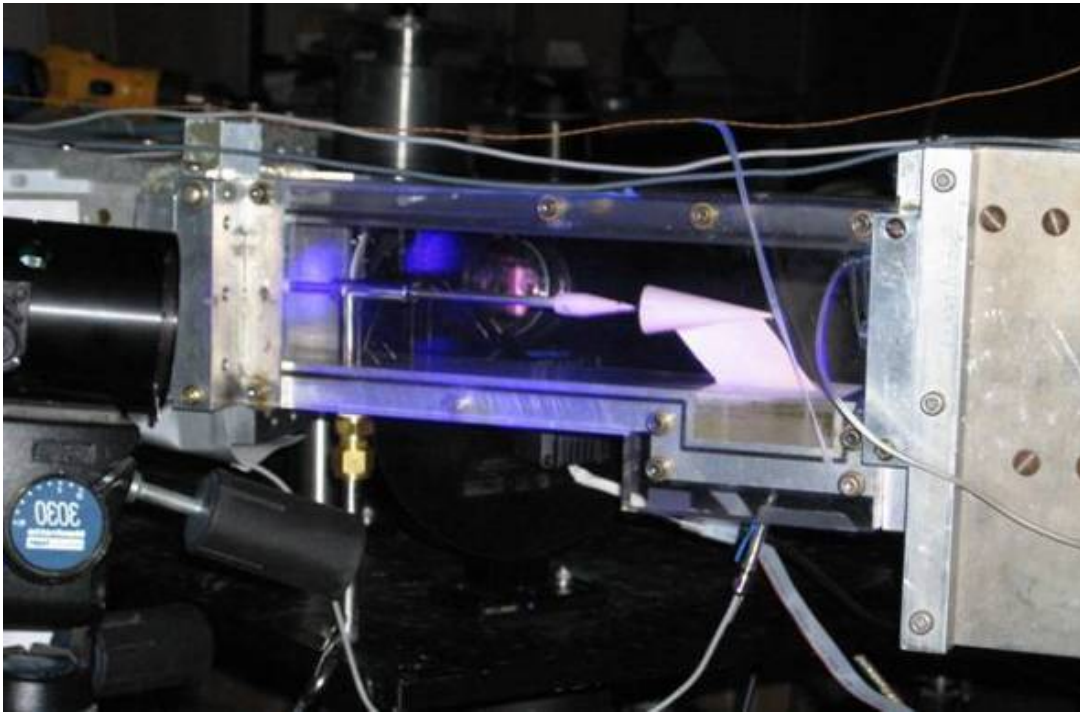


Figure 2.5: Depiction of Jung's Experiment [21].

follow-on studies presented and discussed herein were also performed in the same wind tunnel. The advantage is that this provides the potential for validation and verification of

experimental procedures, methodologies and results. Obviously the disadvantage is that potential exists for the same dilemmas to be encountered.

Jung investigated the method for mounting the parent cone. This is significant because one of Jung's preliminary conclusions was that the method of mounting the parent cone can drastically affect what happens in its wake. Additionally Jung revealed that the parameters of the AFIT wind tunnel limited selections for mounting the cone. A 40° forward-swept diamond strut similar to the one used by Jung was considered a potential option for current research. Jung and Simko concluded however, that there was an inherent problem in the forward-swept strut in that it turns the oncoming flow upwards into the parent vehicle and its wake region [21, 36].

The cone and store geometries used in this experiment were the same used by Jung. Both the parent cone and the store consist of a 10° half-angle cone. As can be seen in Figure 2.6, the store has a cylindrical base.

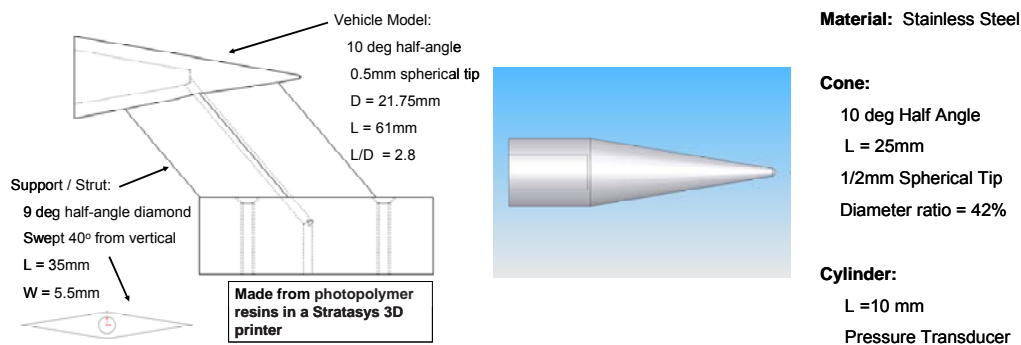


Figure 2.6: Cone and store geometries [22].

Jung used pressure-sensitive-paint (PSP) and Schlieren shadowgraph to identify pressure gradients, shock waves and reflections. These visualizations, seen in Figure 2.7,

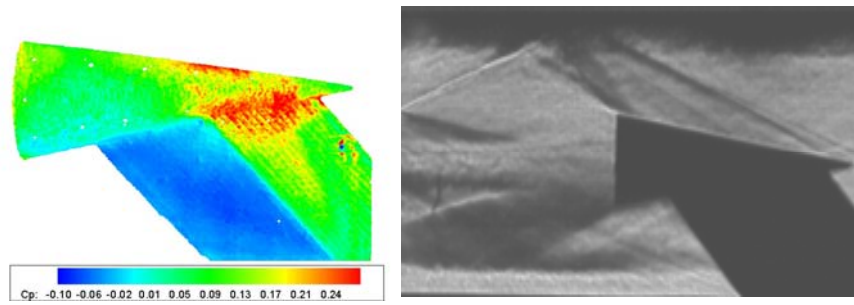


Figure 2.7: Jung's PSP and Schlieren images [21].

were significant in preliminary identification of the intrusive effects of the strut on the cone and the effects of the reflected shock waves in the cone's wake. Lastly, Jung investigated the effects of the store on the wake of the parent vehicle and the effects of the wake on the store.

Summarizing all the studies performed with respect to the influence of a support on the base region leads to the following conclusions:

1. Presence of a support draws the neck of the trailing wake and the reattachment point closer to the base of the mounted model.
2. The bluntness of the leading edge of a support (wire, strut, etc.) is coupled with the shock strength, which subsequently affects the level of intrusiveness.
3. A support oriented at an angle with respect to the oncoming flow can turn the flow, increasing its intrusiveness.

With the complexities associated in performing free-flight and strut-mounted studies no significant quantitative results or analyses were found that clearly identified the wind tunnel effects on the experimental models. Obvious qualitative impacts include the reflecting shock waves propagating down the tunnel and imperfections (nicks, scratches) present in the tunnel [21:30].

In the various studies, multiple techniques are used to obtain base pressure data and base flow field visualization. As mentioned earlier, Schlieren imaging was a common procedure used throughout the various studies to visualize base flow. All of Dayman's studies that were reviewed included Schlieren images of the model and its trailing wake, including the base region [11, 12, 13, 14]. Martellucci and Agnone and Boswell and Dutton also used Schlieren imaging and shadowgraph techniques to obtain visualizations. Laser Doppler Velocimetry (LDV) is another nonintrusive method that was used to obtain visualizations, velocity measurements and some turbulence information (intensity, kinetic energy) for the flow fields [7, 8, 15, 20, 26]. In addition to the LDV, in more recent studies Dutton used Mie scattering and oil droplets to generate visualizations. The Mie scattering is advantageous for generating images of shock waves and turbulent structures while the droplets were used to produce oil-streak visualizations to determine directional mapping of the fluid about the model [7, 20, 23]. Unfortunately, present options available for the AFIT wind tunnel are limited. Prior to Jung's experiments, Bjorge performed experiments to study the ejection of a store from a side or underbody cavity. Jung and Bjorge both employed Pressure-Sensitive-Paint (PSP) and Schlieren images to visualize the flow and pressure fields present during the experimental runs performed in the AFIT wind tunnel [5, 21]. While their studies were significantly different, the techniques used to generate flow visualizations were the same. Some of the experimental flow visualizations will be compared with results obtained in current research to verify shock reflections, pressure distributions and base pressures.

2.5 Computational Methods

In recent years, commercially available computational packages have contributed to research and development by providing flexibility in replicating and predicting experimental studies. Advantages of CFD include the ability to observe a variety of flow visualizations as well as access to numerical data such as aerodynamic loads [35]. Many studies similar to current research have been done at high Mach numbers with a variety of cone, cone-cylinder, rocket, missile, bullet and ogive shaped models [10, 24, 29, 30, 31, 32, 33, 35, 41, 42]. This can be attributed to the fact that with CFD it is much easier to make geometry and test modifications [35]. In addition to the array of rocket, missile and various cone-model studies, several computational studies were found that were of interest due to the geometries used, the CFD software used, the viscous-turbulence equations used and the replication of a parent vehicle with an associated aft store release.

The first study of particular interest is the study performed by The Delft University of Technology in the Netherlands. Ottens, Gerritsma and Bannink performed a computational study of a cylindrical-cone subject fixed to a forward-swept strut. This study was interesting because the geometry of the strut was similar to the one used in Burt, Miller and Agrell's research shown previously in Figure 2.4. In the paper, it is restated several times that the presence of the forward-swept support decreases the base pressure over the entire base [31]. This is in agreement with what was observed experimentally, in that it confirms that a forward swept support provides no advantage over a backward swept support in terms of the reattachment point. Also reiterated is the

idea that the effects of an underbody mounted support are significant to the data extracted from the experiment.

As referenced earlier, the only other CFD study encountered that analyzed the effects of the strut with respect to the base region and a store was Simko's [36]. Simko displayed several detailed images and vector plots of the flow field surrounding the objects of interest. A sample is presented in Figure 2.8. Simko utilized the Beggar code

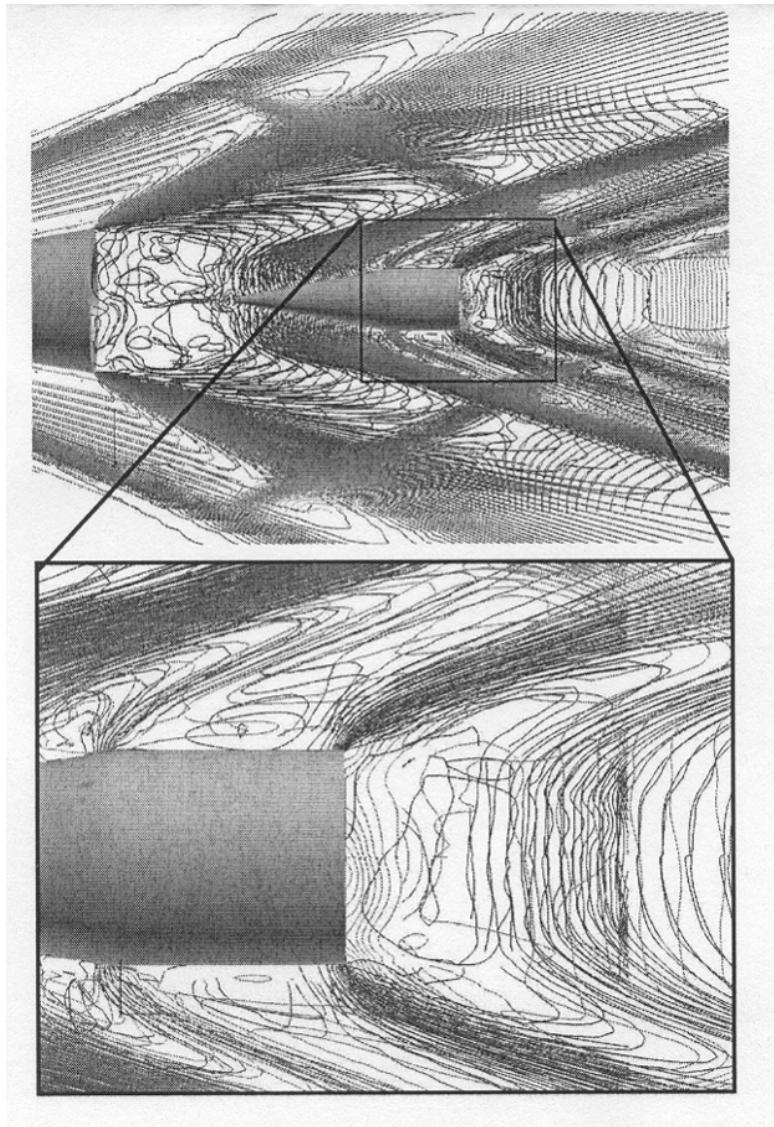


Figure 2.8: Sample of Simko's CFD-generated contour plots [36].

from the Air Force Seek Eagle Office to analyze models of the cone and store in free-flight and with the strut to make comparisons. For comparative purposes Simko evaluated the Spalart-Almaras (S-A), Baldwin-Lomax (B-L) and Detached Eddy Simulation (DES) models in his study. He concluded that when compared to empirical information, the S-A turbulence model did not perform as accurately when calculating base pressures as did the Baldwin-Lomax (B-L) and Detached Eddy Simulation (DES) models [19, 21]. Simko also concluded that the wind tunnel produced very little quantifiable change in the near wake but generated discernable changes in drag on the store outside the near wake. Significant changes in drag and base pressure calculations in the base region were attributed to the strut [38:78]. Additionally Simko was able to predict aerodynamic loads on the store that Jung could not obtain with his experimental set-up [21, 38].

The U.S. Army Research Laboratory investigated a CFD model in which a free-floating parent vehicle ejected a small store [41]. A Navier-Stokes, time-marching computational technique was implemented to study a missile-shaped conical parent vehicle at Mach 4.4 imparting an ejection force to a small store (see Figure 2.9). Sahu used an overset Chimera grid and his model predicted that in a dynamic ejection case the store will experience negative drag at small separation distances from the parent vehicle. In this case it is interesting to note that the store was much smaller than the parent vehicle and an impulse ejection force was applied. This is different from what is found in Jung's and Simko's cases where the store is nearly half the scale of the parent vehicle and is not imparted any ejection-type force within the set-up. Although the store dynamics and

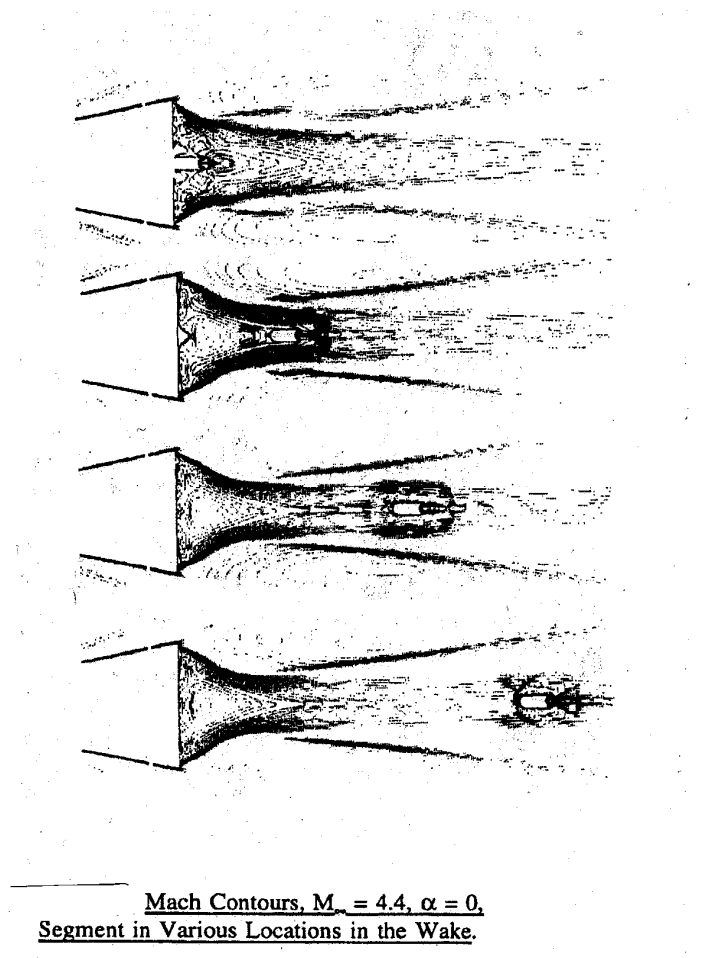


Figure 2.9: Sahu's cone and ejected store [41].

parent vehicle geometry are considerably different in Sahu's analysis, it appears that the characteristics of the base region are similar to what Jung and Simko found. The identification of a negative drag momentarily acting on the ejected store while it is in the near base region tends to coincide with Jung's and Simko's findings. This indicates that the effects of store size and applied ejection force may not significantly alter the effects of the base region on the store – namely a brief region of negative drag on the store. This also indicates that amid the various differences in the dynamic and static cases, they share a common finding in seeing the store experience a negative drag. It also indicates

that quantifying these effects in terms of axial loading on the store may shed more light on the subject.

De Feo and Shaw performed axisymmetric studies with the CFD package *Fluent* [16]. Although the axisymmetric studies did not include a store and are not suitably representative of the dynamics present in 3D strut-mounted studies, some information can be gained of *Fluent's* performance with a few turbulence models. De Feo and Shaw elected to implement the Spalart-Almaras model, the $k-\omega$ Shear Stress Transport (SST) adjusted model and the Reynolds Stress Model (RSM). Additionally they used pressure inlet and outlet boundary conditions for the wind tunnel inlet and exit respectively. Similar to Simko they concluded that the complexities of separated flow and recirculation at the base make Spalart-Almaras an inadequate model for accurate results. The $k-\omega$ SST model tended to overestimate the turbulent viscosity present in the base region. The RSM was deemed the most accurate; however it lacked robustness and took a significant amount of time to converge. Tucker and Shy attempted to validate the Jones and Lauder (1972) $k-\epsilon$ turbulence model with a cylindrical afterbody in Mach 2.46 flow. Realizing that the standard $k-\epsilon$ model tends to under-predict the distance from the base to the reattachment point they added a correction factor that tended to do the opposite. Using first, second and third order upwind schemes they concluded that both the standard and corrected $k-\epsilon$ models equivalently tend to over-predict the turbulent viscosity [42].

2.6 Summary

Important aspects of the project at hand include the supersonic phenomenon present; specifically the compressibility effects and the separated flow in the base region. Understanding these is essential for accurate comparisons between the CFD and experimentally derived information. Varying angle-of-attack, test object geometries and Mach number compose a majority of the studies performed. Inserting a store tends to require intrusive methods for mounting and recording data. This is due to the complexity of the base region. Introduction of CFD has contributed to the advancement of research including base flow visualizations, separating stores and model support analysis. Careful selection of the turbulence models can accommodate a more accurate solution that will better define the important aspects of the problem. While a variety of turbulence models have been applied and compared, the more popular choices include Detached Eddy Simulations (DES), and the $k-\epsilon$ and $k-\omega$ models, which have shown promise in giving meaningful information.

Naturally, it is near impossible to accurately and exhaustively model every aspect of the flow. Approximations and trade-offs will need to be made to generate a working CFD solution from which to base predictions of flow effects and axial loads on the store. CFD can be used to fill in or predict cases where the experimental studies may be weak and the experimental studies can be beneficial in substantiating the CFD predictions. Where applicable, past methods and procedures will be used or modified for the current problem. Where not applicable, the background discussed here will be used to arrive at the best decision.

III. Methodology

3.1 Chapter Overview

The purpose of this chapter is to describe in detail the procedures undertaken in this investigation. A methodical approach was taken to satisfy the objectives laid out in chapter 1. The chapter begins with basic preparation phases including the steps taken for redesigning the strut and the details of the AFIT wind tunnel. These are followed by the computational and experimental methods. Lastly, the specific configurations are introduced and the operational procedures are discussed.

3.2 Planning and Preparation

In the absence of a means to transition the store automatically, the snapshot approach provided the capability to retrieve detailed data at various store locations. This generated time-averaged CFD and experimental results. The actual snapshots were defined using a non-dimensional distance between the base of the cone and the tip of the store as depicted in Figure 3.1 [21]. Previous researchers used x/D where x is the

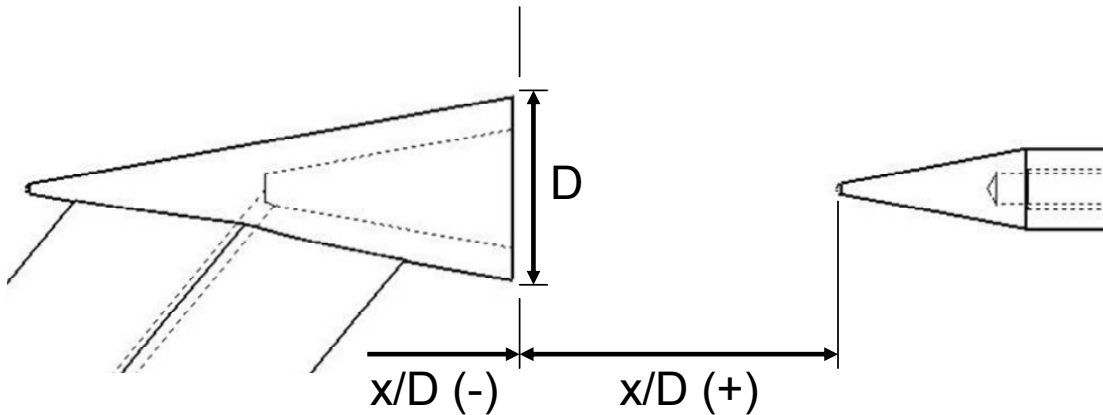


Figure 3.1: Non-dimensionalization technique.

horizontal distance between the tip of the store and the base of the cone and D is the diameter of the base of the cone. Recall from chapter 2 that $D = 21.75$ mm. Three locations were examined: $x = 3$ mm, $x = 17.5$ mm and $x = 35.0$ mm. Translating to x/D results in a stage 1 where $x/D = 0.14$, stage 2 where $x/D = 0.80$ and stage 3 where $x/D = 1.61$. A fourth stage where $x/D = 2.41$ was planned, but was later excluded when converged CFD solutions could not be obtained. The CFD solutions were limited to these three configurations. The experimental data was obtained from several stages to better capture the response of the loads on the store as it moves away from the cone.

Vehicle Models The CFD simulations were performed with a solid cone while the experiments in the wind tunnel were performed with a cavity cone to accommodate other experiments taking place. The actual models used are shown in Figure 3.2. The parent cone displayed on the left appears yellowish or vanilla in color and is attached to the strut and block. The cone measures 61 mm in length from tip to base. The outer diameter (base) measures 21.75 mm and the inner diameter of the cavity measures 16 mm. It is made of a lightweight polymer and is formed in a 3D *Stratasys* printer. The small whitish-yellow store on the far right was made the same way. Its dimensions are the same as the black metallic store. They measure 35 mm in length (10 mm for the cylindrical base and 25 mm for the cone). The base diameter of the store is ~9.2 mm. The nose of the cone models had a radius of 0.5 mm. In all models the cone was a 10° half-angle cone. Two notable differences in the two store models are their mass and surface roughness. Measured in a closed metric scale, the polymer store had a mass of 1.33 grams while the metallic store had a mass of 10.55 grams. Although the

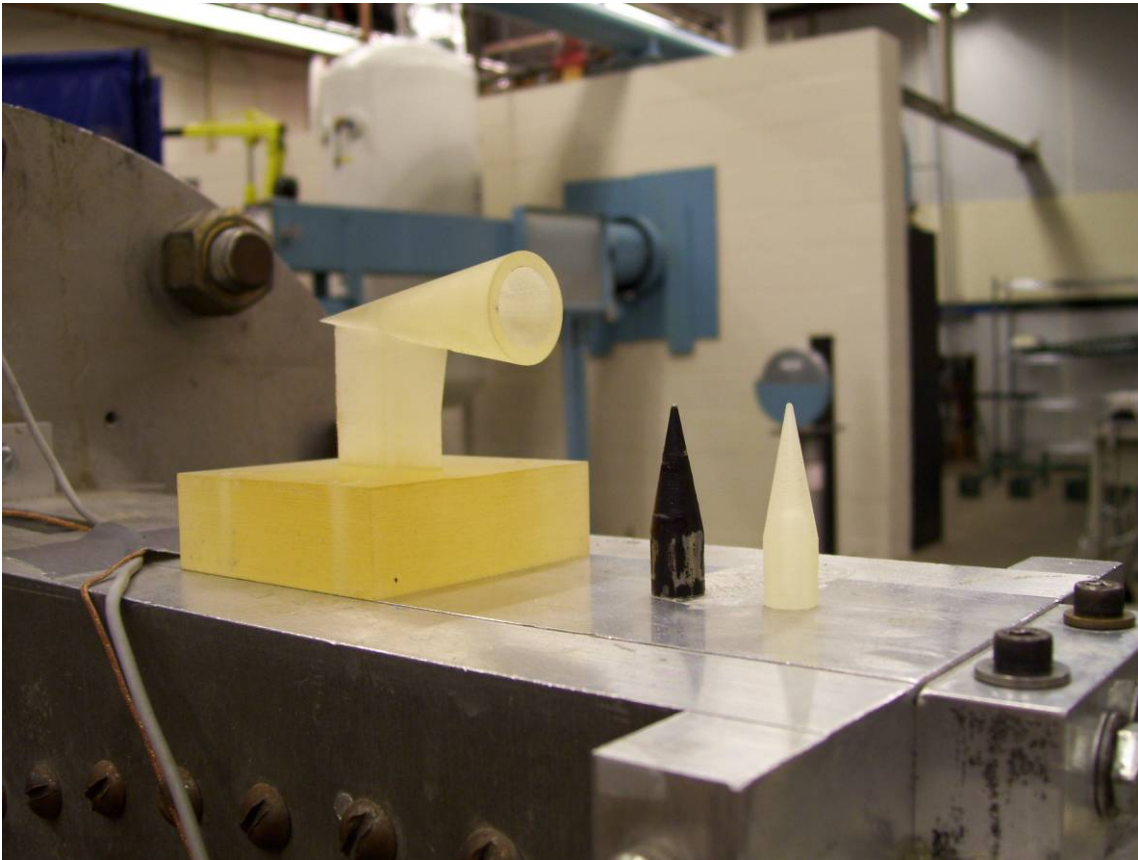


Figure 3.2: Parent cone and store models.

surface roughness may have some effect on the flow, it was assumed negligible with respect to the scope of the experimental research. Therefore no method was used to determine a coefficient of surface friction. The smoothed metal store was covered with a flat black enamel paint which began to rub off. The polymer store surface was noticeably rougher when compared via touch. Although they are not the exact same structures used in previous research they are 1:1 scaled replicas generated specifically for the experiments described herein.

Load Cell Unique from all previous studies reviewed was the use of a miniature load cell to determine force coefficients. Typically in a wind tunnel, force and moment measurements are taken with a multiple degree-of-freedom (DOF) balance that

supports the test object. Due to the small cross-sectional area of the wind tunnel, the cumbersome nature of implementing the balance and the availability of the load cell, the decision was made to incorporate the miniature load cell in place of the balance. A photo of the actual load cell used in the experimental portion is shown in Figure 3.3. The load



Figure 3.3: Sensotec Miniature Load Cell (Appendix C).

cell is produced by the *Sensotec* division of Honeywell Inc. The particular model used was the AL311. It features stainless steel construction and 1000-gram range with male and female threads to accommodate mounting. The load cell operates in like manner as a strain gage. The strain gage bridge is balanced to within two percent of the full rated output in millivolts. Within the active element, an electrostatic material receives input from the applied load. This input is measured as a change in electrical resistance. Since the current is known, the change in resistance can be recorded in terms of voltage via a multimeter. The calibration process equates a voltage range with a metric load in grams-force. Additional details and specifications of the load cell can be found in Appendix C.

3.3 Strut Design

Once decisions for the basic set-up and vehicle models were made, the strut was investigated. Previous research indicated that although the swept strut tended to reduce the strength of the oblique shock wave, it turned the oncoming flow up and into the bottom of the cone thus affecting the flow around and behind the cone [21, 36]. Figure 3.4 demonstrates the effect by using streamlines in a CFD model of the cone and strut.

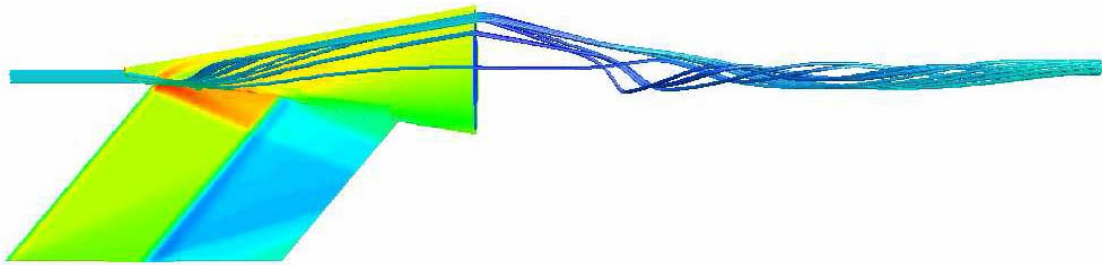


Figure 3.4: Simko's CFD analysis of swept strut [36].

Prior to any runs or experiments being performed, aerodynamic theory was revisited in order to generate a sound procedure for redesigning the strut. The fundamental idea with the redesign effort is to mitigate base flow disturbances and reduce the shock interaction between the cone and the strut by keeping the strut leading edge near normal to the oncoming flow. This requires a strut that projects at a right angle to the cone until it reaches the cone's shock. At the shock it must bend in such a way so as to remain normal to the undisturbed oncoming free stream flow.

For the cone's shock angle, the Taylor-Maccoll chart initially determined an angle range of 21-26 degrees for the given Mach number of 2.93 and the cone half-angle of 10° [2]. To narrow down the values, the Taylor-Maccoll differential equation was applied. Using a Taylor-Maccoll solver [43], it was determined that the conical shock angle was 22° . Subsequently, inviscid computational runs were completed and a 2-dimensional cut-

plane was made to examine the shock wave produced by the nose of the parent cone. A scaled printout and a protractor were used to verify the 10° half-angle cone and the predicted shock-wave angle (reference Appendix A). The 2-D shock wave angle was determined to be approximately $22^\circ \pm 1^\circ$. Therefore the 22.0° angle was selected based on the Taylor-Maccoll solver and was used to identify the bend in the strut. The redesigned strut shown in Figure 3.5 was initially generated in *Gridgen*, a commercial

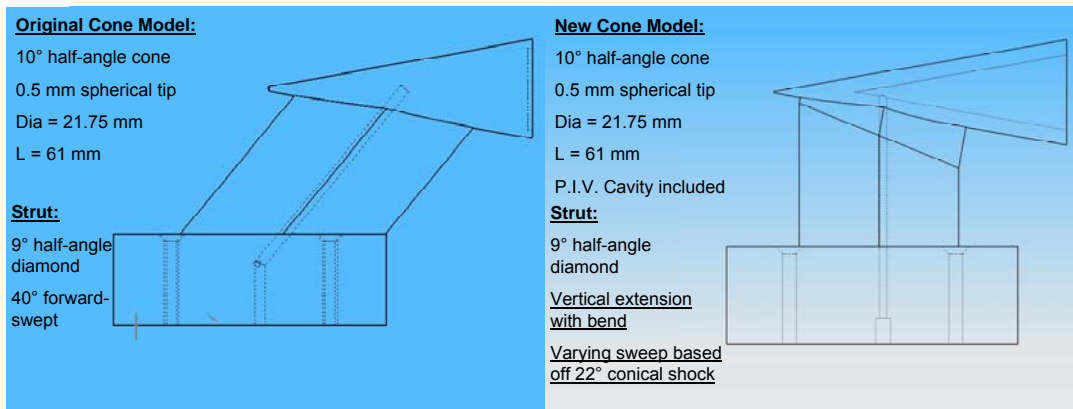


Figure 3.5: Comparative Synopsis of Original and new Struts.

grid generation package for CFD. Later the redesigned strut was drafted in *SolidWorks*. The *SolidWorks* model was imported into the database for the 3D *Stratasys* printer to generate a wind tunnel model. As seen in the figure, the base plate was included with the model. The cavity was incorporated into the cone with the redesigned strut to accommodate P.I.V. testing experiments performed in parallel with this study. The effect of the cavity on the predicted loads is considered negligible. Simko's axial force coefficients calculated by Detached Eddy Simulation (DES) for the wind tunnel at a Reynold's number of 3.9×10^8 showed less than a 4% difference as a result of the presence of the cavity [36].

3.4 Wind Tunnel Set-up

The AFIT wind tunnel is depicted in Figure 3.6. It is a closed circuit pressure-

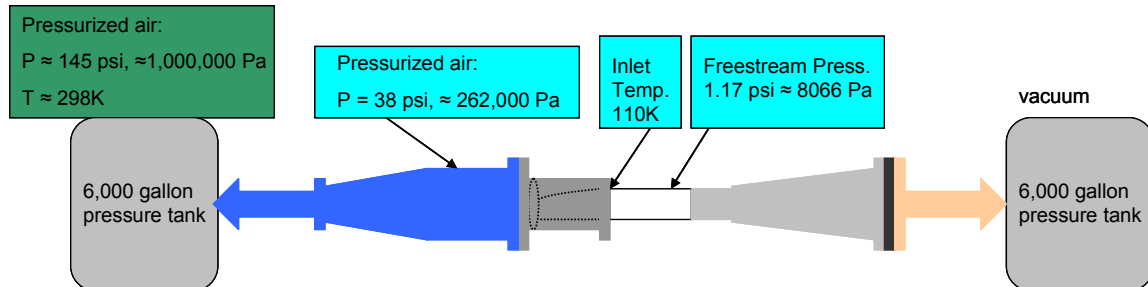


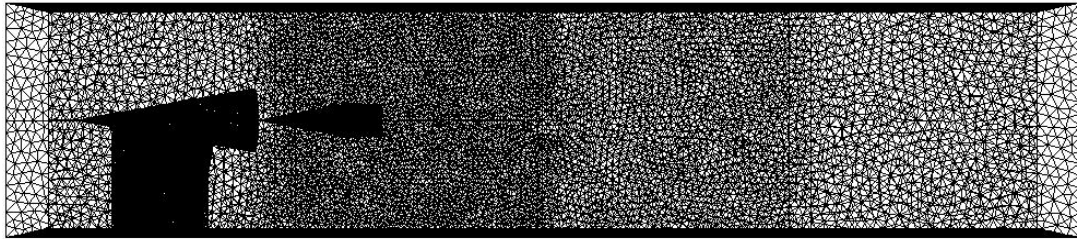
Figure 3.6. Depiction of AFIT Wind Tunnel System [21:22-23]

vacuum blow-down wind tunnel capable of achieving a freestream Mach of 2.93 based on the 2-D nozzle. A 6000-gallon pressure tank outside the building maintains air at a pressure of ≈ 145 psi. A regulator then reduces the pressure to feed the user-controlled stilling chamber. The stilling chamber, controlled manually by a reducing valve, provides the inlet stagnation pressure of ≈ 38 psi. As this air exits the stilling chamber, it passes through a honeycomb filter which straightens the flow prior to entering the asymmetric converging-diverging nozzle. Upon exiting the nozzle, free stream air enters the 2.5 x 2.5 x 12.0 inch test section comprised of Plexiglas windows that run the full length of the test section. Under typical operating conditions, the test section pressure is on the order of 1 Pisa with actual values dependent upon the stagnation pressure setting. As air exits the test section, it encounters the variable area diffuser and terminates with the vacuum tank, a 6,000 gallon tank that is outside the building. The variable area diffuser aids in the tunnel start-up. The vacuum tank is evacuated prior to initialization of the wind tunnel to reduce the pressure in the test section. This allowed for a lower stagnation pressure at inlet to generate the desired supersonic conditions [21].

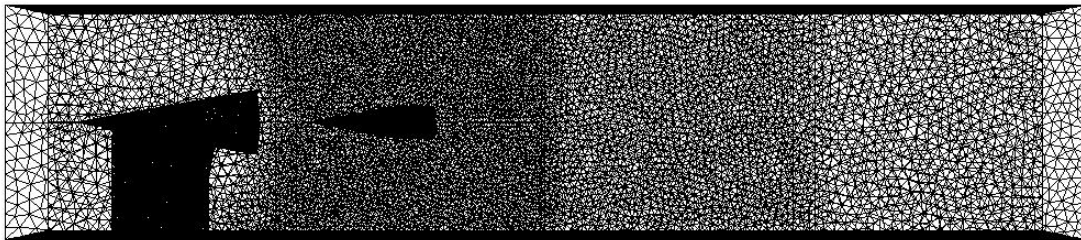
3.5 Computational Modeling

Due to the uncertainty of the loads, the computational modeling was performed first to predict the experimental loads and verify that the load cell would not be overloaded. The software package *Gridgen* was used to develop the database structures and create custom grids. The original strut, cone and store were imported from *SolidWorks* files available from a previous study [21]. The redesigned strut was initially developed in *Gridgen*. The walls of the wind tunnel were created around the strut, cone and base block entity with the actual wind tunnel dimensions.

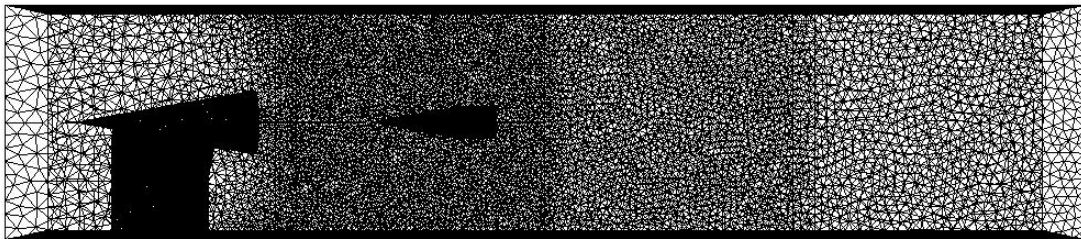
Mesh Generation Initially inviscid grids were generated to produce quick approximations for verifying the conical shock wave angle (reference Appendix A). This later proved useful in identifying areas where more grid points and tighter spacing would be necessary. Due to the complexity of the strut/cone shapes and the intersection angles of the cone and strut, an unstructured mesh was implemented in all cases. Once inviscid analysis was complete, the surface grids were imported into *SolidMesh* for development of the viscous boundary layers. The final grids are depicted in Figure 3.7. Based on a Reynolds number of 3.9×10^8 , the viscous grid spacing was selected to be 2×10^{-5} to ensure a wall $y^+ \leq 1.0$. The viscous boundary layer was only grown on the strut, cone and store. The strut, cone and store combination was selected to reduce the grid size and eliminate the added complexities of wall functions and high y^+ values at the tunnel walls. The sting and support apparatus used to support the store were omitted for simplicity and to obtain true store-only measurements. The default growth rate of 1.25 was selected to maintain adequate spacing in the viscous sub layer. Within the grids, all surfaces were assigned as



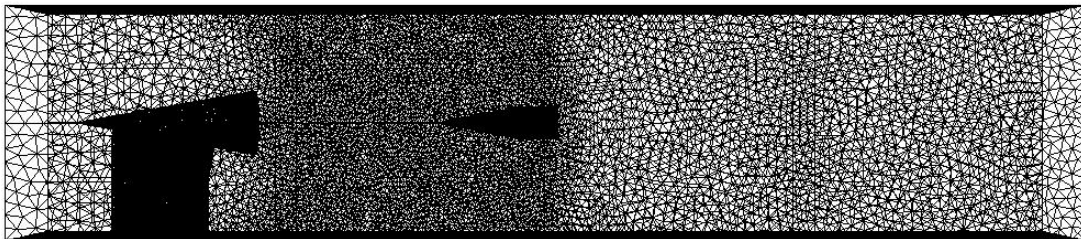
Stage 1: $x/D = 0.14$



Stage 2: $x/D = 0.80$



Stage 3: $x/D = 1.61$



Stage 4: $x/D = 2.41$

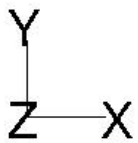


Figure 3.7: Grids for redesigned strut, cone and store.

solid walls except for the wind tunnel inlet and outlet areas. Once complete, the four viscous grids ranged in size from 3.9 to 4.2 million cells. Parallel computational processing was performed to accommodate the memory usage associated with the large grids. Several operations were performed to determine optimal processor allocation and adequate grid density to size relation. All grids were partitioned using Metis and Principal Axis and allocated to 4, 6, 8, 10 and 12 processors. The optimal performance was found partitioning by Metis and parallel computing with 8 processors. For the grids depicted in Figure 3.7, a converging computation required 8 processors and took approximately 5-6 days to complete.

Turbulence Modeling CFD involves computing numerical solutions to the governing equations of fluid flow. These governing equations are generated from the basic laws of fluid dynamics, namely the conservation of mass, momentum and energy. When separated and applied to a finite volume of fluid these equations constitute the discretized Navier-Stokes (N-S) equations, which govern the full spectrum of fluid motion. The N-S equations account for the flow dynamics and turbulence generated from complex flow involving high velocities and high Reynolds numbers. For high Reynolds number flows however, resolving the full range of turbulent length and time scales would require time and computing resources exceeding the capabilities of modern supercomputers. For current research and most engineering purposes the mean flow dynamics are adequate to obtain an accurate solution. For this the Reynolds Averaged Navier-Stokes (RANS) equations can be implemented. These consist of time-averaging the N-S equations to mitigate the effects of substantial fluctuations generated from

turbulence [1]. The RANS equations can incorporate various models to estimate the effects of turbulence. They are based on the equations of turbulent kinetic energy [45]. The turbulence eddy-viscosity models are typically categorized into one-equation and two-equation models based on the number of model parameters governed by partial differential equations [1]. Consequently it is understood that one-equation models are incomplete when relating a flow dimension to the turbulence length scale and two-equation models are complete when based on an equation for the eddy viscosity [45]. The model selected for the CFD portion of the study was the standard k- ϵ turbulence model for steady state from *Fluent*.

The k- ϵ turbulence model has been one of the more popular models in the past several years. It is similar to the k- ω model in that both tend to over predict turbulent viscosity. It features three defining equations (3.1, 3.2 and 3.3), five closure coefficients (3.4) and three closure functions (3.5).

$$\nu_T = C_\mu k^2 / \epsilon \quad (3.1)$$

$$\frac{\partial k}{\partial t} + U_j \frac{\partial k}{\partial x_j} = \tau_{ij} \left(\frac{\partial U_i}{\partial x_j} \right) - \epsilon + \frac{\partial}{\partial x_j} \left[(\nu + \nu_T / \sigma_k) \frac{\partial k}{\partial x_j} \right] \quad (3.2)$$

$$\frac{\partial \epsilon}{\partial t} + U_j \frac{\partial \epsilon}{\partial x_j} = C_{\epsilon 1} \frac{\epsilon}{k} \tau_{ij} \frac{\partial U_i}{\partial x_j} - C_{\epsilon 2} \frac{\epsilon^2}{k} + \frac{\partial}{\partial x_j} \left[(\nu + \nu_T / \sigma_k) \frac{\partial \epsilon}{\partial x_j} \right] \quad (3.3)$$

$$c_{\epsilon 1} = 1.14 \quad c_{\epsilon 2} = 1.92 \quad c_\mu = 0.09 \quad \sigma_k = 1.0 \quad \sigma_\epsilon = 1.3 \quad (3.4)$$

$$\omega = \epsilon / (C_\mu k) \quad \ell = (C_\mu k^{3/2}) / \epsilon \quad (3.5)$$

This defines the standard k - ϵ model as prescribed by Launder-Sharma (1974). Equation (3.1) defines the kinematic eddy viscosity equation, Equation (3.2) governs the turbulence kinetic energy, and Equation (3.3) governs the turbulent eddy dissipation rate. The k - ϵ model is typically used for duct or wall-bounded flows. Although it can encounter difficulties with separated flow, it handles it comparably with the k - ω model [45].

Solution Method Both the inviscid and the turbulent, steady state flow predictions were generated with *Fluent 6.2.16*. *Fluent* is a 3-dimension, double precision flow solver capable of accommodating parallel computing operations. This proved very valuable for the larger grids and complex flow patterns seen in base regions. The wind tunnel walls were designated as slip walls with no shear stress to compliment the lack of viscous wall grid spacing. The main expectation from the wall surfaces was an approximation of where the shock waves from the cone would reflect. It was decided that the pressure inlet and pressure outlet boundary conditions best suited and replicated the actual tunnel effects. This decision was also guided by successful axisymmetric base flow studies performed earlier [16]. Blow-down style wind tunnels typically rely on a user-specified inlet pressure and exit pressure to generate the desired supersonic conditions. The AFIT wind tunnel outlet is regulated by the vacuum system and the Mach number is regulated by the wind tunnel nozzle. This leaves the inlet pressure boundary condition as the primary method for coupling the CFD model with the wind tunnel operation. Doing the CFD and experimental work together and ensuring the inlet

pressure ratios are appropriately coupled should help mitigate variations between the predicted and empirically obtained loads.

The specified inlet total gauge pressure was the tunnel stagnation pressure of 38psi or 262,001 Pa. The supersonic gauge pressure was 1.17psig or 8066 Pa. All pressures were accounted for in terms of gauge measurements. Isentropic relations for an ideal gas relate velocity, total pressure and static pressure for a pressure inlet boundary condition [18]. This relation is demonstrated in Equation 3.6 obtained from *Fluent* [18: eq. 7.3-7]:

$$M \equiv \frac{u}{c} = \frac{u}{\sqrt{\gamma RT}} \quad (3.6)$$

where M is the Mach number equal to 2.93, u is the unknown velocity, c is the speed of sound for the experimental conditions of air ($\gamma = 1.4$, $R = 287$ J/kg-K) and temperature ($T_s = 110$ K). This generated a freestream velocity of approximately 614.5 m/s. Then, from equation (2.1) the ideal gas law can be rewritten as equation (3.7a):

$$\rho = \frac{P_s' + P_{op}}{RT} \quad (3.7a)$$

from equation 7.3-8 in the *Fluent 6.2* Users Guide. Since the operating conditions were zero, Equation (3.7a) becomes Equation (3.7b):

$$\rho = \frac{P_s'}{RT} \quad (3.7b)$$

where p_s' is the total pressure also referred to as the stagnation pressure and is equivalent to 1.17 psi or 8066 Pa, the freestream density can be calculated for the desired units of pressure. Finally, Equation 3.8 relates total and freestream temperature. Using the

equation and the inlet temperature of 110K and a freestream Mach of 2.93, the total temperature of the air in the pressurized tank outside of

$$\frac{T_0}{T} = 1 + \frac{\gamma - 1}{2} M^2 \quad (3.8)$$

AFIT is $\sim 298\text{K}$. Equation (3.8) reflects equation (7.3-9) in the *Fluent* User's Guide describing the relations used to deduce values for the initialization menu [18]. For the wind tunnel exit, the pressure outlet condition was selected with the gauge supersonic pressure at 8066 to reflect the wind tunnel pressure when the Mach number is 2.93.

Many difficulties were encountered attempting to obtain a converging solution. Convergence typically takes place when the variation between successive iterations is less than a specified amount. Iteration is the calculation of a solution for every point defined by the mesh or volume grid. The variation was truncated to 1×10^{-3} . As a result of the convergence difficulties, a few techniques were applied that fostered successful runs. The first was starting the flow at a slower initial velocity. *Fluent* provides the user with the option of initializing the flow to free stream conditions and then changing selected variables. Once the initialization was performed, the supersonic velocity was reduced. Doing so allowed the tunnel to accelerate to the supersonic velocity in similar fashion as the actual tunnel would. Periodic grid adaptation was applied on the pressure gradients to refine the grid in the shock wave and base regions during the iterative runs. The periodic grid refinement coupled with the accelerated wind tunnel velocity aided in better convergence of solutions with the first order upwind scheme. First order solutions were obtained for 3 of the 4 viscous grids with the redesigned strut. For unknown reasons, solutions for stage 4 would not converge to the specified threshold of 1×10^{-3} so it

was eliminated from the current study. The first three stages with both strut designs were run for 5,000 iterations at which convergence was seen with the declining residuals and leveling-off of the drag coefficient on the store. The first order solutions were then submitted to the second order solver where further convergence issues were encountered. Using the second order flow and turbulence solvers, not all grids saw complete convergence – where the residuals all dropped below the specified threshold. Drag history on the store, decline of residuals and number of iterations were comparatively used to determine acceptance of the solutions. Comparison with the first order results was also used, however data from the first order solution is typically questionable [1, 18]. In *Fluent* the first-order upwind schemes are best when applied to laminar duct flow in a structured mesh. Solutions involving complex geometries, shock waves and steep pressure gradients are usually best handled with unstructured grids which will tend to see numerical dissipation when a first order solver is used [1, 18]. The primary benefit of the first order solutions was to serve as an initial guess for the second order solution.

The coupled, implicit, 3-Dimensional, steady state solver was used for all cases. Coupling the energy and continuity equations allowed for simultaneous solving of the compressible flow equations. This resulted in more accurate and robust solutions in compressible steady state. Steady state was selected in order to approximate time-averaged solutions.

CFD Post-Processing CFD data was accumulated and various post-processing techniques were employed based on the options available in *Fluent*. Based on previous research, 2-dimensional cut planes were used to deduce information on the

symmetry of the flow over the cone, store and strut. The use of both side and top cut-planes provided information on the flow structure throughout the modeled environment. Various visualization profiles such as base pressure, Mach distribution, and velocity vectors were obtained for comparative analysis.

In addition to the visualizations, *Fluent* is capable of generating various reports and plots based on the selection of input data. Generation of force data was accomplished using the “force report” option in *Fluent*. Potential for error exists when inputting the incorrect reference values for area, length, etc. To eliminate the potential, a checklist control was used to ensure the correct data was entered and checked. Additionally, plots such as pressure coefficient distribution over a body required the appropriate dimensions, namely reference area, to be accurately logged. Reference values are calculated using the appropriate drop-down feature in *Fluent*, compared to the values recorded in previous experiments and verified with a hand calculator. Once the appropriate variables are set in the “reference values” drop-down menu, *Fluent* is able to integrate over surfaces and/or apply the built-in equations to numerically calculate the desired values. Generating the force and pressure coefficients and checking them analytically was significantly easier than the experimental data.

Other avenues for error or data degradation stem from the nature of CFD itself. Solution residuals and store drag trends were compared when determining convergence in order to reduce the possibility of obtaining poor or corrupt solutions. This was incorporated as a feedback mechanism after generating many solutions with convergence issues, fixing them, and regenerating them.

3.6 Experimental Procedures

After the computational runs generated solutions and predictions of the axial loads on the store, experimental testing began. A suitable data acquisition system was developed to accommodate the load cell and its means of rendering output.

Data Acquisition System The data acquisition system (DAS) consisted of the load cell, an in-line amplifier, a multimeter and an oscilloscope. Figure 3.8 displays the

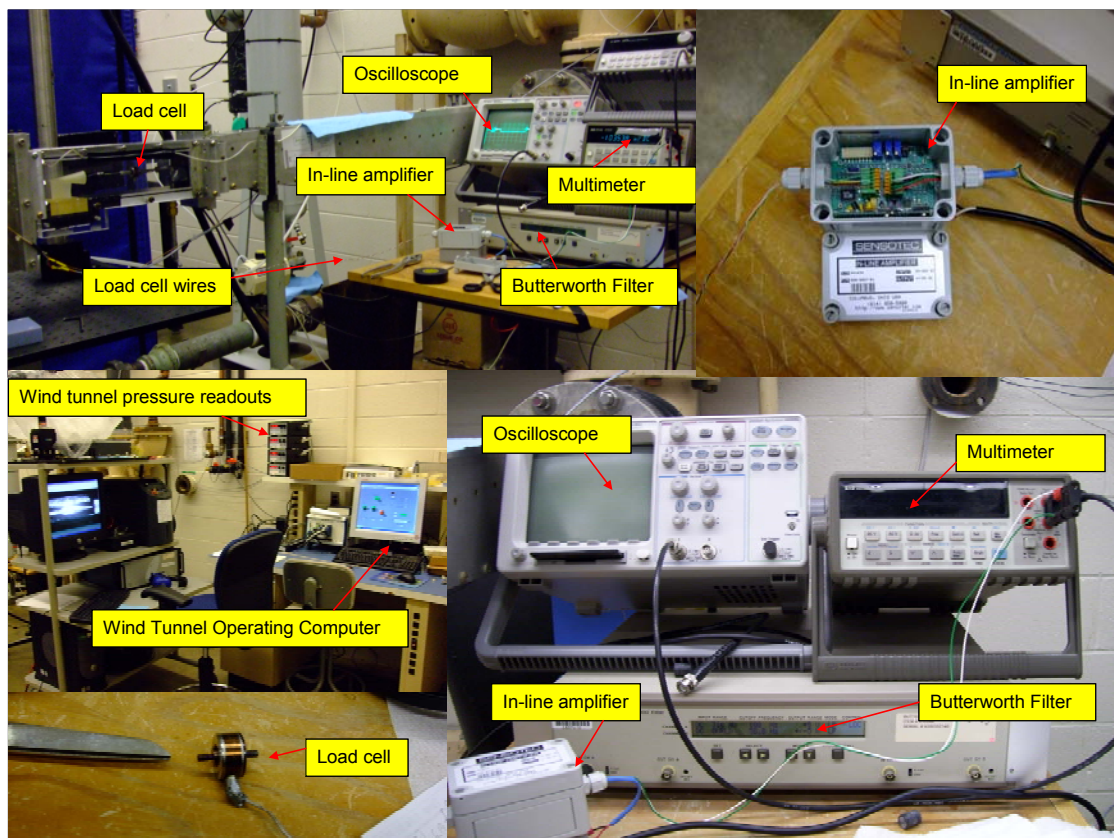


Figure 3.8: Photos of Data Acquisition System.

set-up. The load cell featured four fine-gauged output wires originating from its base. These were fed out of the wind tunnel via a protective support apparatus. The four wires connected directly into four terminal ports within the 5 Volt in-line amplifier. From the amplifier, a larger gauge wire with two leads carried the signal to the multimeter. The

multimeter displayed time-accurate output but did not contain the means to record the signal or monitor fluctuations in the load signal over time. Therefore, the oscilloscope was added to record time- accurate output of the load signal. Due to high-frequency noise evident in the recorded data, an attempt was made to incorporate a Butterworth filter. It could not adequately dampen the frequency response, however, without significantly altering the data. Therefore, the data acquisition system consists strictly of the load cell, amplifier, multimeter and oscilloscope.

Calibration and Initial Set-up Once assembled the DAS required calibration. Current calibration procedures and certificates for the oscilloscope and multimeter maintained by the technical support office at AFIT were followed. The miniature load cell and amplifier required joint calibration per the factory guidelines. A certificate of calibration (reference Appendix C) contained all the information for connecting, calibrating and interpreting the load cell output. The amplifier was connected to the multimeter which provided a digital readout of the voltage. Specification sheets from Honeywell state that calibration of a tension/compression load cell is only done in tension. Calibration was done by anchoring the load cell in a face-down position such that a pure tension load could be applied. The published non-linearity is $\pm 0.15\%$ (Appendix C). The initial tare readout was recorded from the multimeter. The amplifier was adjusted with a calibration factor of 1.0358 millivolts/Volt (mV/V) as specified in the calibration certificate (Appendix C). Using a fixed mass of 100 grams, the amplifier was adjusted internally until the multimeter readout stabilized and reflected the correct measurement for the 100 gram load. Taking

the difference from the initial reading and the final reading resulted in a ratio of 0.005 Volts per gram (V/g). The ratio can be verified from applying the 5V excitation across the 1000-gram load range ($5V/1000g = 0.005V/g$). Since the multimeter and oscilloscope displayed output in Volts, the ratio was applied to determine the load in grams-force.

Experimental Set-ups The scope of experimental operations included a preliminary, secondary and tertiary configuration. These three methods were examined in series to better validate the operability of the load cell. The test set-up required modification in order to accommodate the load cell. A photo of the modified store support can be seen in Figure 3.9. A tapped hole in the floor of the wind tunnel allowed previous experimenters to insert the support from which to mount the store. The steel angled-tube was altered to attach the load cell to the store and its sting. Appendix B contains the drawings submitted to the AFIT machine shop for fabrication and attachment of a brace. The angled steel tube was fitted with a brace on which the load cell could be bolted at the appropriate height. The appropriate height of the load cell was based on the position required to insert the threaded sting (extender) through the horizontally oriented steel tube segment and into the load cell. A nylon sleeve was tapped with the equivalent threading and fit inside the horizontal steel tube segment. This aided in reduction of moments and friction forces on the sting as it attached to the load cell. In addition to the 1000-gram load cell a 250-gram load cell was also examined. The 250-gram load cell

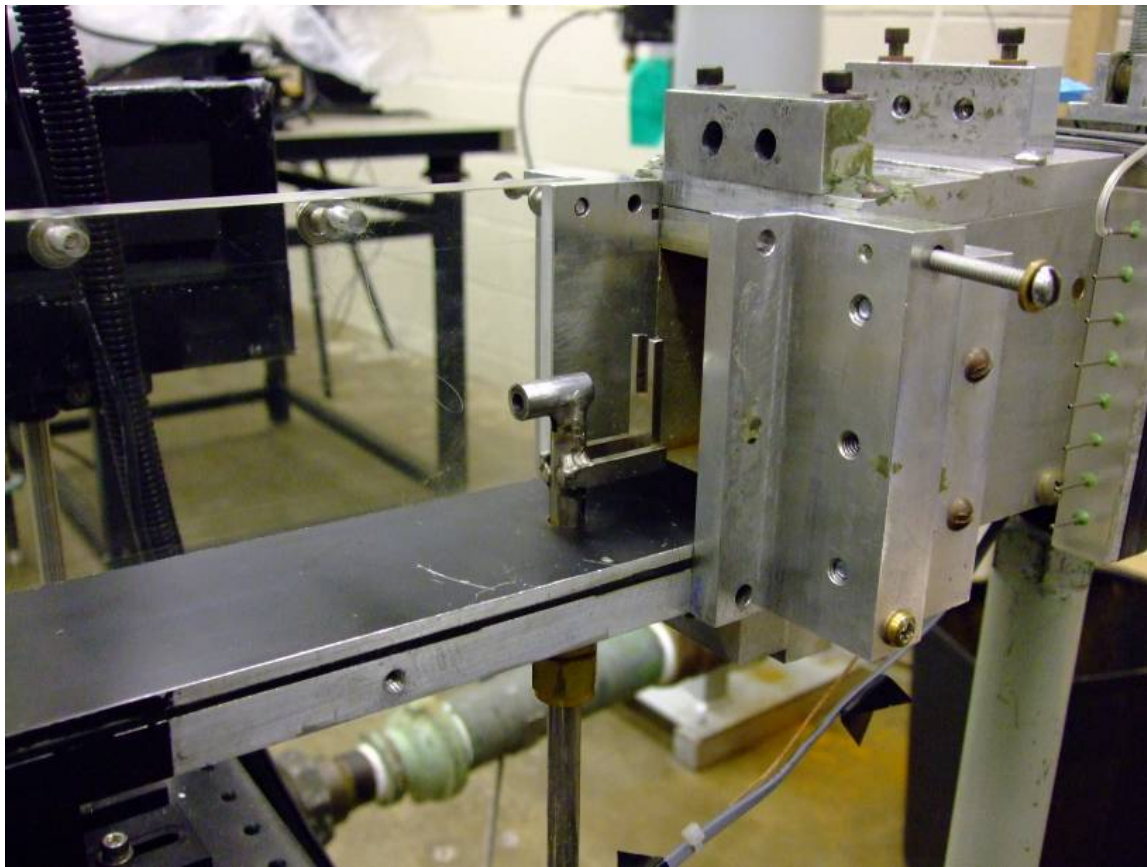


Figure 3.9: Support apparatus for load cell and extender rod.

introduced considerable hysteresis to the signal as a result of the weight of the extender rods and was replaced with the 1000-gram load cell. Once configuration modifications and adjustments were complete, the wind tunnel was operated in a methodical pattern using the interface shown in Figure 3.10. The control pressure is manually set at the beginning of a series of tests. The software established the pressure ratio required for the run. The higher the pressure ratio (control pressure/ vacuum pressure), the longer the wind tunnel can operate for a given run. For initial runs the control pressure was set as high as 34 psig. Later, the control pressure was reduced to 24 psig which resulted in a total operating pressure of 38 Pisa to match the CFD conditions.

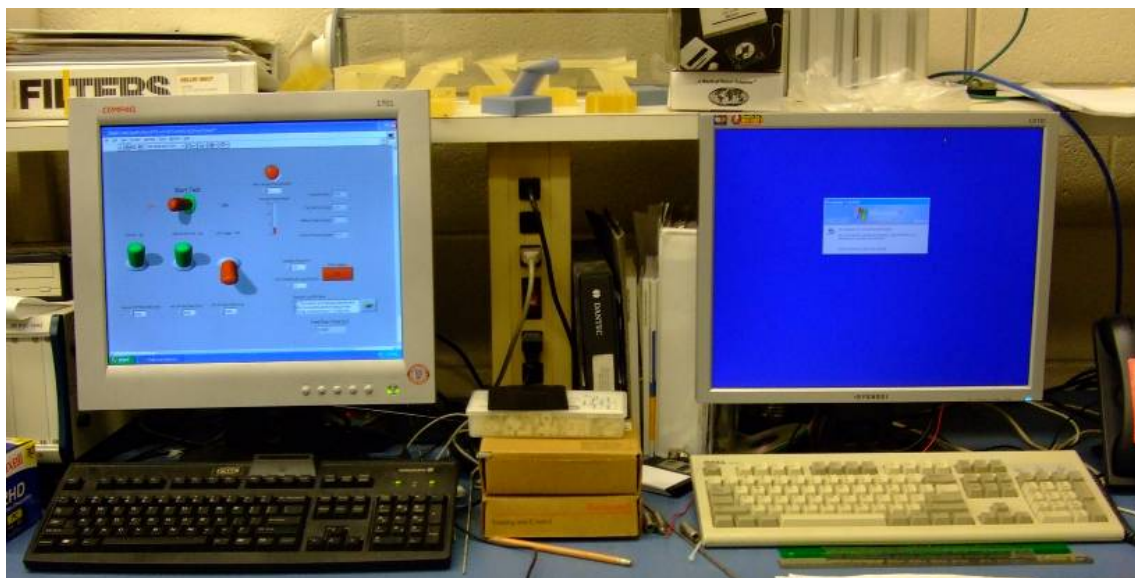


Figure 3.10: Photo of wind tunnel operating computer.

Preliminary Configuration Preliminary runs were conducted to examine the store, load cell, apparatus and new set-up. The preliminary configuration consisted of a #6-32 threaded rod threaded directly into the load cell on one end, and directly into the store's base on the other. Figure 3.11 features a diagram of the preliminary configuration and the resulting observations. The back of the load cell was bolted onto the upright brace. This secured the load cell and held it in the correct location, so that the extender rod would guide into the small horizontal tube with a smooth inner surface which served as a linear bearing, and thread into the stores' tapped base. Data was collected by observing the rapidly changing multimeter display in hopes of obtaining a maximum value that could be recorded. The preliminary runs were discontinued primarily because severe oscillations occurred. As the tunnel velocity settled into Mach 2.92 flow, very minor vibrations of the store tip could be observed for approximately one to two seconds.

Shortly thereafter the vibrations transitioned to severe oscillations of the entire store as depicted in Figure 3.11. These oscillations saw the store rapidly moving in and out of the base region of the cone and continued until the wind tunnel began its shut-down

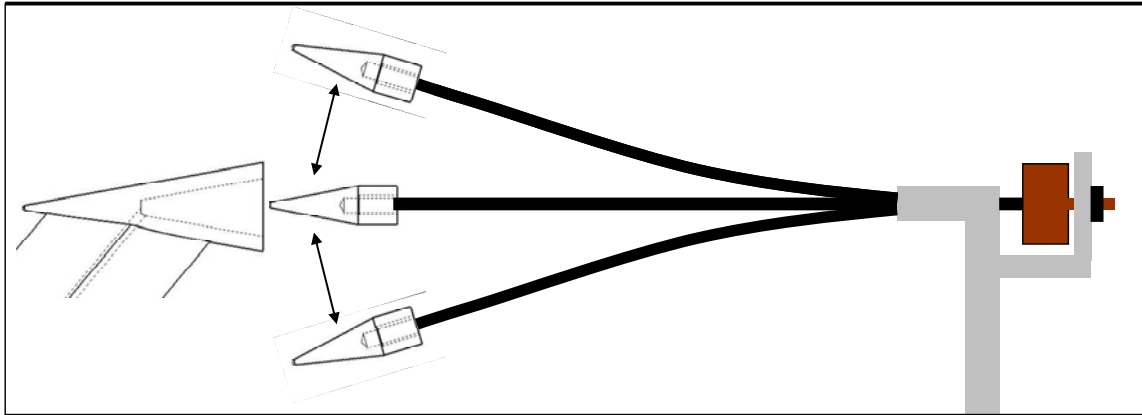


Figure 3.11: Preliminary configuration and result.

sequence. When the wind tunnel began its shut-down sequence and the oscillations began to dampen out, it was noticed during three of the four tests that the store and extender began to unscrew from the load cell. Fortunately the wind tunnel completed its shut-down before the extender unscrewed far enough to separate from the load cell. The brief couple of seconds of minor vibrations created the window of data acquisition when the multimeter display was visually monitored and recorded.

Secondary Configuration As a result of the undesirable conditions observed in the preliminary configuration, the data acquisition system was upgraded with the oscilloscope and the test set-up was modified as depicted in Figure 3.12. The significant changes included adding the oscilloscope to the DAS, moving the load cell out of the brace and securing it between the support rod and the extender rod connected to the store. This allowed the load cell to move with the store when changes in the x/D location

were made. At this point a new 1000-gram load cell was acquired and appropriately calibrated according to factory specifications. The original load cell was removed due to failure from a suspected short in the wires when they were cut and re-soldered to

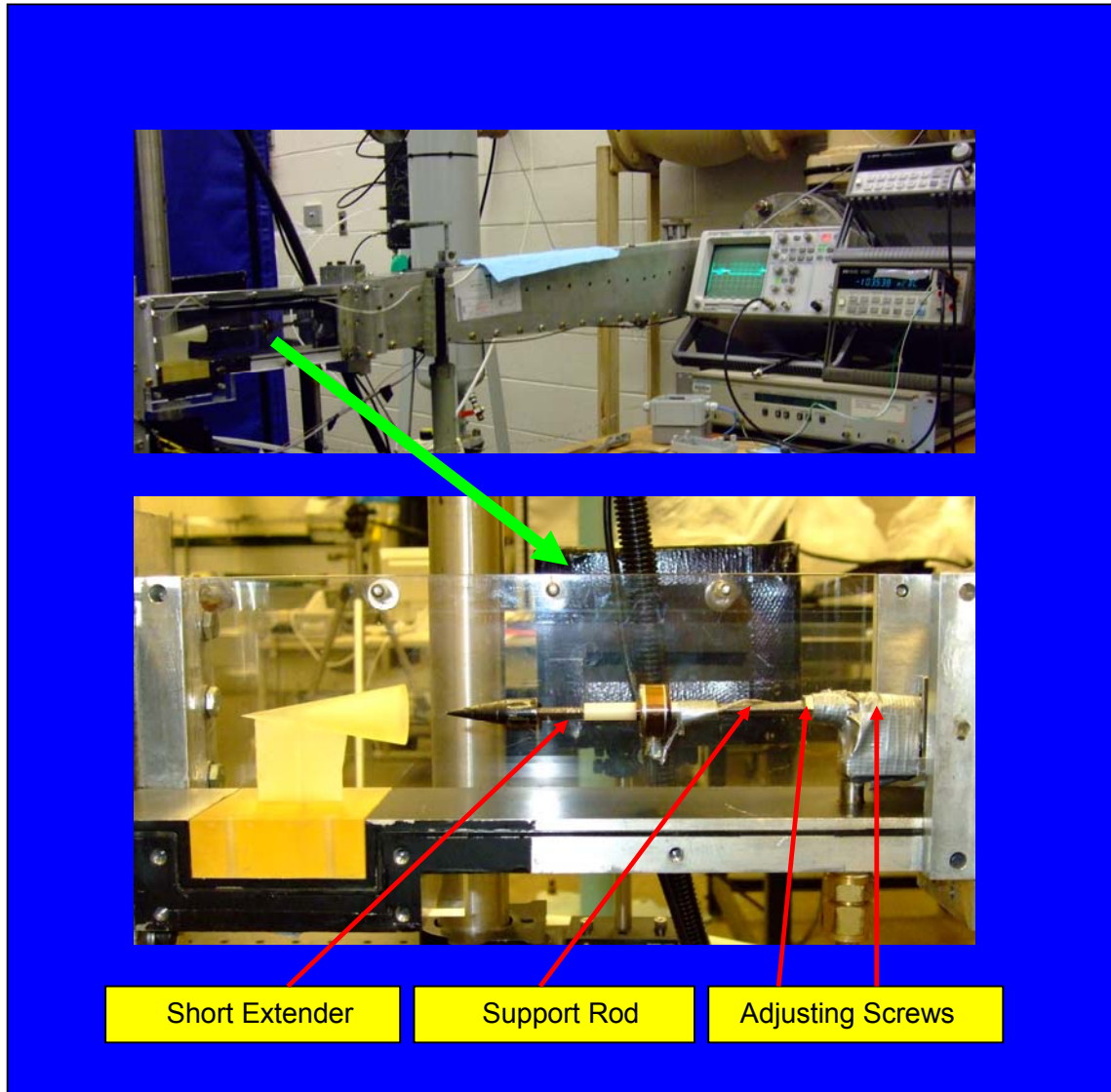


Figure 3.12: Secondary Configuration.

accommodate keeping the wire bundle and circuit-board outside the wind tunnel. The new load cell wires were secured to the test mounts via industry-grade tape shown in Figure 3.12. The addition of the short extender rod connecting the store to the load cell

proved to be a significant change. Lessons learned from the preliminary configuration indicated that either a thicker or shorter extender rod was required to eliminate the large oscillations. Due to the sensitivity of the load cell, a compromise was made. This consisted of adding the heavy support rod used in previous experiments [21] along with the short extender rod. The support rod was secured to the mounting apparatus on one end via the adjusting screws and coupled to the base of the load cell on the other. During all remaining tests conducted, very little – if any vibrations were seen in the support rod. The total length of the shorter extender rod was 37 mm resulting in a distance of 36 mm from the store's base to the face of the load cell. Multiple stages were evaluated by moving the entire mechanism consisting of the store, extender, nylon coupler, load cell, steel coupler and stiff 10-20 support rod. The support rod had nuts on either end which were loosened to facilitate moving the assembly back or forth. This set-up and operation was migrated to the third configuration examined.

Tertiary Configuration

Figure 3.13 shows the third configuration for the experimental portion. In the third configuration a longer extender rod between the load cell and store was used. In this case the longer extender rod had a total length of 52 mm making the distance from the aft of the store to the face of the load cell ~51 mm. Operations were carried out in similar fashion as in the secondary configuration. It was expected that this configuration would provide an optimal condition because it allows more separation between the store and the load cell without extending the store so far that heavy oscillations would prevail as in the preliminary runs. Such heavy oscillations would severely damage the load cell. Since adding the longer extender was expected to

create an optimal condition, the polymer store was also incorporated in addition to the metal store. This configuration proved to be the best for obtaining the axial loads on the store.

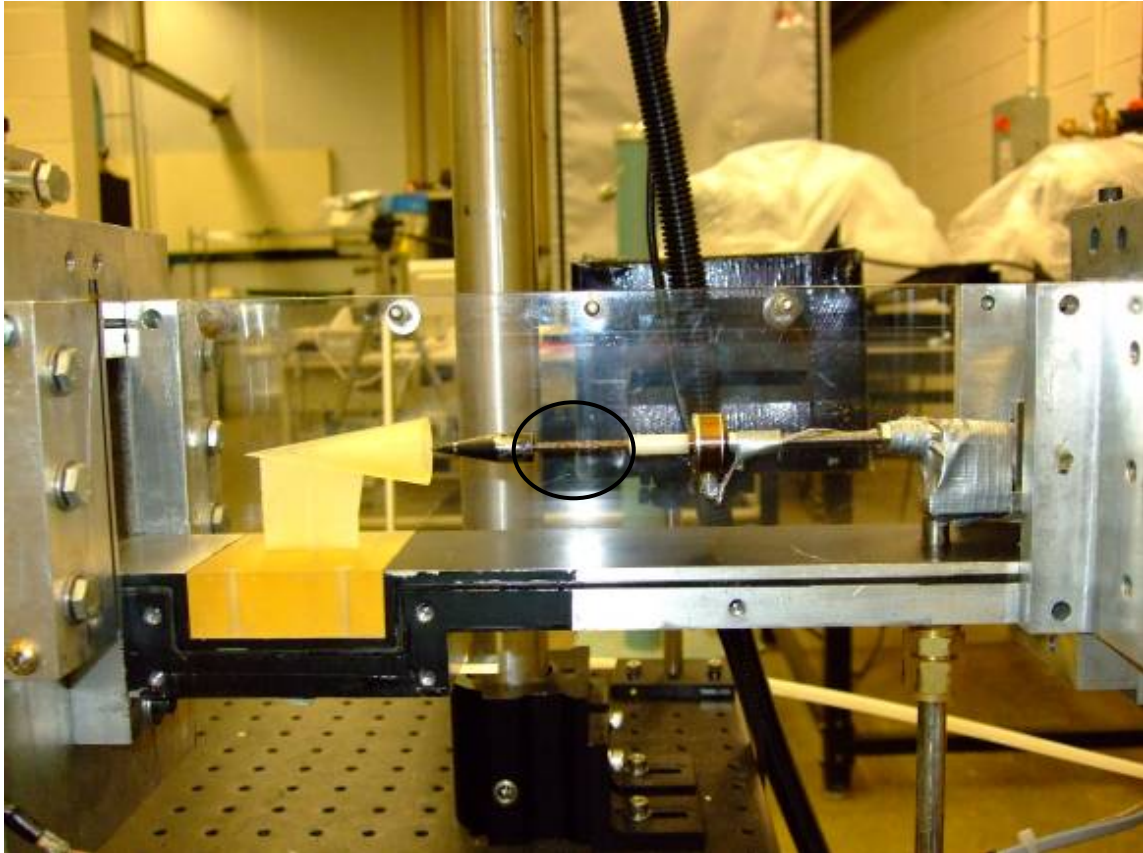


Figure 3.13: Tertiary Configuration.

Experimental Operations A given run was performed by following a standard sequence of events. First, the store/load cell/support position was determined by measuring the distance between the cone base and store tip and fastening the nuts on either side of the large support rod. The measurements were performed by using trimmed markers of a predetermined length and verifying with a small metric ruler. Then the wind tunnel walls were put back in place to complete the set-up for the particular run. This is depicted in Figure 3.14 below. The control pressure was set as desired and a vacuum was

allowed to draw out air from the down-wind side. To initiate a run, the oscilloscope was first triggered for a single sweep and then the tunnel was started via the computer interface. Across the runs performed, the average run time was approximately 6-12

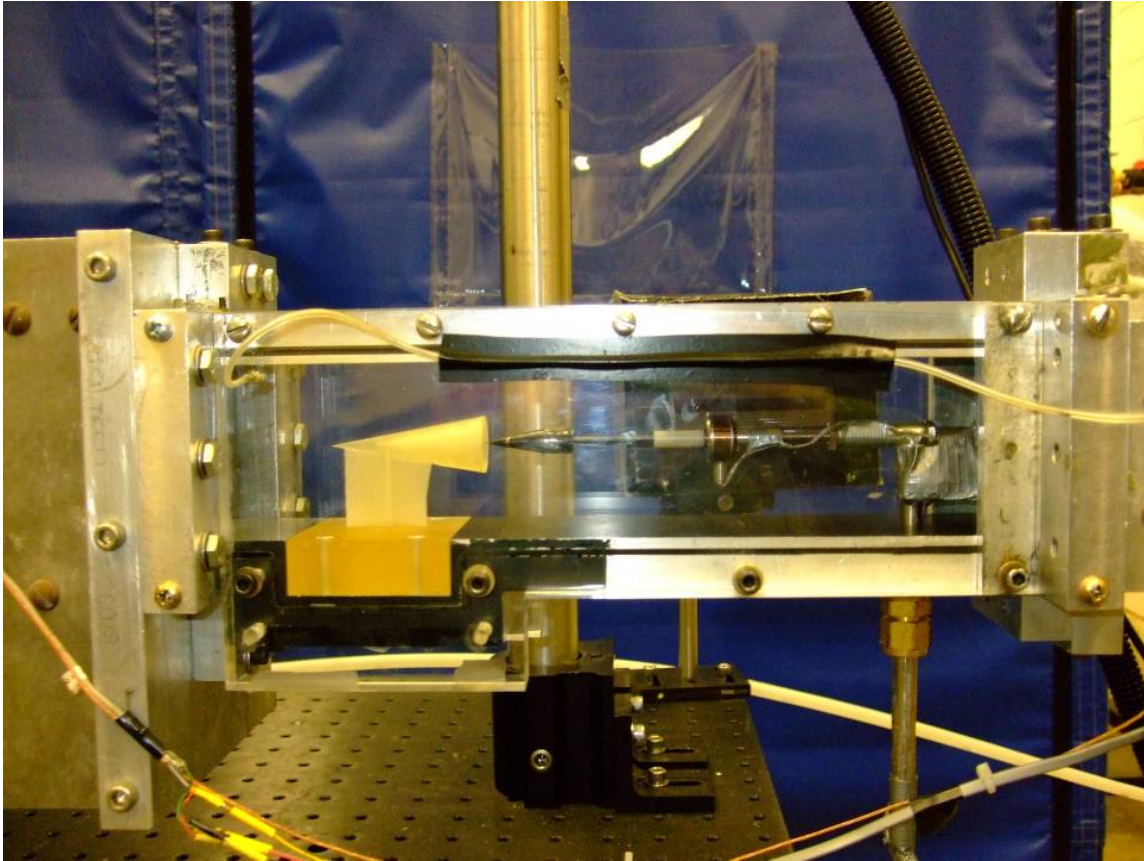


Figure 3.14: Photo of a typical experiment.

seconds. The multimeter recorded instantaneous changes in voltage while the oscilloscope recorded all the voltage across a predetermined time interval or sweep. Sweeps were typically set for 20 seconds which was sufficient time for the wind tunnel to operate and data to be properly recorded for analysis. A typical output plot from the oscilloscope taken from one of the runs can be seen in Figure 3.15. The initial vacuum spike can be seen followed by the control pressure spike. Upon tunnel shut-down, the oscilloscope typically leveled off at or near the value measured before the test. For each

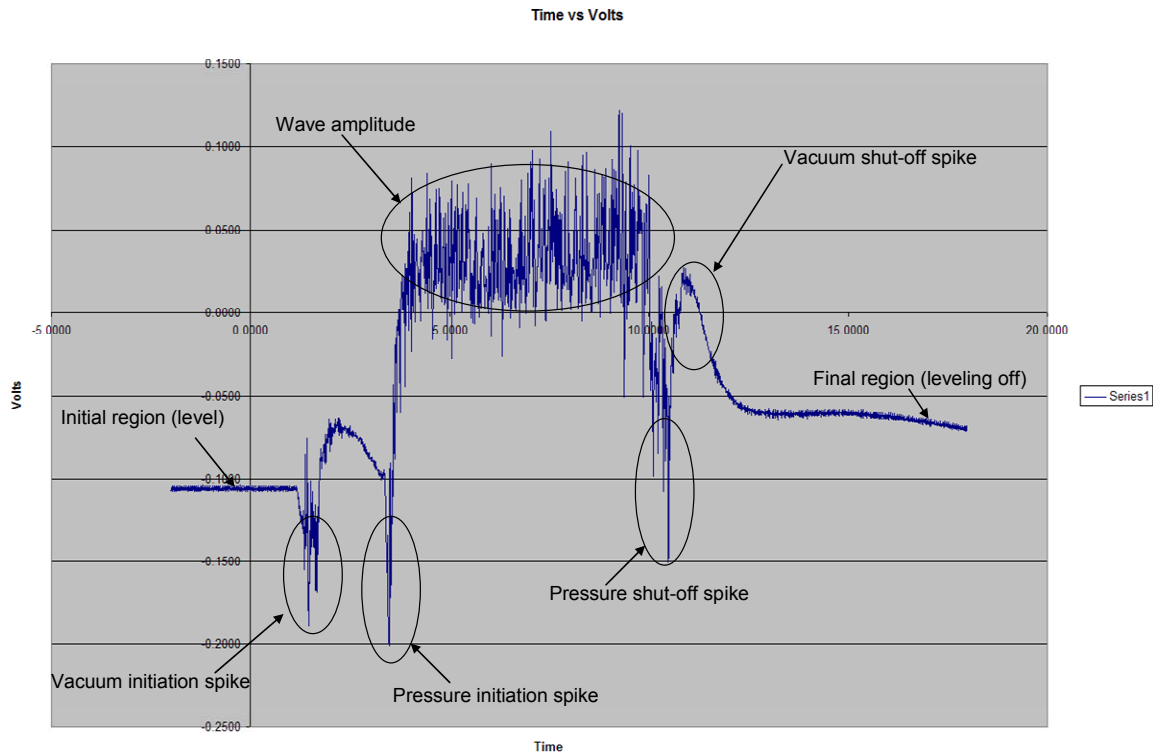


Figure 3.15: Typical data plot recorded by oscilloscope.

of over 160 wind tunnel test runs completed, an associated “Time vs. Voltage” plot was generated.

3.7 Data Acquisition and Processing

The results extracted from the data rely on careful data reduction and processing techniques. Both CFD and experimental data required post-processing. Due to volume, the experimental data required significantly more time, precision and consideration. This was due to the complexity of the testing environment.

CFD Data A completed computation consisted of a three dimensional model of the entire calculated flow field within the confines of the wind tunnel. Figure 3.16a and b depict an early inviscid computation of Mach number. The basic mesh

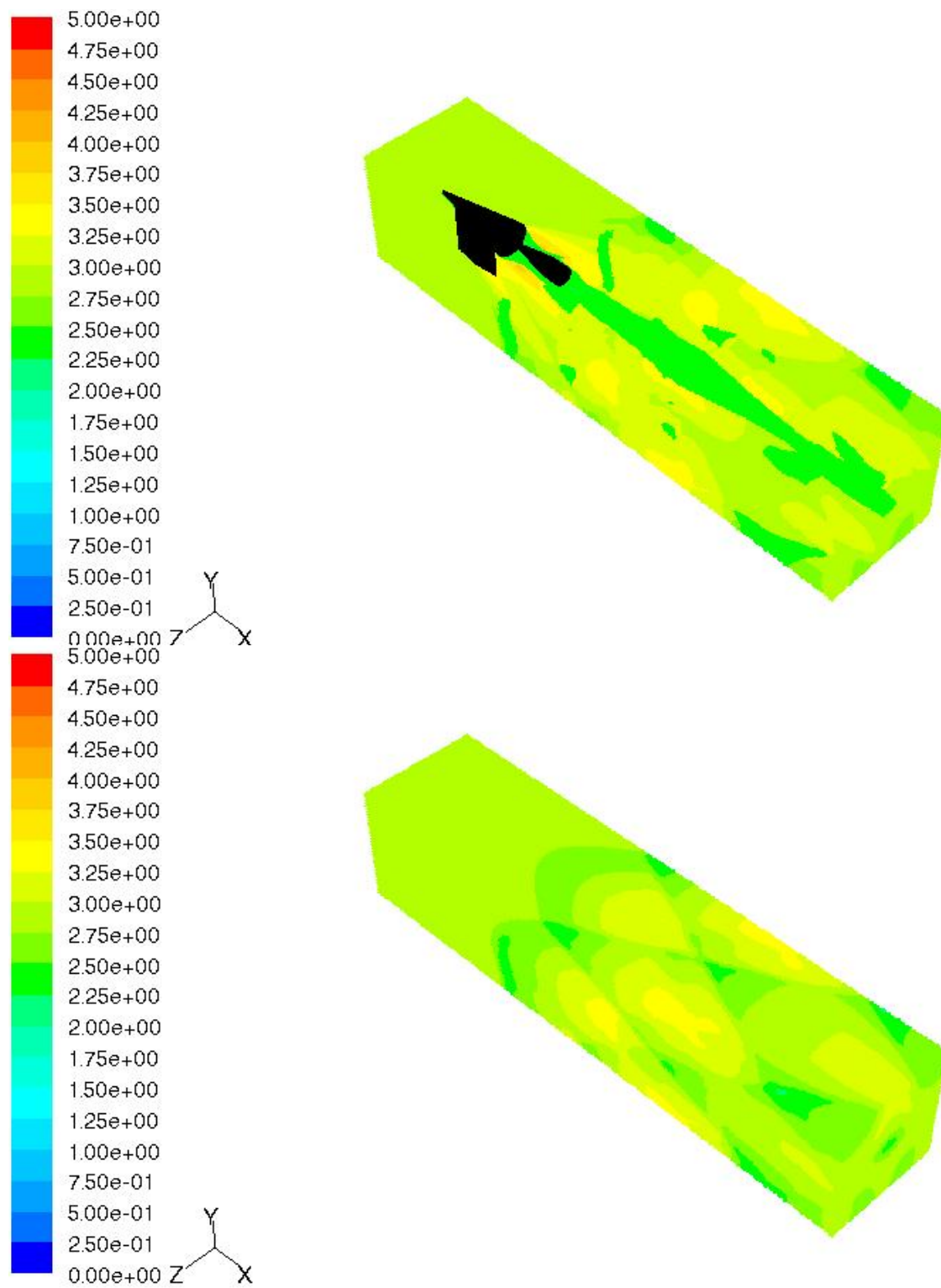


Figure 3.16a: 3-D Isometric view of Mach number.

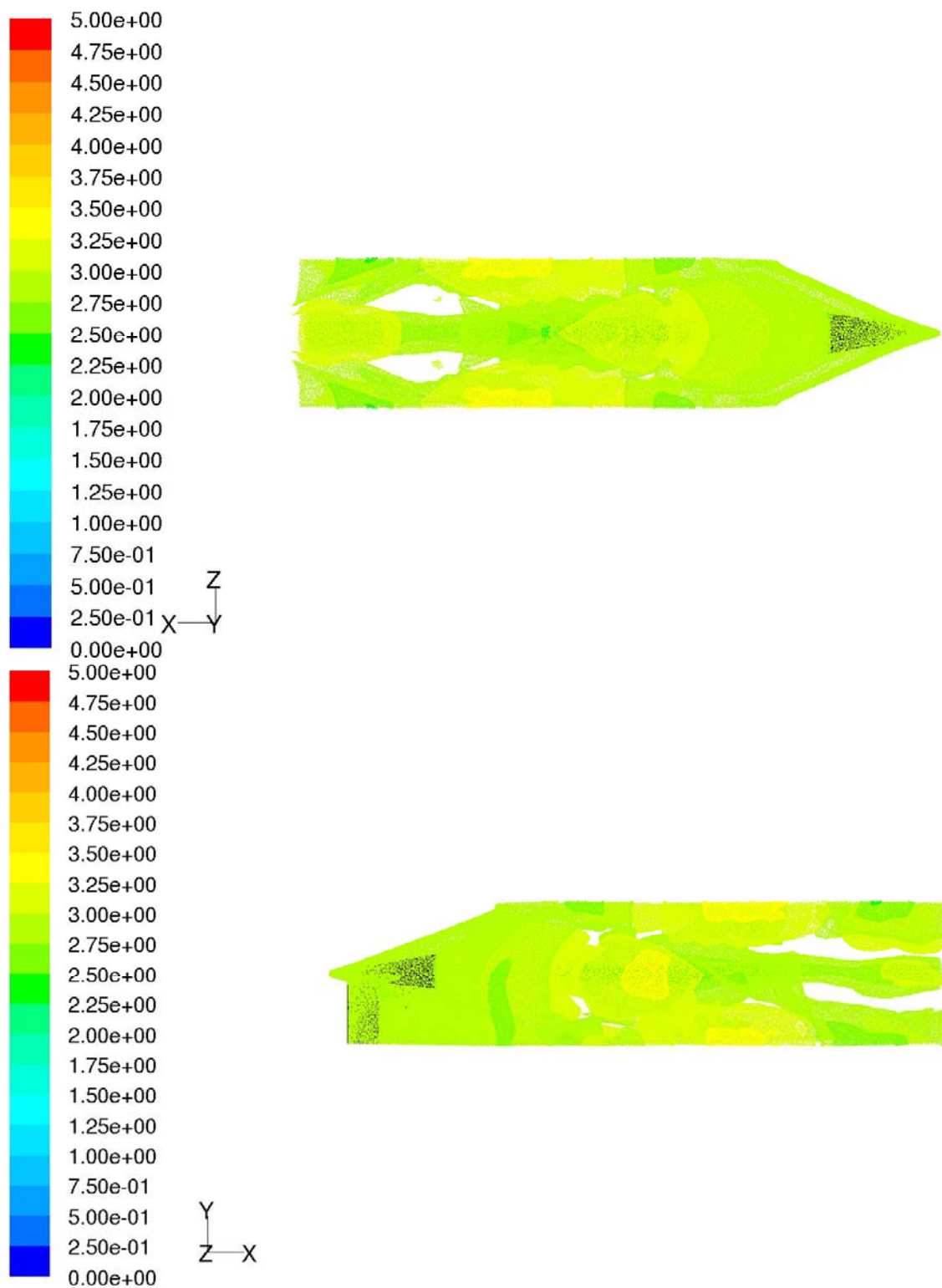


Figure 3.16b: 3-D Wind tunnel interior view of Mach number.

contributed towards development of the mesh that led to the final results. Figure 3.16a is an isometric view including the 3-dimensional flow field and Figure 3.16b include a top and side view respectively of the flow field internal and incident to the surfaces of the wind tunnel. These figures are presented here to demonstrate that 3-dimensional effects can clutter and conceal valuable information. Although some useful observations might be made with respect to wall effects such as the reflected shocks, it would be difficult to deduce information regarding flow symmetry, especially in the base region. For this reason, the 2-D cut planes were used to perform examinations of the flow field in the pertinent dimension or viewing plane. This was done by calculating the exact location of the desired frame in x, y and z coordinates and inputting the values in *Fluent's* drop-down menu. After a few iterations, various cut lines and planes were generated for various contour, vector and pressure plots. This is a great advantage of using a package such as *Fluent* to perform CFD.

Experimental Data As the experiments were conducted it was necessary to monitor the data acquisition system, wind tunnel responses, experimental set-up and laboratory environment to ensure the appropriate data was acquired. Several wind tunnel test runs were omitted due to calibration errors, oscilloscope synchronization errors and the presence of liquid in the wind tunnel test section. Once these problems were resolved, the post-processing of the accumulated data became the challenge. The benchmark of experimental data collection was the time vs. voltage reports generated from the oscilloscope. Initially the expectation was the resulting plots would take on a typical form as shown in Figure 3.17. Although this situation is preferred, many of the

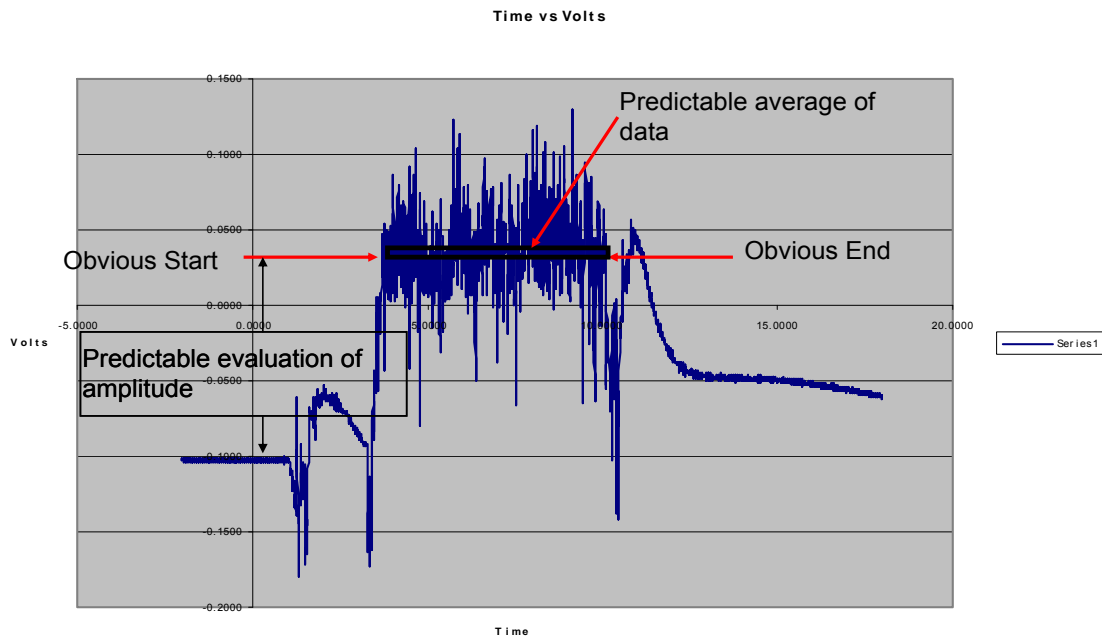


Figure 3.17: Plot depicting ideal amplitude increase.

reports resembled the form seen in Figure 3.18. Figure 3.17 resembles a step input in which a discernable start and finish can be deduced as well as a relatively level or predictable amplitude mean. Such a response is easy to evaluate. Averaging the amplitude peak across the start and end time-interval generates the time-averaged response of the load cell. Subtracting the averaged amplitude peak from the initial region or base provides the change in load received from the load cell. This method holds even if the amplitude peak is below the initial region. In such a case, the sign (+/-) determines the direction of the load based on the load cell orientation. Applying the calibration factor determines the load in grams-force. In cases like Figure 3.18, determining the load value was not as straight-forward due to the amplitude response. As a result, a consistent procedure was implemented and applied to every time vs. voltage report. The criteria consisted of determining the beginning (t_1) and ending (t_2) of the peak based on time.

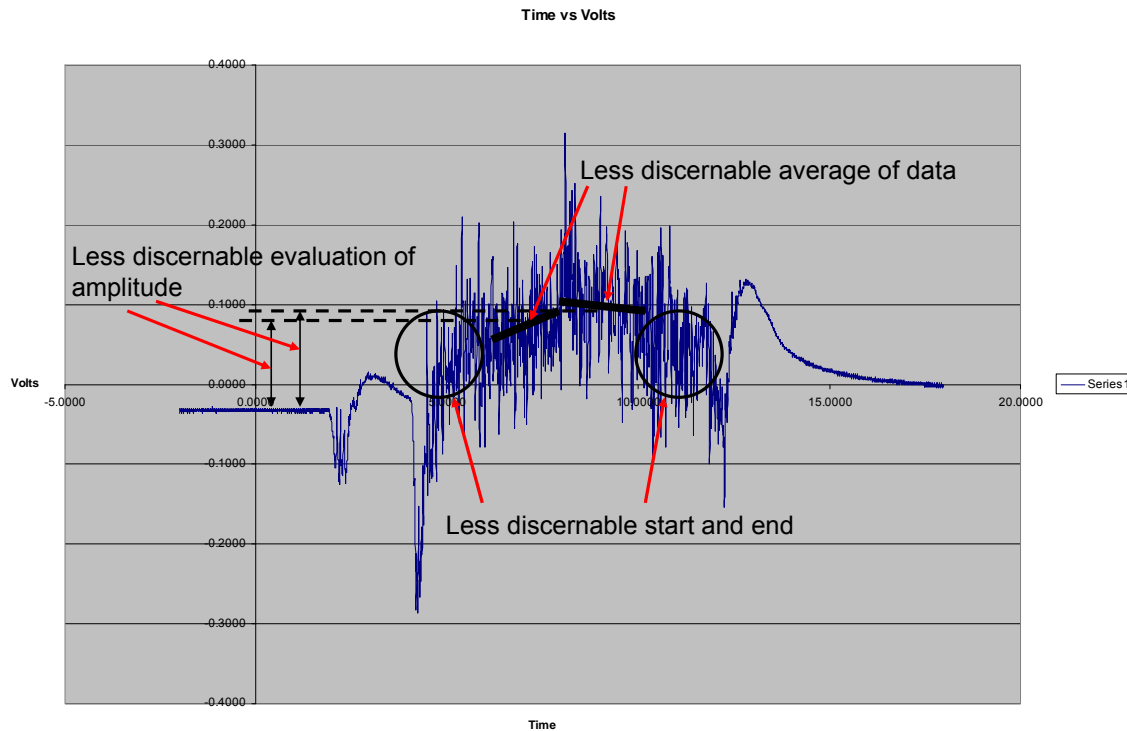


Figure 3.18: Plot depicting less-than-ideal amplitude.

Once t_1 and t_2 were determined, the average of the two values was taken to determine the center of the data range. In more difficult cases multiple selections of t_1 and t_2 were made and compared. To determine the average peak, a “data-frame” was identified by incrementing (+ and -) a deviation factor of a predetermined time interval. Initially several reports were analyzed using a time factor of 0.5 second resulting in a total frame of 1.0 second. Later, a 1.0 second factor was implemented which resulted in better alignment of the data with the previous method without expanding beyond the total time frame of the amplitude peak. This analysis method is depicted in Figure 3.19. Obviously there is some room for error when determining t_1 and t_2 however the adverse impact on the data is greatly mitigated by implementing the deviation factor. Averaging over a more specific range will incorporate data points that fall within the center of the

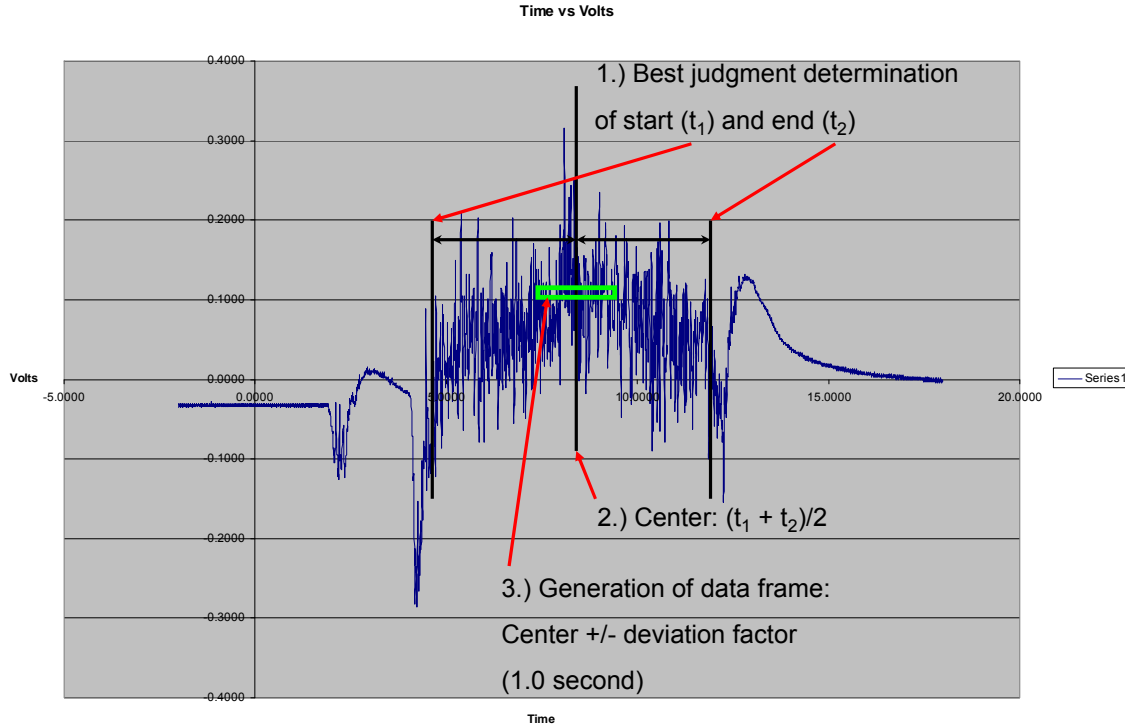


Figure 3.19: Experimental Data Post-processing procedure.

amplitude range. Although some data points on the edge are then omitted, it is data that may be questionable and is only useful for determining the desired range.

Three approaches were tried after all the experimental plots had been generated. The final approach was implemented over the others for three reasons:

1. When slightly adjusting the selection for t_1 and t_2 for a given plot, the 2-second time averaging frame produced the most repeatable data in terms of metric load values.
2. When accounting for the values generated in subsequent test runs at varying x/D locations, the 2-second time averaging frame generated values that better matched the expected overall trend.

3. Approach 3, the 2-second time averaging frame, provided better data confidence by omitting the questionable start and end selections while maintaining the broadest interval for time averaging without reaching or exceeding the endpoints (t_1 and t_2).

Of the challenges encountered in the experimental portion, the data analysis and reduction proved to be the most time-consuming. Accurately processing the data aided in identifying the need for additional tests and the configuration changes.

Once the metric load measurement was calculated from the data plot, it was non-dimensionalized into a coefficient of drag force using Equation (3.9).

$$C_{F_i} = \frac{F_i}{\frac{1}{2} \rho V^2 A_{ref}} \quad (3.9)$$

The load (F) is the metric load value obtained from the load cell via the oscilloscope plot and converted to Newtons. The calculated A_{ref} was 66.3 mm^2 and represents the maximum cross-sectional area of the store. Given the temperature and Mach number, the wind tunnel free stream velocity was calculated as 614 m/s via equation (3.6) which holds for ideal gas approximations. This calculated value falls within 4% of the velocity obtained via CO_2 seeding in the AFIT wind tunnel with the redesigned strut and cone [34]. During the experimental runs the wind tunnel computer recorded the stagnation and free stream pressure measurements in pounds per square inch and tabulated them in an Excel spreadsheet. The test section density was computed by rearranging equation (2.1) into equation (3.10):

$$\rho = \frac{P}{RT} \quad (3.10)$$

Here the pressure must be in Pascals, while $R=287.05 \text{ J/kg}\cdot\text{K}$ and T is the test section temperature in Kelvin. The temperature was deduced via Perfect Gas relations and compared with the CFD calculated temperature as well as previous experimental data in the AFIT wind tunnel [21]. The experimental value for T is 110.0K. The resulting density is given in kg/m^3 . The calculation spreadsheets can be seen in Appendix D.

Error Quantification While both the CFD and experimental data may have error, the error discussed here is specifically assigned to the experimental data. Error in the CFD data is evident in truncation error in the solutions, divergence of the residuals and grid inconsistencies and is difficult to quantify. Therefore particular attention was given to these methods to generate CFD data that is refined and trustworthy. Error in the experimental data can be allocated to two inclusive sources: error induced by the devices carrying and measuring the signal and error in the signal itself. Error in the signal is assigned solely to the load cell. The load cell receives input and converts it into the signal. The amplifier, multimeter and oscilloscope carry and measure the signal.

Amplifier Error Error in the amplifier is identified as changes to the signal as a result of poor or incorrect amplification. The most likely error in the amplifier would be the presence of a non-linearity in the amplification of the signal. This could be caused by exposure to a magnetic field, power surge or competing signal within the radio frequency range. It is expected that performing the calibration in accordance with the equipment manufacturer's guidelines should mitigate any biases introduced into the

device. When the calibration was performed, the multimeter was used to monitor the output signal. Successful calibration with a 100 gram load concluded when the multimeter reflected the correct voltage measurement for the load. Applying the conversion factor of 0.005 mV/gram to the 100-gram load predicts a voltage measurement of 0.500 Volts. For the full scale range of 100 grams the observed error was less than 2.0%. Although several additional masses were examined, they were not recorded because in all measurements the same error margins were maintained.

Multimeter Error Error in the multimeter is identified as the tendency of the multimeter display to wander when presenting a value. The difficulty of this error is that variations or errors in the signal are also capable of causing the multimeter to wander. In all cases where the load cell had no object attached to it, the observed error in the multimeter was equivalently 0.0% since no observable wander occurred. Given this, the only other potential for error is a bias within the multimeter causing the readout to consistently display a higher or lower than true value. Given the current calibration sticker attached to the multimeter, it is assumed that any bias is insignificant. Additionally, any bias that causes a shift in the display will be eliminated when calculating the change in signal for a data set.

Oscilloscope Error Error in the oscilloscope is identified as oscillations or alterations to the signal that are not already introduced by the signal, the amplifier, multimeter or load cell. This implies that oscilloscope error is similar in nature to multimeter error. When the oscilloscope initiated a sweep, miniscule wander in the signal could be observed. Figure 3.20 depicts a zoom-in of the initial readout of the

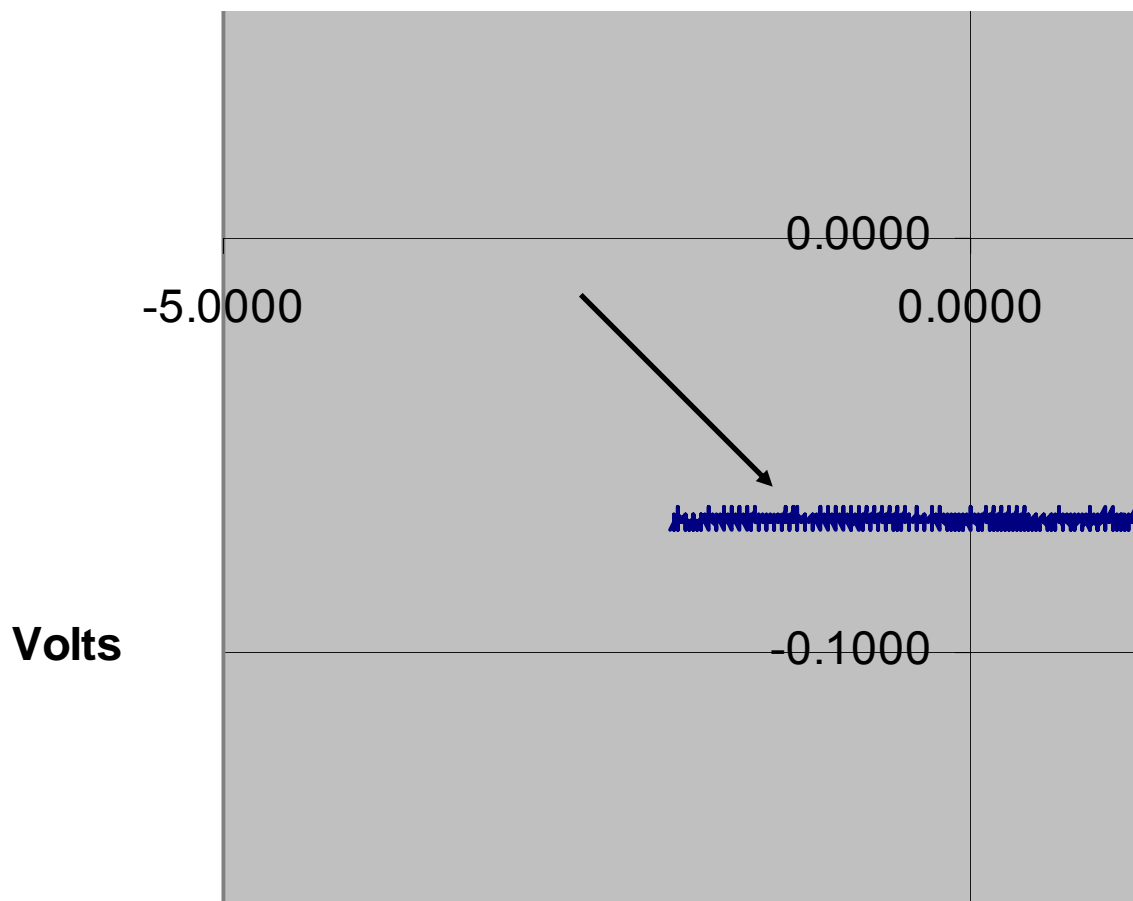


Figure 3.20: Zoom-in of data plot generated by oscilloscope.

oscilloscope in a typical data run. The presence of low frequency oscillations could be introduced by any number of sources, including the oscilloscope itself. Digitized error is considered a factor since it would be on the order of the oscillations seen in Figure 3.20. However, such error is negligible when compared to the oscillations seen in the amplitude of the signal. Therefore, similar to the multimeter, it is difficult to assign a quantitative value of error. Current calibration stickers indicate that any bias within the oscilloscope should be negligible. Therefore, it is assumed that similar to the multimeter, any error introduced by the oscilloscope should be accounted for and eliminated when evaluating the change in the signal. Wander in the multimeter is largely associated with

the transverse load or bending moment experienced by the load cell from the store and extender. It was observed in many cases that when the multimeter display was examined prior to initiating an experimental run, some wander was apparent as a result of the load cell.

Load Cell Error The error present in the load cell signal is best seen via the data plots in Figures 3.17, 3.18 and 3.19. It can be clearly seen that in the initial region (Fig. 3.20) there are some small-scale oscillations present. In the wave peak region heavy oscillations in the signal can be seen. The wave peak region corresponds to the area where the store is undergoing the greatest dynamics. Therefore it is assumed that these oscillations are a direct result of excessive transverse and axial buffeting of the store. This assumption is strengthened by the fact there are only miniscule oscillations present during the initiation cycle of the wind tunnel. Furthermore, as discussed previously, sharp changes in the test section flow field caused by the pressure and vacuum spikes generate severe spikes in the load cell signal (ref. Fig 3.15).

In order to quantify the load cell repeatability and error, multiple runs were performed for the data sets. The statistical error introduced by successive runs at the same x/D location is quantified by equation (3.11):

$$\sigma = \sqrt{\frac{\sum (\bar{X} - \bar{\bar{X}})^2}{N - 1}} \quad (3.11)$$

where \bar{X} is the average force coefficient value determined from the samples of a single run in grams-force, $\bar{\bar{X}}$ is the average force coefficient value of multiple runs performed at

a given x/D , and N is the total number of runs performed at the particular x/D . The resulting value, σ is the standard error from the mean [46].

Figure 3.21 shows the error trends calculated using Equation (3.11) for the optimal configuration set-up which includes the longer extender rod. Equation (3.11)

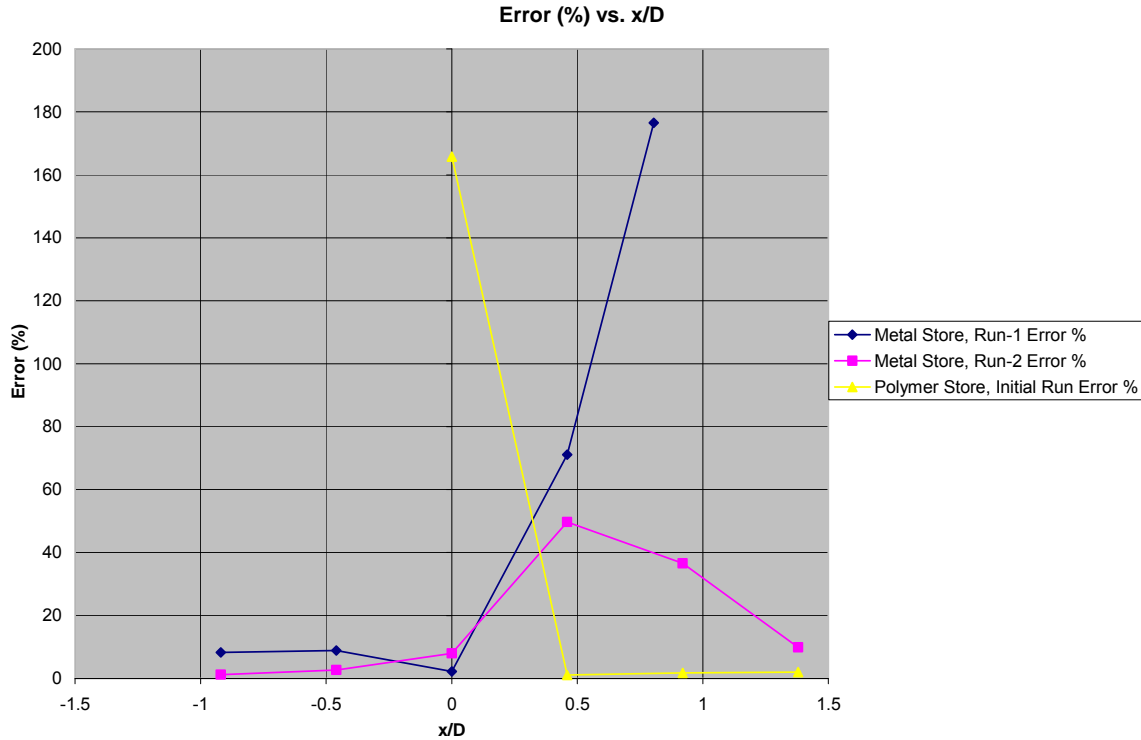


Figure 3.21: Average Statistical Error (successive runs), long extender.

applies only to the two data sets with the metal store and the initial run with the polymer store. In these cases the force coefficients were determined by averaging multiple runs at a given x/D

There are two possible sources for the error plotted in Figure 3.21. One is error introduced by changes or alterations to the test set-up itself between runs. Errors introduced by alterations to the tests are assumed to be unquantifiable since no intentional modifications were made to the test set-up between successive runs at the same x/D

location. The second is error within the operation of a test, such as deviating pressures or temperatures within the wind tunnel. Typically the wind tunnel walls were left on while the vacuum was being drawn for the next run. It is assumed the wind tunnel maintained relatively equivalent pressures, temperatures, and no anomalous effects during successive operations. At $x/D = 0$, the polymer store trend contains a significantly high percentage of error. At this point the determined values of axial load were near zero, contributing to some inflation of the error. The error introduced into the load cell measurement is most likely due to the transient nature of the flow transitioning the cavity opening and around the store tip [21, 38]. Presence of this error was evident in the vibrations and oscillations of the store tip as a result of axial buffeting and transverse loading. This conclusion is reasonable since the base flow in the immediate vicinity of a cavity will be separated, turbulent and unsteady with reversed flow entering the cavity resulting in possible resonance at the base opening of the cavity. The resonance was evident in significant transverse loading imparted to the tip of the store. The presence of the strut will also contribute to asymmetry near the cavity [21, 38]. In a majority of the wind tunnel tests, transverse vibrations were observed in the vicinity of $x/D = 0$ indicating the adverse effects of the cavity and turbulent transition of flow into the cavity.

The general trends show considerable variation in the error. In addition to the high error in the polymer store at $x/D = 0$ is the high error seen in the last x/D location for the metal store, run 1. The anomalous peaks and variation in error is partially addressed in the Honeywell specification sheets in Appendix C. Paragraph 5 of the Sensotec Installation Instructions indicates the fixture weight (store, extender and nylon coupler)

will introduce some unbalance in the strain gauge as a result of the applied bending moment. The effect of the unbalanced strain gauge on load values across successive runs and successive x/D locations can be quantified in terms of repeatability. The published non-repeatability of the load cell is specified by Honeywell as $\pm 0.1\%$ of the full scale range (1000-grams). This equates to a maximum non-repeatability of 1 gram.

Referencing Appendix D, the actual metric loads for successive runs at a particular x/D for the metal store run-1, metal store run-2 and polymer store initial run, can be compared. With the exception of x/D = 0, the Polymer store run falls within the 1-gram repeatability limit specified by Honeywell and maintains the flattest trend. The metal store sees an increase in deviation between successive runs and subsequently falls out of the repeatability limits. Therefore it is concluded that the polymer store introduces less error in the load cell signal by reason of its considerably lower mass. The higher mass of the metal store introduces a significant change in the natural frequency of the vibrations transmitted through the longer extender rod and into the load cell. As a result, the metal store contributes to non-repeatability.

Aside from the error quantified from performing multiple runs, the oscillations within the signal recorded by the oscilloscope can be used to determine the standard error of the mean for a particular load measurement. For a single run performed at a given x/D, the standard error of the mean is calculated using equation (3.12):

$$\sigma(\bar{X}) = \frac{\sigma}{\sqrt{n}} \quad (3.12)$$

where σ is the standard deviation of the samples from the mean and n is the number of samples across which the mean is computed [46].

Figure 3.22 shows the standard sample error calculated using Equation (3.12).

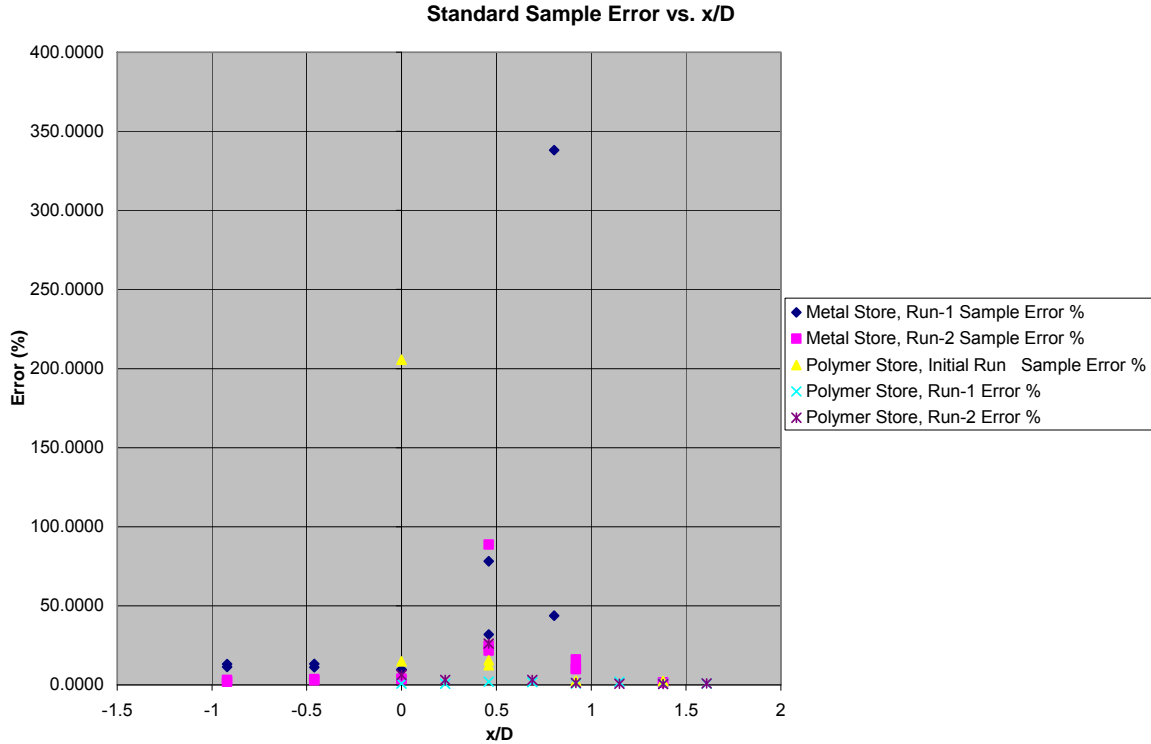


Figure 3.22: Standard Error of the Mean (single run), long extender.

Equation (3.12) was applied to each individual wind tunnel run completed with the longer extender rod. For the purpose of examining data set repeatability, two data sets with the polymer store (Run-1 and Run-2) were performed by completing a single run at each x/D . With the exception of one run at $x/D = 0$, all the sample errors for the two polymer store runs are less than 6%. Two anomalous data points are seen for the polymer store, initial run and the metal store, run 1 at $x/D = 0$ and 0.80. A logical conclusion is that these two anomalous data points contributed to the high average statistical error at the same x/D location as displayed in Figure 3.21. At these particular locations the store is

experiencing the effects of reattachment shocks interacting with the tip and possibly a normal shock forming on the tip as the store enters supersonic flow in the reattached far wake of the cone [15, 19, 21, 38, 41]. Although less anomalous, notable error can be seen in the vicinity of $x/D = 0.5$. While a congregation of data points is seen in the vicinity of 25% error, a few are scattered as high as 80% demonstrating that experiments conducted with the metal store tend to have higher error.

The data plots introduced in chapter 4 include average statistical errors as calculated by Equation (3.12). For the single run cases, error magnitudes from the initial run, polymer store are applied. Based on the lower mass and demonstrated repeatability, it is assumed that the average statistical error from the polymer store (initial run) will provide an accurate estimate for the first and second comparative polymer runs.

3.8 Summary

Research procedures and methods were initially guided by documented cases of successful research. Although the CFD portion was started first, difficulties with convergence caused the CFD portion to be ongoing. Multiple first and second order runs were performed along with laminar and turbulent flows. This was done to gain familiarity with the software and to update load predictions as efforts transitioned into the wind tunnel. Parallel computing was used to reduce time and increase efficiency. The CFD runs eventually met convergence criterion based on declining residuals and level-off of calculated drag values on the store.

The experimental portion encountered issues when excessive oscillations of the store were observed during the preliminary tests. Two valid configurations were

subsequently examined to determine the effects of sting length on the experimentally derived axial loads. To better accommodate the experimental tests, a complete data acquisition system was developed in order to properly generate discernable data and plots of the axial loading phenomenon occurring in the wind tunnel. Due to the difficulties associated with the experimental tests, careful data processing and analysis had to be performed, including implementation of a data reduction criterion. Using the cavity analogy, it was determined that the configuration with the long extender provided the best conformity to the physics of base flow. The load data obtained from the long extender configuration is expected to provide the most accurate data.

Statistical error was calculated and analyzed for all the data sets with the long extender. In the three cases where multiple runs were performed, the average statistical error indicated the polymer store introduced less error than the metal store. Subsequently, two data sets were conducted with single runs for the purpose of examining data set repeatability. The trends tend to match each other to within a few percent. The trends identify increased error in measurements taken in locations where complex phenomena take place such as transient cavity flow and reattachment shocks. Since the two polymer store runs can not account for statistical error introduced by multiple runs, the magnitude of the error from the initial polymer run is applied to both of the polymer store runs to accommodate accurate assignment of statistical error to the final comparative data plots in chapter 4.

IV. Results and Analysis Pertaining to the Strut

4.1 Chapter Overview

This chapter includes the CFD and experimental results as they pertain to the strut. Various sections highlight a particular method in which the strut is analyzed. The second section includes various computationally generated flow visualizations. These will be used to demonstrate the differences in the flow field as a direct result of the struts. The third section analyzes of the transverse force coefficients acting on the store. The fourth section looks at of the pressure distribution charts for the strut and cone and the fifth section introduces the base pressure plots for comparison and discussion.

4.2 CFD Visualizations

Several configurations were examined with CFD. However, only six pertinent configurations are presented here. Flow visualizations are presented to demonstrate the effects of the struts on the flow aft of the cone, including the store. The k- ϵ turbulence model was applied to the three stages of analysis with the original and new strut. In all cases presented here the 1st order flow solver and 1st order turbulence model was implemented for the first 5000 iterations, in which solution convergence took place. This was done due to divergence issues when directly initiating solutions with 2nd order options. For all cases the wall y^+ values were $\ll 1.0$ indicating an adequately fine viscous boundary layer was implemented on the model without the use of wall functions. second order options included at a minimum the 2nd order flow solver and 1st order turbulence model. In a few cases turning on the 2nd order turbulence model was delayed

to treat divergence issues. For each stage a global presentation of the flow solutions is presented first followed by a detailed drill-down for comparison and analysis.

Original Strut, Stage 1: The first case completed was the first stage of store release ($x/D = 0.14$) with the original strut. It reached convergence at 27,290 total iterations. Figures 4.1a and b display the side view and top view contour plots of Mach number for the strut, cone and store respectively. The pale orange region before the cone and strut indicates the Mach 2.92 flow. The conical shock wave can be discerned as well as its reflection off the top wall. The base regions of the cone and store can also be identified by the blue regions. The top view demonstrates that the diamond cross-section of the strut is adequate in retaining z-x plane symmetry in stage 1. The two results show the reflected shock wave does not interfere with the cone's base region in stage 1.

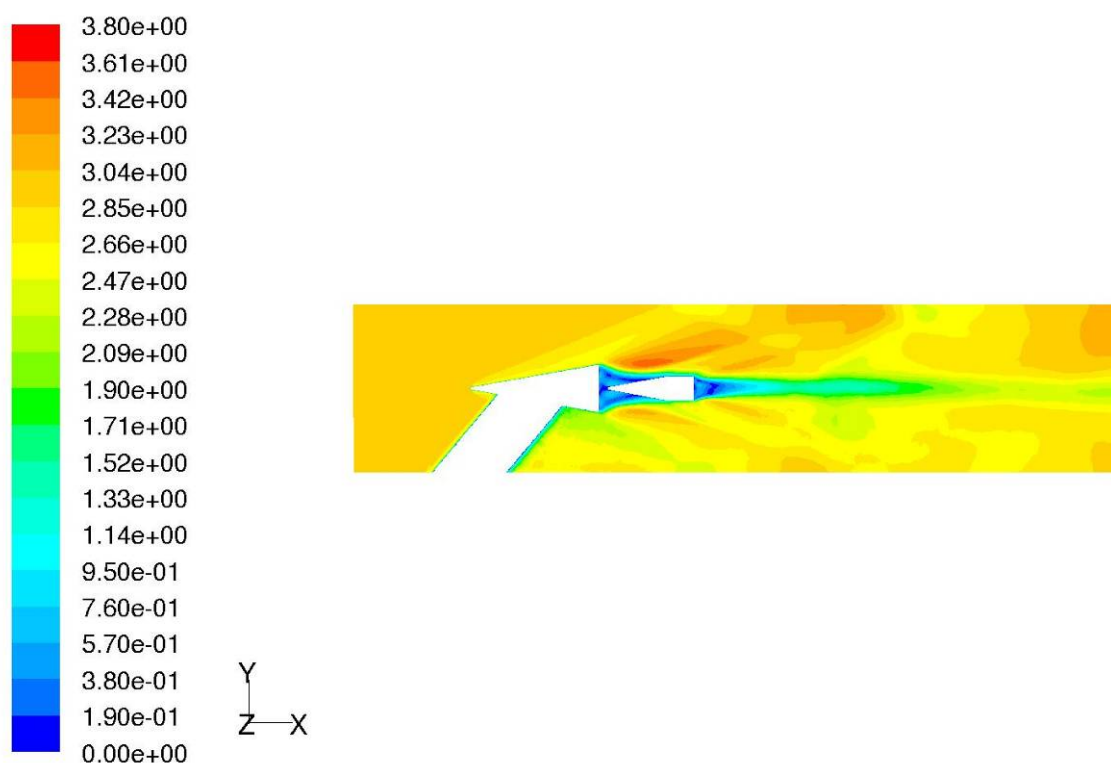


Figure 4.1a: Original strut, stage 1, 2-D Side Contours of Mach number.

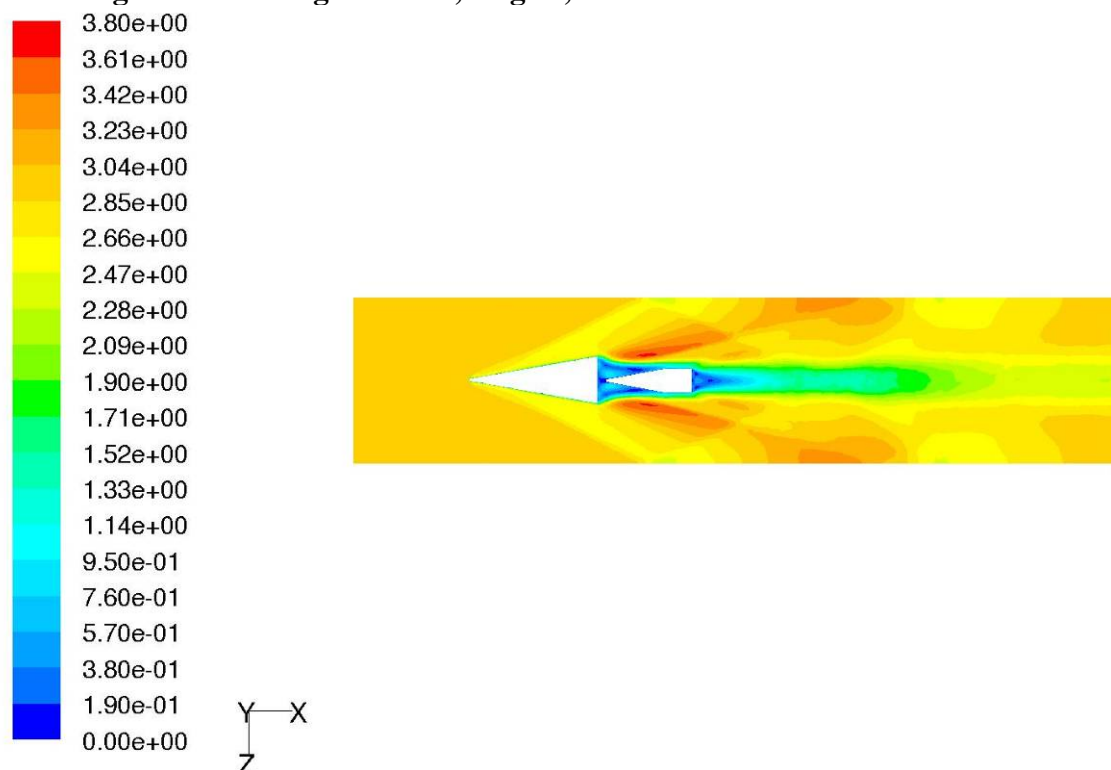


Figure 4.1b: Original strut, stage 1, 2-D Top Contours of Mach number.

Original Strut, Stage 2: The second case completed was the second stage of store release ($x/D = 0.80$) with the original strut. It reached convergence at 5,500 total iterations. This stage 2 run had significant difficulties with convergence most likely due to the unsteady nature of the base region coupled with the store's location. Figures 4.2a and b display the side view and top view contour plots of Mach number for the strut, cone and store respectively. Similar to stage 1, the stage 2 contour plot displays the shock wave propagating from the cone and reflecting off the top wall of the tunnel, as well as the base regions of the cone and store. Different from stage 1 however, is the apparent lengthening or developing of the store's base region. At this location the store is transitioning out of the cone's base region and is beginning to take on its own flow profile. From the two views it can be seen that the reflected shock wave still does not interfere with the cone's base region. At this location however, it is likely that the store's base region will be influenced by the reflected shock wave. The collision point of the reflected shock waves appears to take place behind the store at a distance of approximately half of the store's length. From the top-down view, some level of symmetry is still maintained which strengthens the argument for the symmetrical diamond shape cross-section of the strut.

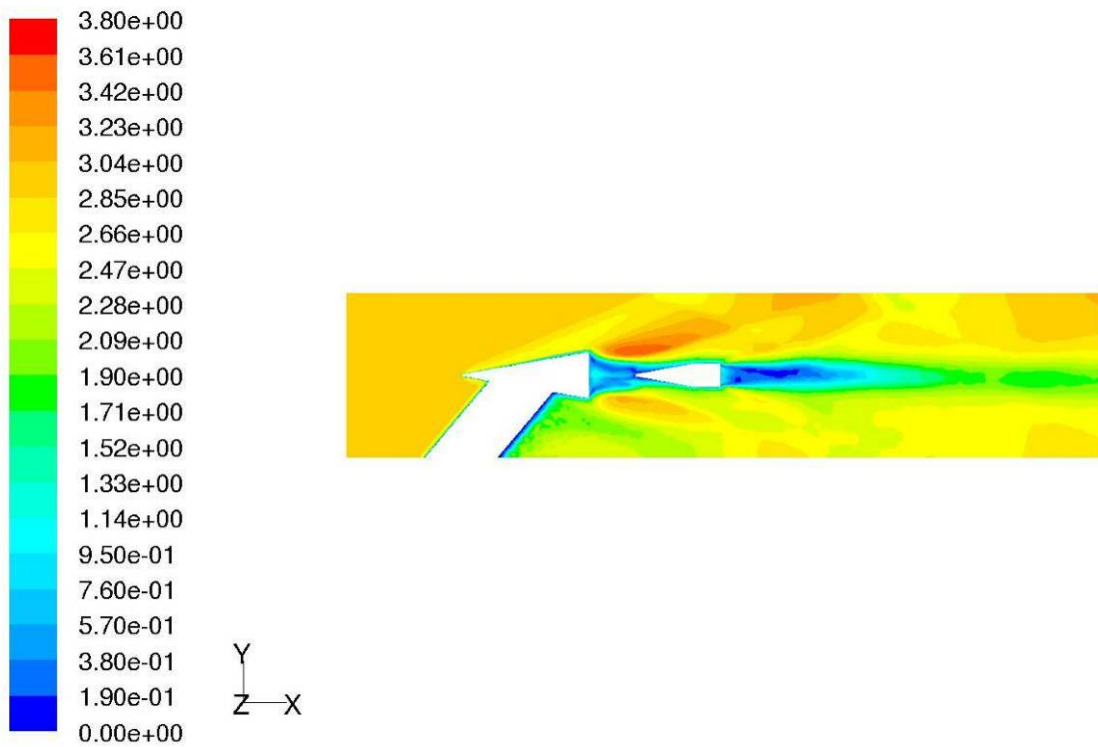


Figure 4.2a: Original strut, stage 2, 2-D Side Contours of Mach number.

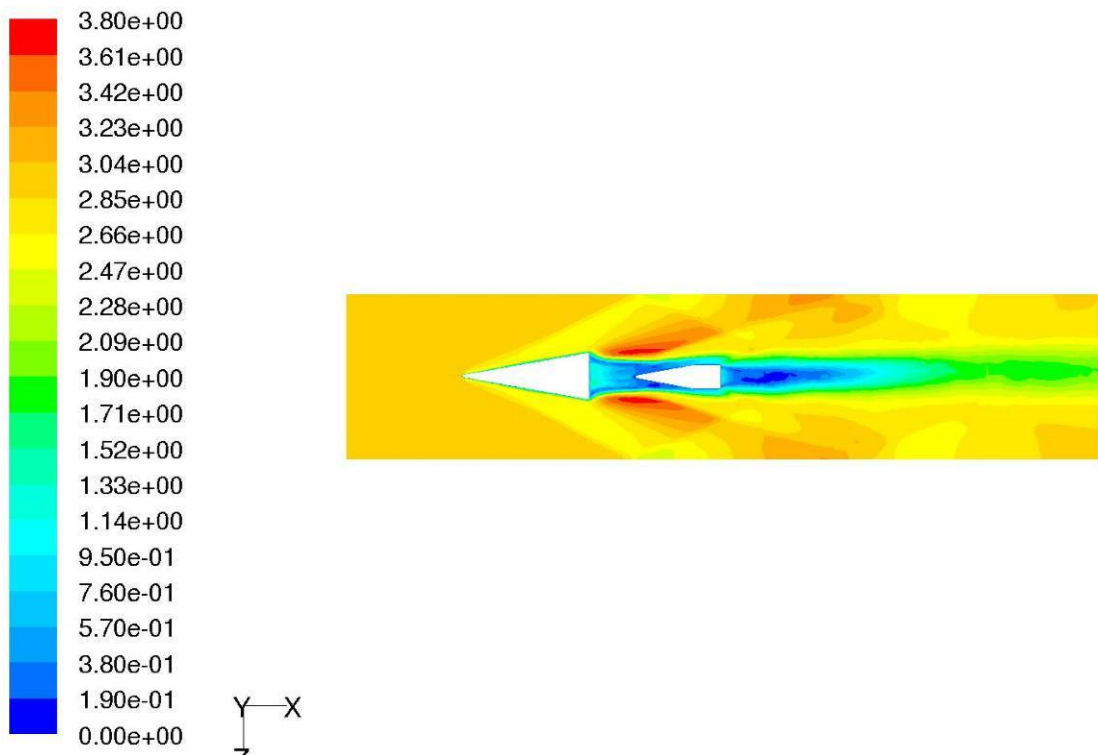


Figure 4.2b: Original strut, stage 2, 2-D Top Contours of Mach number.

Original Strut, Stage 3: The third case completed was the third stage of store release ($x/D = 1.61$) with the original strut. It reached convergence at 15,020 total iterations. The first 5,000 iterations were performed with the 1st order solver and 1st order turbulence model. The latter 10,020 iterations were performed with 2nd order flow solver and 2nd order turbulence model. Figures 4.3a and b display the side view and top view contour plots of Mach number for the strut, cone and store respectively. Here it can be seen that the store has exited the cone's base region. This is evident when comparing to stage 2 and seeing that the tip of the store is no longer interfering with the reattachment point of the cone's base region. The formation of the reattachment shock can be seen in the vicinity of the store's tip. Between the side and top view plots certain defining factors can be seen. The cone and store base regions both display relatively triangular structure as predicted in chapter 2. The recompression waves from the cone and their reflections off the tunnel walls are clearly seen and the reflected shock waves from the cone now impinge upon the store. The faint beginning of recompression waves coming from the store can also be seen. Careful comparisons of the original and new strut flow fields show the expected aerodynamic responses. Therefore it is assumed that they generate visualizations that can be trusted.

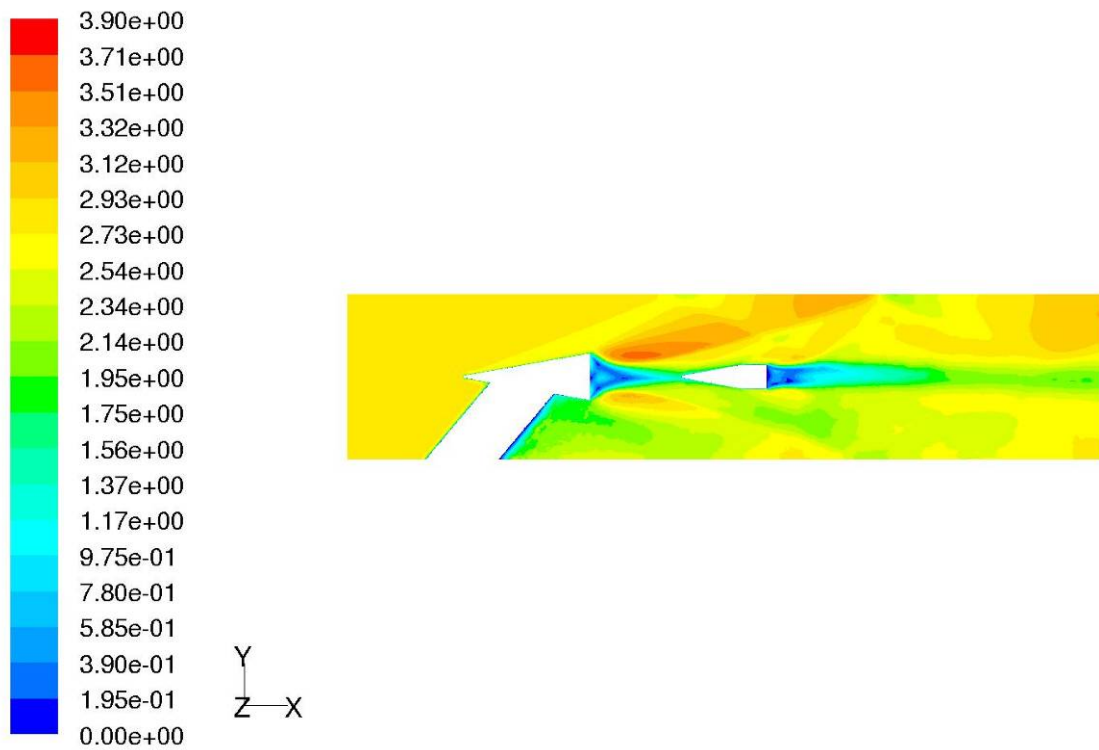


Figure 4.3a: Original strut, stage 3, 2-D Side Contours of Mach Number.

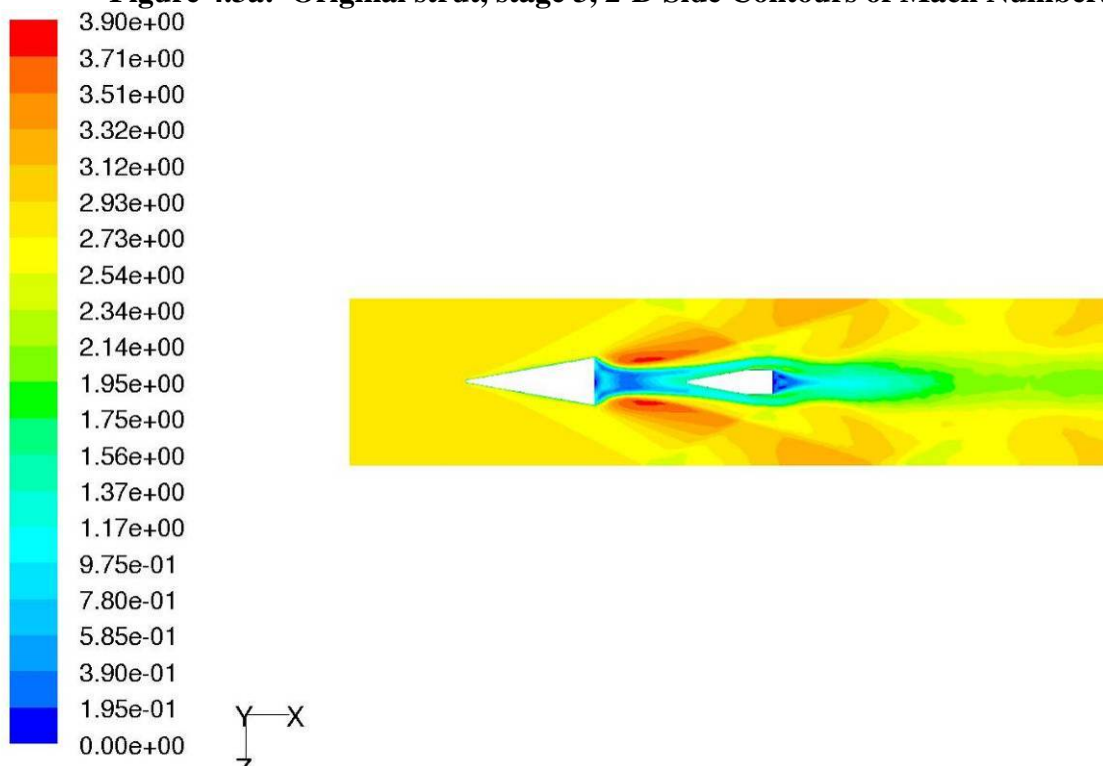


Figure 4.3b: Original strut, stage 3, 2-D Top Contours of Mach Number.

New Strut, Stage 1: The fourth case was complete when it reached convergence at 22,295 total iterations. Figures 4.4a and b display the side view and top view contour plots of Mach number for the strut, cone and store respectively. Similar to the original strut model of corresponding stage, the cone shock wave and trace of its reflection on the top wall can be seen. The cone and store base regions appear to have the expected general structure similar to the original strut stage 1 model indicating that the two models are comparable. The pale orange region before the cone and strut indicates the Mach 2.92 flow. A notable difference from the original strut in these global views is reduction of the high Mach region immediately adjacent to, and surrounding the cone's base region. This is indicated by the bright red shade seen in the top view. The top view also reveals that the new strut retains general z-x plane symmetry. This is expected as the same symmetrical diamond cross-section was maintained in the redesign. Comparing Figures 4.4a and b to Figure 4.1 it is seen that the global effects are similar with respect to the strut's interference in the flow field and the store's interference in the base region. This indicates any improvements made by the new strut will be identified locally in the base region of the cone.

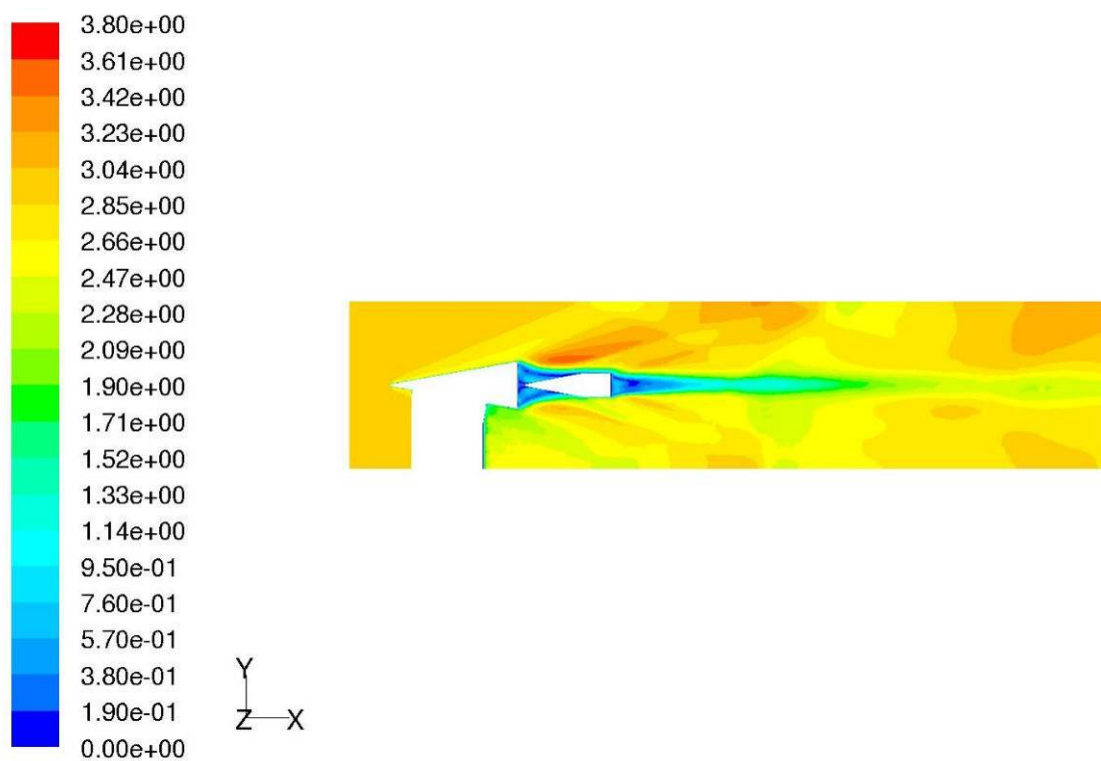


Figure 4.4a: New strut, stage 1, 2-D Side Contours of Mach Number.

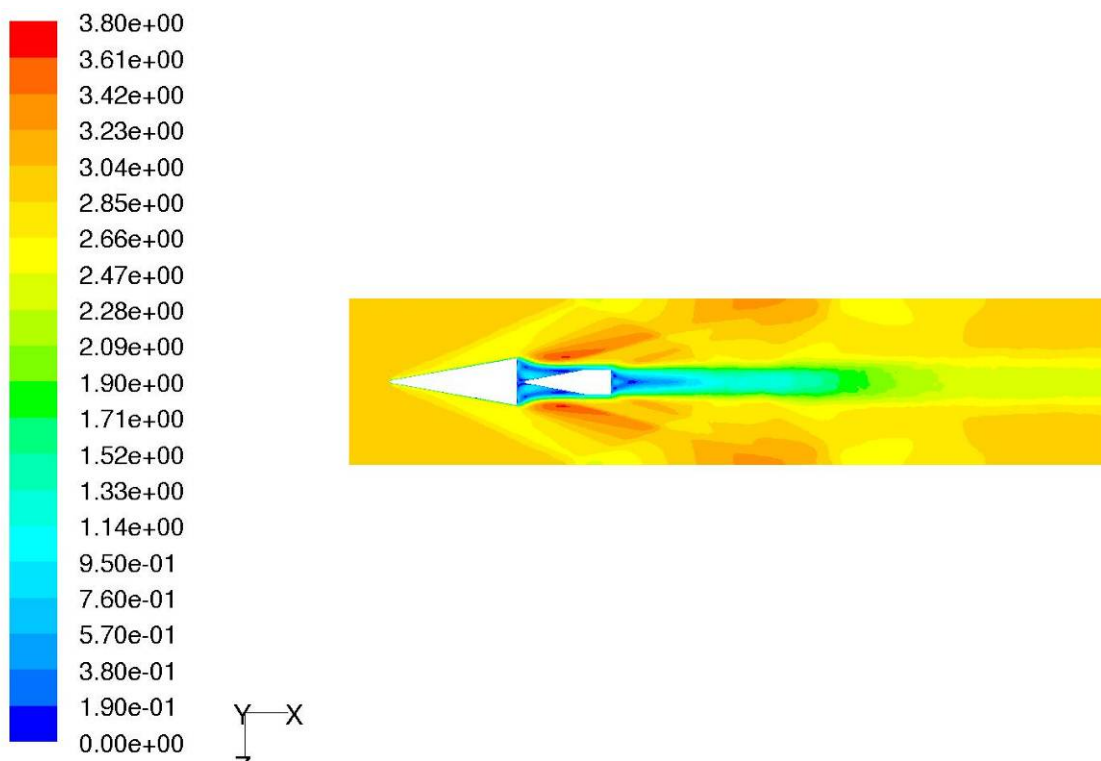


Figure 4.4b: New strut, stage 1, 2-D Top Contours of Mach Number.

New Strut, Stage 2: The fifth case completed when it reached convergence at 5,450 total iterations. Figures 4.5a and b display the side view and top view contour plots of Mach number for the strut, cone and store respectively. Similar to the original strut, stage 2 model, this geometry and mesh did not converge monotonically. Given the oscillating residuals, developed flow and minimal changes in store drag were used to judge convergence. Although the store is centered with respect to the cone's base, it appears that the trailing tip (reattachment point) of the cone's base is not completely symmetrical. This is most likely a result of the presence of the strut, as previous researchers have found [21, 36]. Comparing with the original strut, Figure 4.2a and b displays a very asymmetrical base region with an apparent split in the bottom area of the base region. The straight segment of the new strut will definitely reduce the tendency to turn flow however it may cause a drop in velocity. The initial formation of the reattachment shock can be seen in the darker yellow region directly above the store in the side view and to either side of the store in the top view.

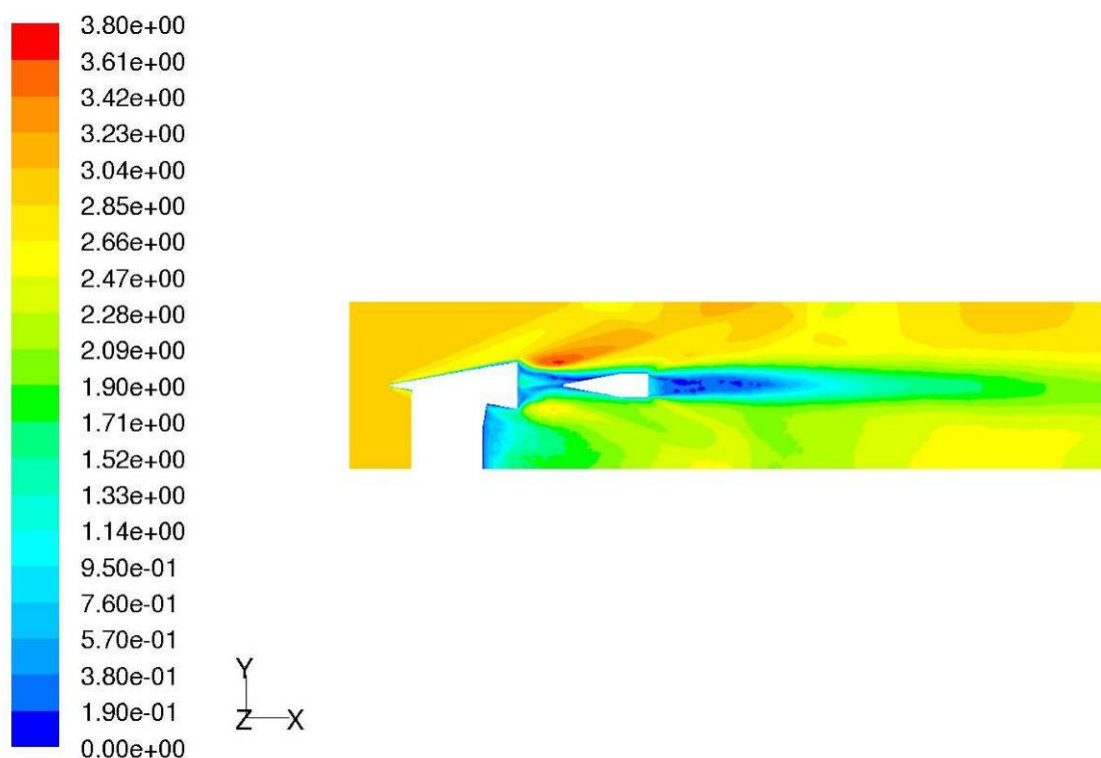


Figure 4.5a: New strut, stage 2, 2-D Side Contours of Mach Number.

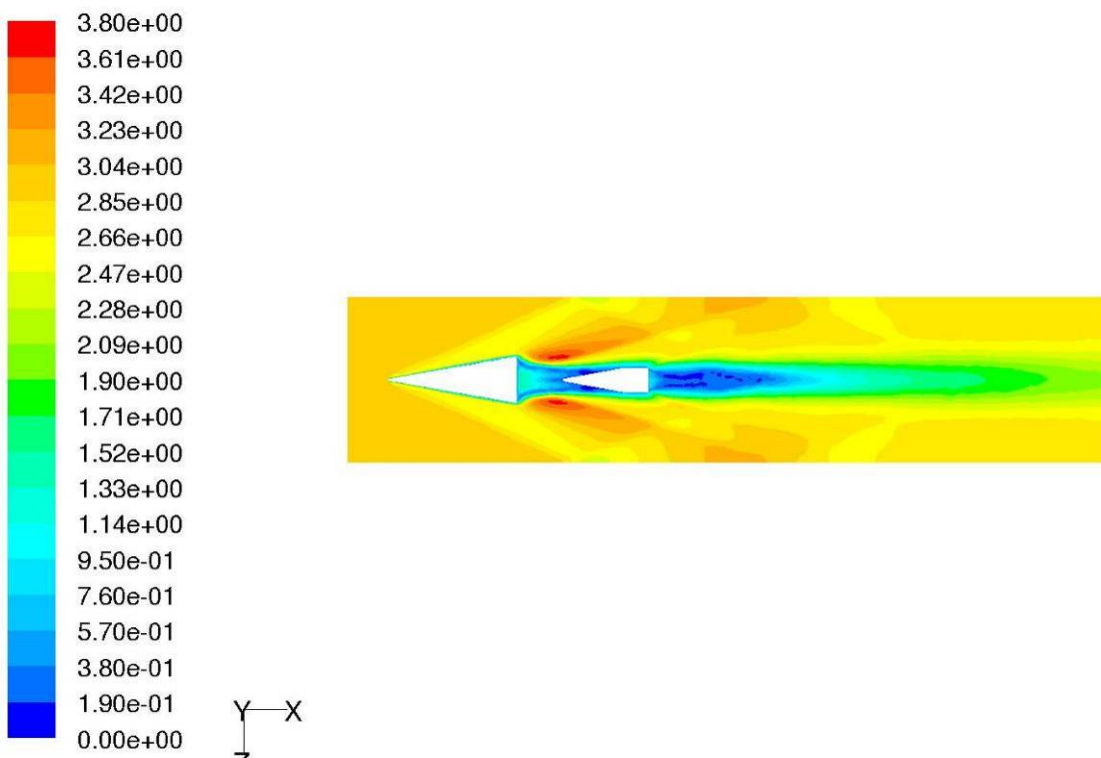


Figure 4.5b: New strut, stage 2, 2-D Top Contours of Mach Number.

New Strut, Stage 3: The sixth run completed when it reached convergence at 15,015 total iterations. Figures 4.6a and b display the side view and top view contour plots of Mach number for the strut, cone and store respectively. Similar to the original strut model of corresponding stage, the reattachment of the cone's wake can be seen. At this stage the store has exited the cone's base region and begins to see external effects. Formation of reattachment shocks and changes in the base regions of both the store and cone can be seen. The asymmetrical appearance of the store's wake with respect to the cone's wake may be an indication of unsteady phenomenon. Many of the observations from the original strut and stage 3 can be seen here. These include development of recompression waves and their reflections, restoration of the base regions to predicted shape and impingement of the reflected conical shock waves on the store.

To gain a better picture of which strut retains better base flow symmetry, enlarged plots of the base region will be introduced and comparatively analyzed.

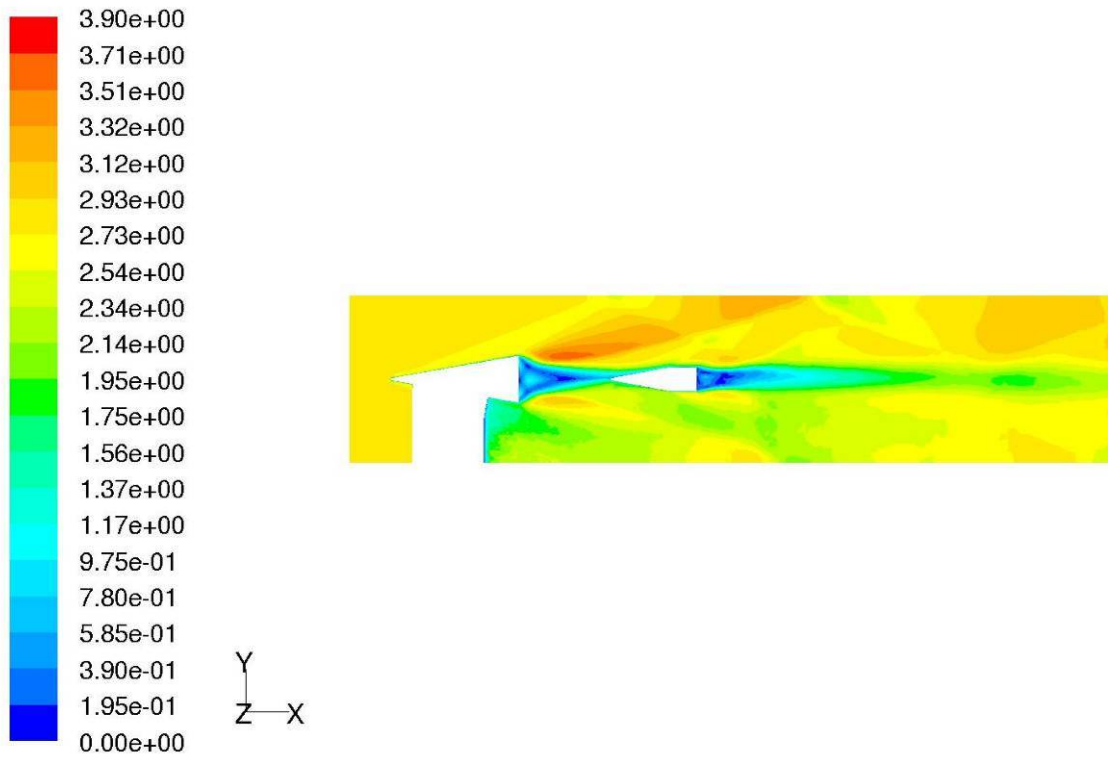


Figure 4.6a: New strut, stage 3, 2-D Side Contours of Mach Number.

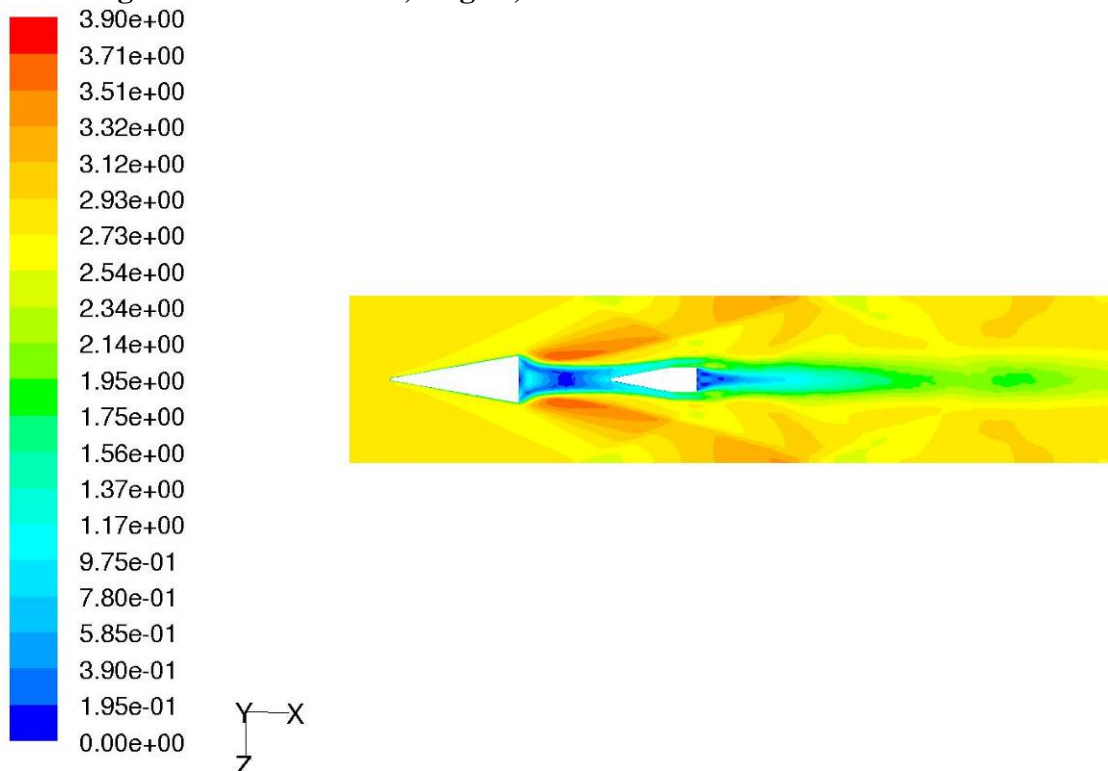


Figure 4.6b: New strut, stage 3, 2-D Top Contours of Mach Number.

Stage 1 Analysis In stage 1 the store introduces the greatest effect on the cone's base region since it occupies nearly all of it. Figure 4.7 shows comparative

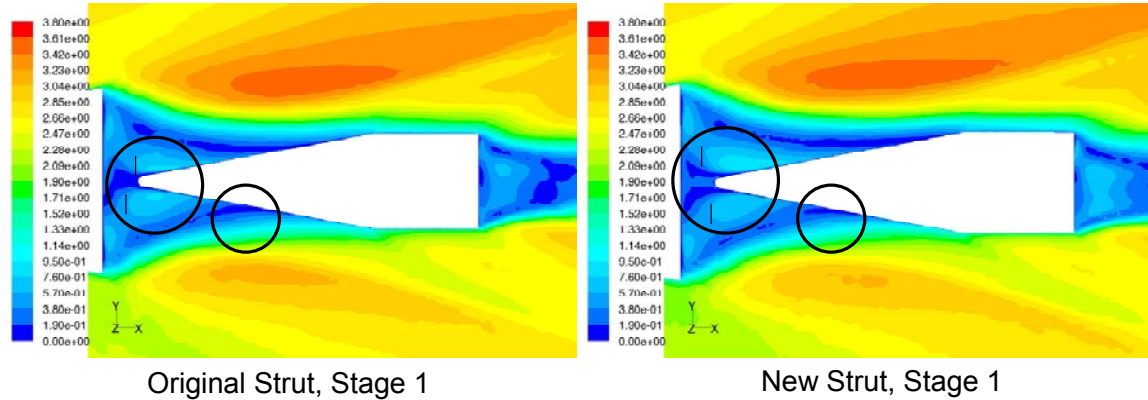


Figure 4.7: Stage 1 Comparative Side Contours of Mach number.

zoomed contour plots of stage 1. Comparing the regions in the smaller circles indicates that the new strut may be causing the base region to have a slightly narrower neck. The recirculation region encompassed by the larger circles appears to have greater top-bottom symmetry as a result of the new strut. Immediately adjacent to the tip of the store is a region of dark blue which corresponds to a Mach number near zero. From the original strut to the new strut, this lopsided subsonic region transitions to a split. The two regions resulting from the split are nearly equivalent yielding a more symmetric structure. This can also be analyzed from a top-down view. Figure 4.8 shows comparative contour plots of Mach number from the top of the wind tunnel looking down. While the global views indicate the z-x planes are typically symmetrical, the new strut brings some refinement. The boxed areas depict the variation in the dark blue region immediately incident upon the conical portion of the store. The new strut demonstrates better symmetry with respect to this region. In the near base region the new strut indicates some splitting of the subsonic region and slightly improved symmetry as seen in the side views. The black

lines demonstrate the asymmetry of the lighter blue region and its contact with the store.

From these visualizations, overall improvement in symmetry can be seen in the z-x plane

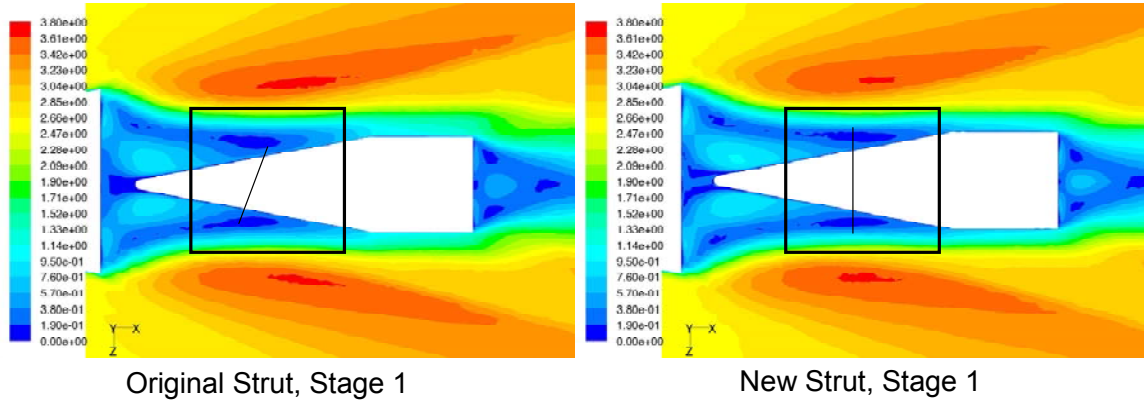


Figure 4.8: Stage 1 Comparative Top Contours of Mach number.

while it may be questionable for the same area in the x-y plane or side view. To gain further insight, Figure 4.9a and b show velocity vector plots for stage 1. What appears as a subsonic region in the Mach contours plots is actually composed of negative velocities with respect to free stream. Although the velocities congregate in the -300m/s range, a more balanced allotment of vectors is seen as a result of the new strut. The distinct shape of the recirculation region can be clearly seen. A detriment of the new strut is the slight reduction of the recirculation region on the bottom side of the store tip. Based on visualizations alone, the new strut clearly provides refinement in the top-down or z-y plane. In the side views it is not intuitively clear whether or not the new strut is superior to the original strut. While the region immediately adjacent to the store sees improvement, the region extending along the conical part of the store sees a detriment. Moving on to stage 2 will assist in full spectrum analysis.

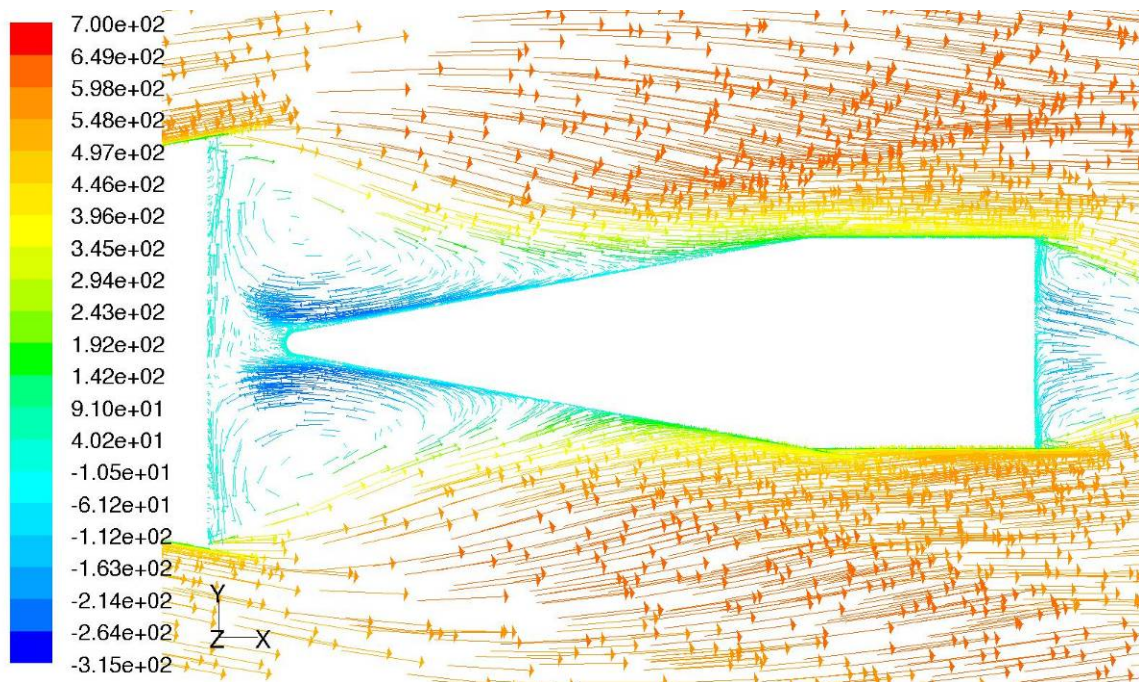


Figure 4.9a: Original Strut, stage 1, side view colored by X-velocity vectors (m/s).

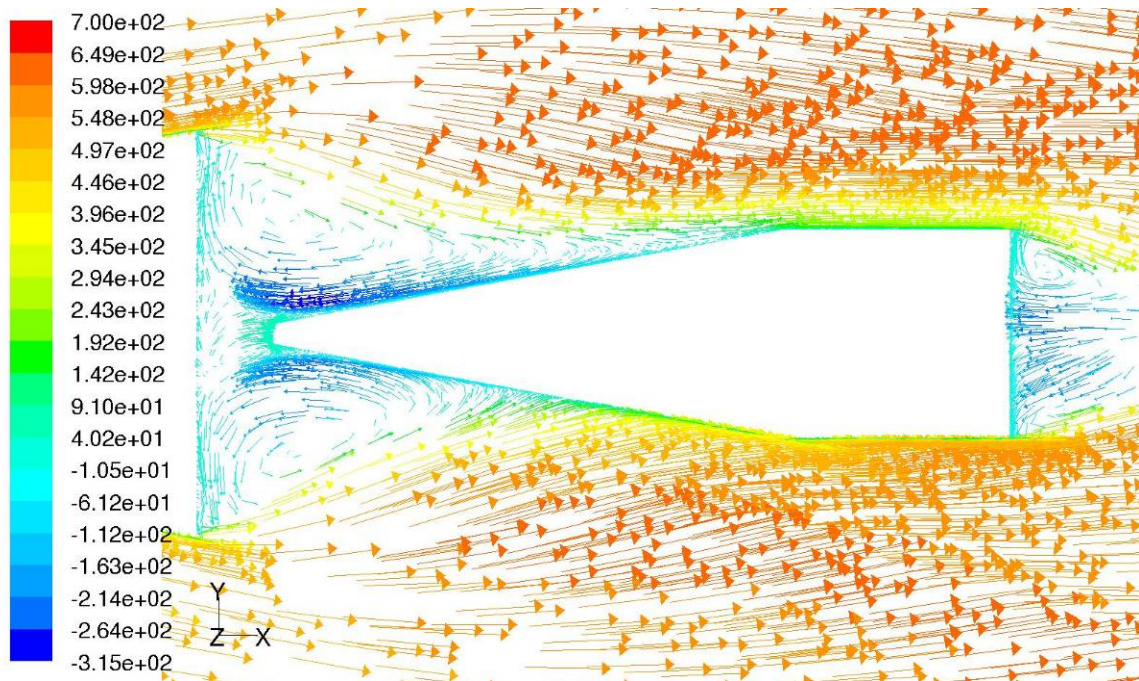


Figure 4.9b: New Strut, stage 1, side view colored by X-velocity vectors (m/s).

Stage 2 Analysis In stage 2 the store is starting to transition out of the cone's base region. Here the store interferes with the reattachment region of the cone's base. Figure 4.10 displays comparative contour plots of stage 2. The narrowing of the neck of the base region can be seen again. The presence of either strut appears to cause the recirculation region to shift upwards as identified in the global views. Although the new strut appears to cause the neck to narrow, the structure shows much better

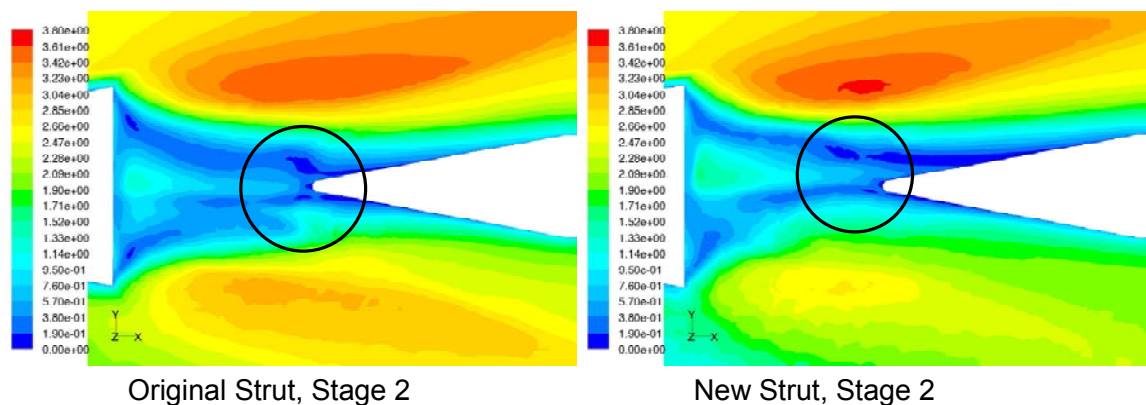
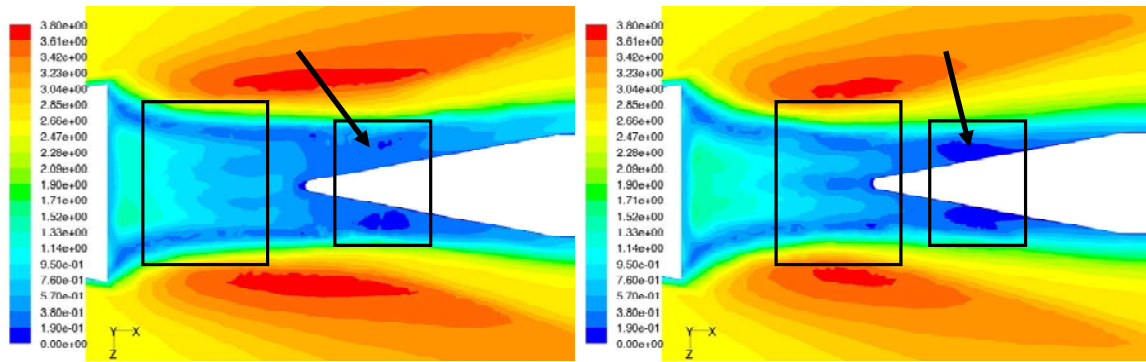


Figure 4.10: Stage 2 Comparative Side Contours of Mach number

symmetry than seen in the circled region for the original strut. This is likely the result of reduced velocity and increased pressure on the bottom side of the base region associated with reduced turning of the flow up into the top region. Figure 4.11 shows stage 2 comparative contour plots of Mach number from the top of the wind tunnel looking down. In this case the boxed areas clearly demonstrate that the new strut is superior to the original strut in maintaining flow symmetry. This is especially evident when viewing the dark blue regions. The lack of a low velocity region on the right side can be clearly seen. Additionally some lengthening of the cone's base region can be seen when comparing the light bluish-turquoise regions in front of the tip of the store. As seen in the global views, Figure 4.11 also shows the brightest red regions which indicate high Mach



Original Strut, Stage 2 New Strut, Stage 2

Figure 4.11: Stage 2 Comparative Top Contours of Mach number.

number and high velocity. The new strut contour plot reveals a reduction in the size of the red regions as a result of the reduction in flow being turned up and into the cone and subsequently accelerated through the aft expansion fans. Therefore reduction in this high Mach region indicates the new strut is a superior design. While the top views continue to demonstrate refinement in flow symmetry as a result of the new strut, the side views are analyzed using the velocity vector plots to strengthen the analysis. Figure 4.12a and b depict the velocity vectors for stage 2. Initially the plots do not appear to offer additional information over the Mach contours show in Figure 4.10. However, the interference caused by the store with the trailing edge of the cone's base region is significantly greater in the case with the original strut. This indicates that the best conclusions on the effects of the strut on the cone's base will be seen in stage 3, where the store has separated from the cone's base. In stage 3 the stagnation or reattachment points should be visible as well as the entire structure of the base region.

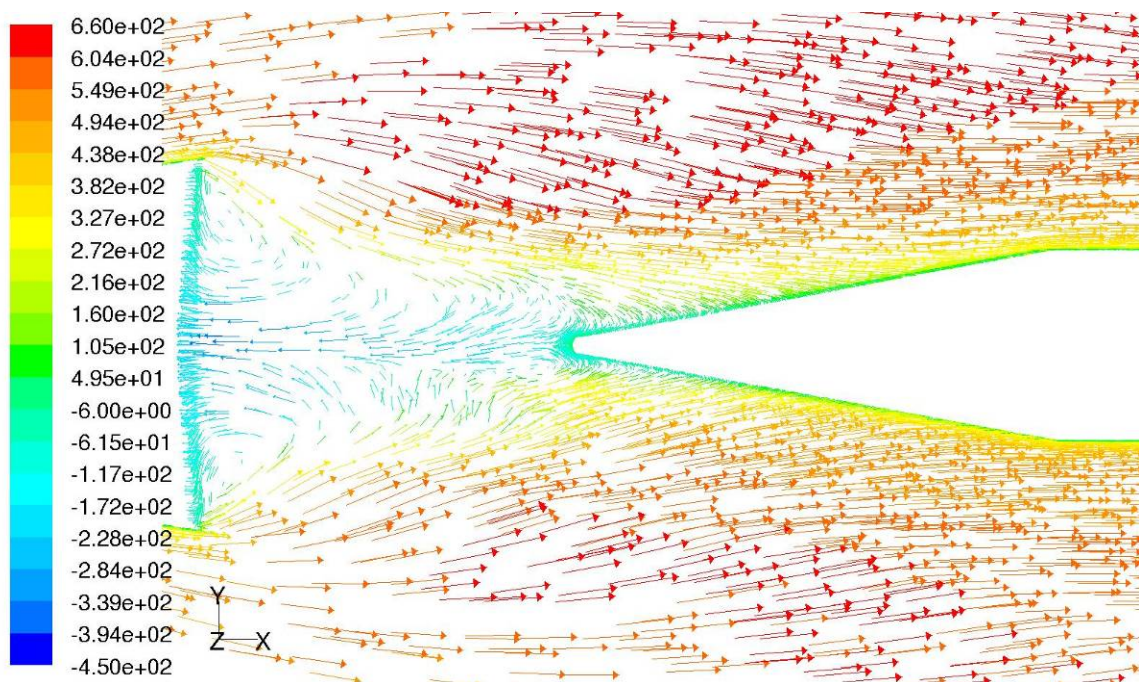


Figure 4.12a: Original Strut, stage 2, side view colored by X-velocity vectors (m/s).

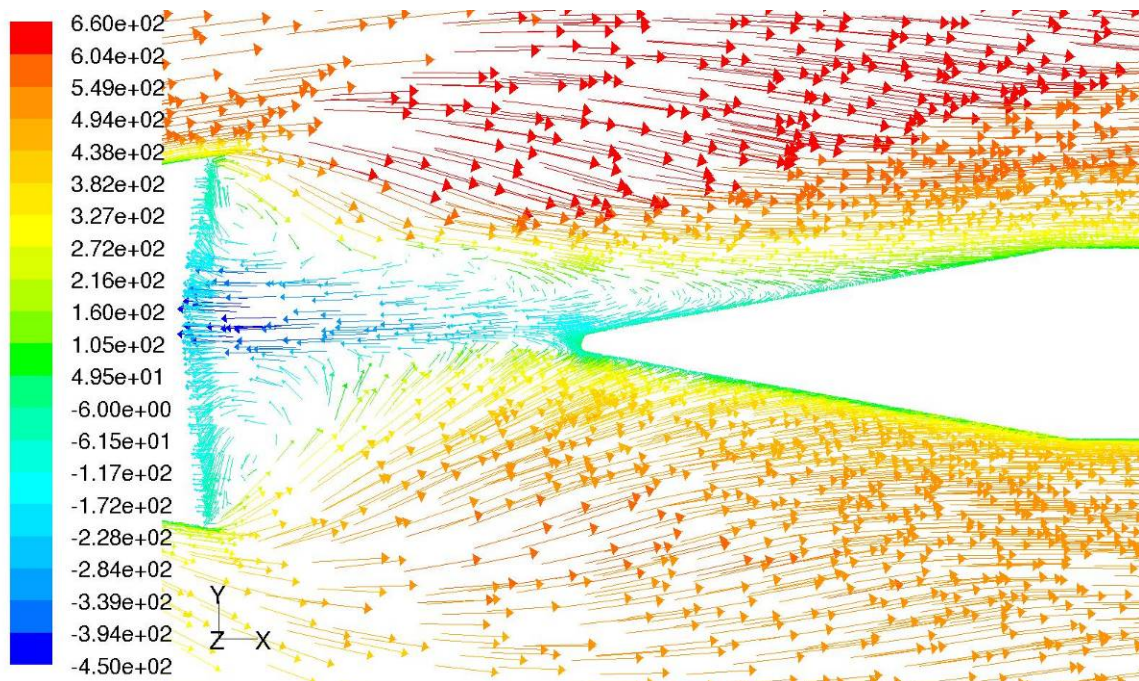


Figure 4.12b: New Strut, stage 2, side view colored by X-velocity vectors (m/s).

Stage 3 Analysis As learned from the global views, Stages 1 and 2 add the difficulty of the presence of the store in the cone's base region. The global views demonstrate that at stage 3 the store has completely transitioned out of the cone's base region. This allows the base region to return to the predicted structure identified in chapter 2. Therefore the enlarged visualizations of stage 3 are expected to provide the best comparative analysis. Figure 4.13 displays comparative plots of the base region in stage 3. The store is statically located at the same distance from the base of the cone.

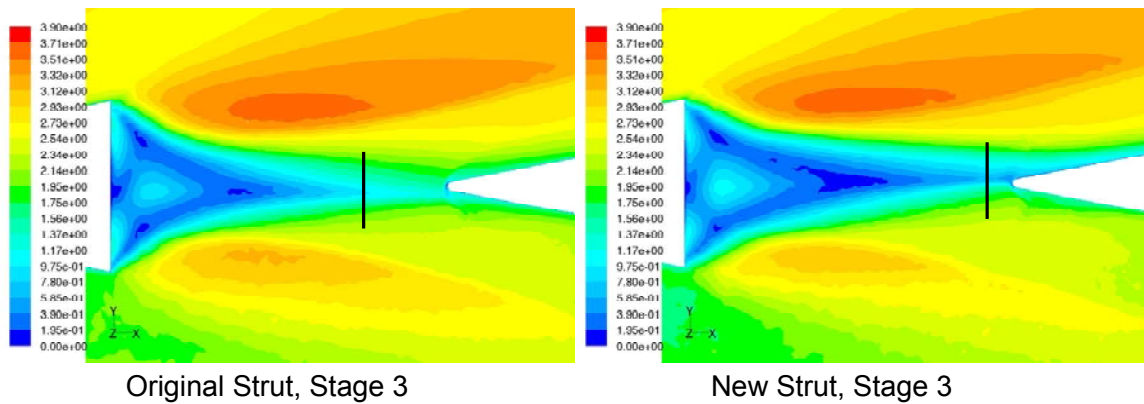


Figure 4.13: Stage 3 Comparative Side Contours of Mach number

While apparent symmetry can be seen in both struts, stronger symmetry can be seen in the base region where the new strut is present with respect to the recirculation region. As demonstrated by the black line, the new strut has accounted for considerable lengthening of the base region. This strongly supports the new strut as a better design for mitigating the tendency of a support to draw the reattachment point closer to the base [12, 21, 26, 31]. Figure 4.14 below shows the stage 3 comparative contour plots of Mach number from the top of the wind tunnel looking down. Although the termination of the base region is not as obvious as seen in the side view, the light blue to dark blue transition regions seen in the new strut contour plot are indicative of the base region terminating in

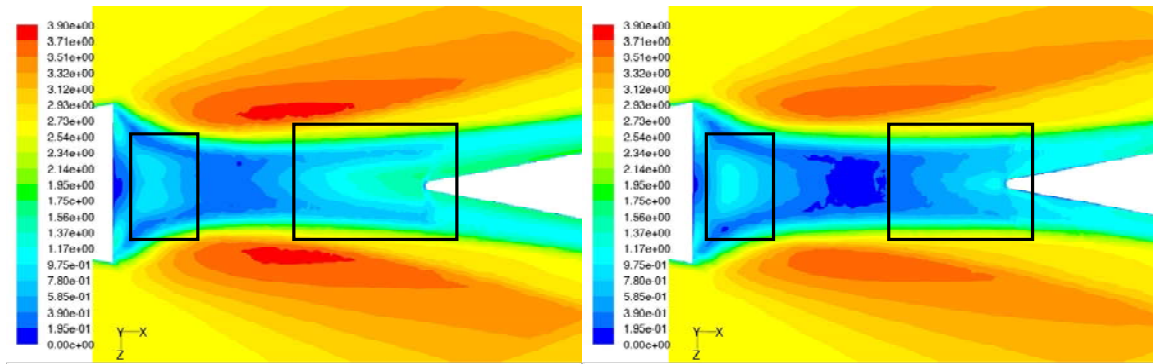


Figure 4.14: Stage 3 Comparative Top Contour Plots of Mach number.

the vicinity of the store tip. The contours corresponding to Mach number = 0.4 – 1 (light blue to turquoise region) seen with the original strut depicts a higher Mach number evident of the reacceleration from base flow. This acceleration can be assigned to the reattachment region in which recompression shocks generate as the flow transitions from subsonic to supersonic. Additionally, the reduction of the high Mach region on either side of the base region indicates a reduction in flow being turned up into the cone and traversing the shock expansion. Using the velocity vectors, it is possible to quantify the change in length of the trailing wake. Figure 4.15a and b both clearly show the termination of the cone's base region as indicated by the change in velocity. Figure 4.16 shows the follow-on step in which the non-dimensional location of the reattachment wake is determined. Observing where the velocity vectors meet head-on identifies the stagnation point. Since we know the reattachment point takes place immediately after the stagnation point, we can conclude that measuring where the stagnation point is will suffice for determining the length of the trailing wake. Using the cone's base diameter to obtain the non-dimensional distances, it was found that the new strut accounted for a 27% increase in distance from the cone's base to the stagnation point. Recall from chapter 2

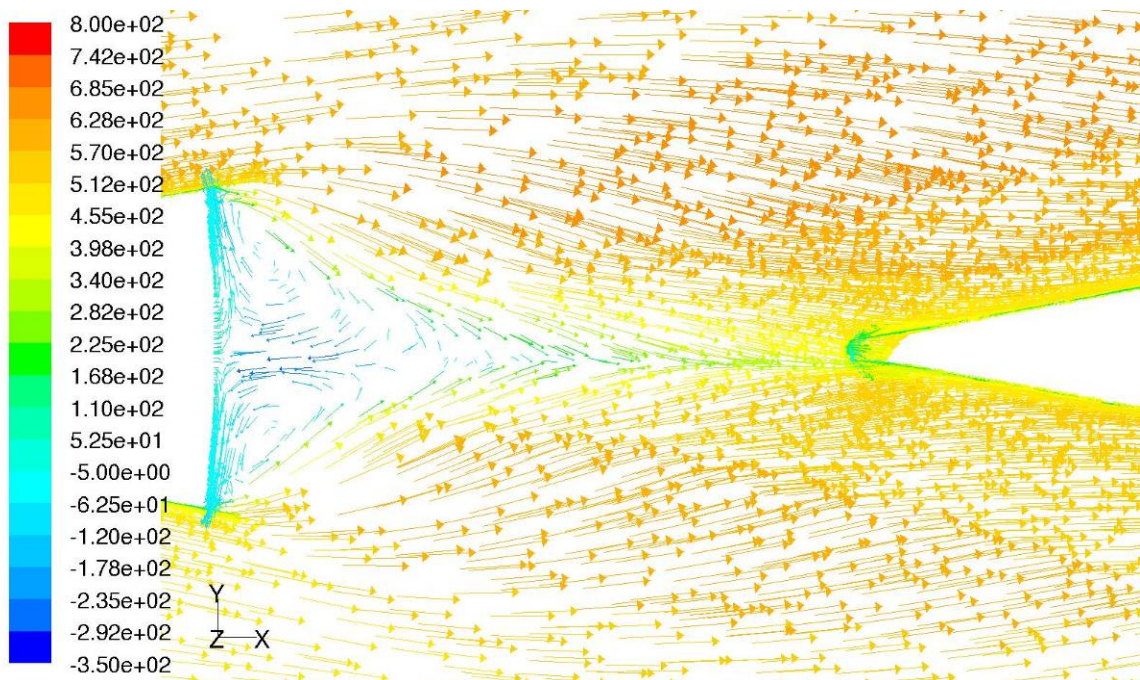


Figure 4.15a: Original Strut, stage 3, side view colored by X-velocity vectors (m/s).

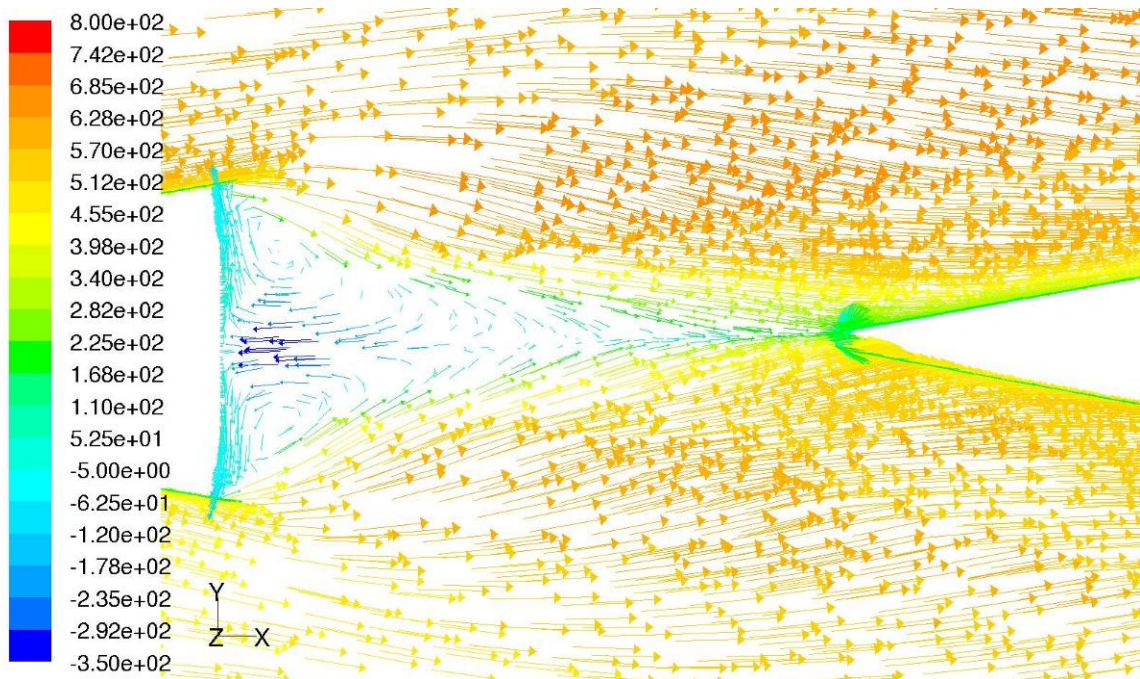


Figure 4.15b: New Strut, stage 3, side view colored by X-velocity vectors (m/s).

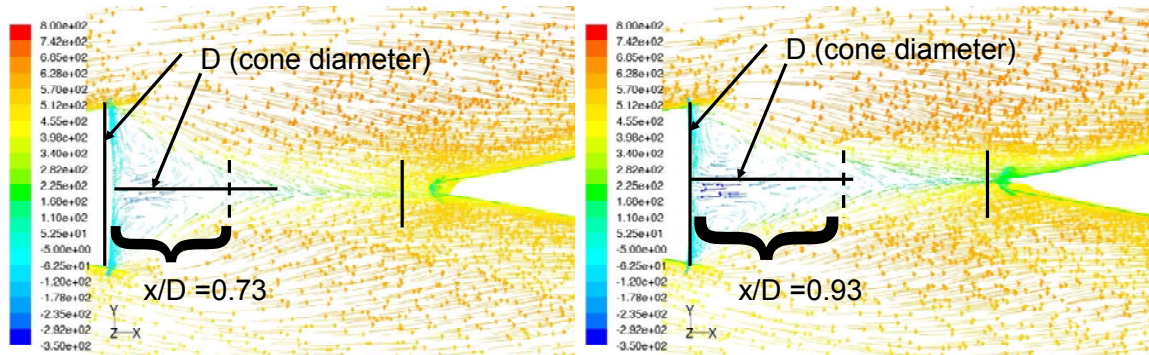


Figure 4.16: Stage 3 comparison, side view colored by X-velocity vectors (m/s).

that observations from Dayman’s free-flight experiments indicate as much as a 20% reduction in the distance between the reattachment point and the base of the cone as a result of the presence of the wires. Comparable with Dayman’s studies, Martellucci and Agnone discovered that their “Configuration B” which consisted of smooth bands with sharp edges was superior to standard wires because no noticeable wake propagated from the bands into the base region. Combining the findings from these two previous studies with the visualization results from current research indicates that a thin, sharp-edged underbody strut oriented perpendicular to free stream flow but accommodating the test vehicle shock angle provides a better mounting configuration than the simple swept design. To add credibility to this indication, the results and analysis of the transverse loads acting on the store will be investigated.

4.3 Transverse Force Comparison

Conical base flow at zero angle of attack on an axis-symmetric body should ideally be perfectly symmetrical in what has been defined here as the y and z planes. The 2-dimensional recirculation region approximates a 3-dimensional donut-shaped vortex attached to the base of the cone. For an equally axis-symmetric store, the forces imparted

onto the store from the cone's base flow should cancel each other resulting in the magnitudes of the y-component and z-component forces equaling zero. It should be noted from previous discussion that the store is only exposed to the cone's base region in stages 1 and 2. By the time the store has reached stage 3 it has exited the base region and the dominant forces are from reflected shock waves, shear layer compressions and potentially the formation of a shock wave off the tip of the store. Although the force coefficients are plotted for all 3 stages, the magnitudes for stages 1 and 2 will be examined to help resolve the inconclusive findings from the visualizations for stage 1 and 2. Therefore, it is assumed the strut that imparts the lowest magnitude of y and z-component forces is causing the least influence on the cone's base flow and is therefore the superior design. Figure 4.17 is a plot of the y-component force coefficients. It can be

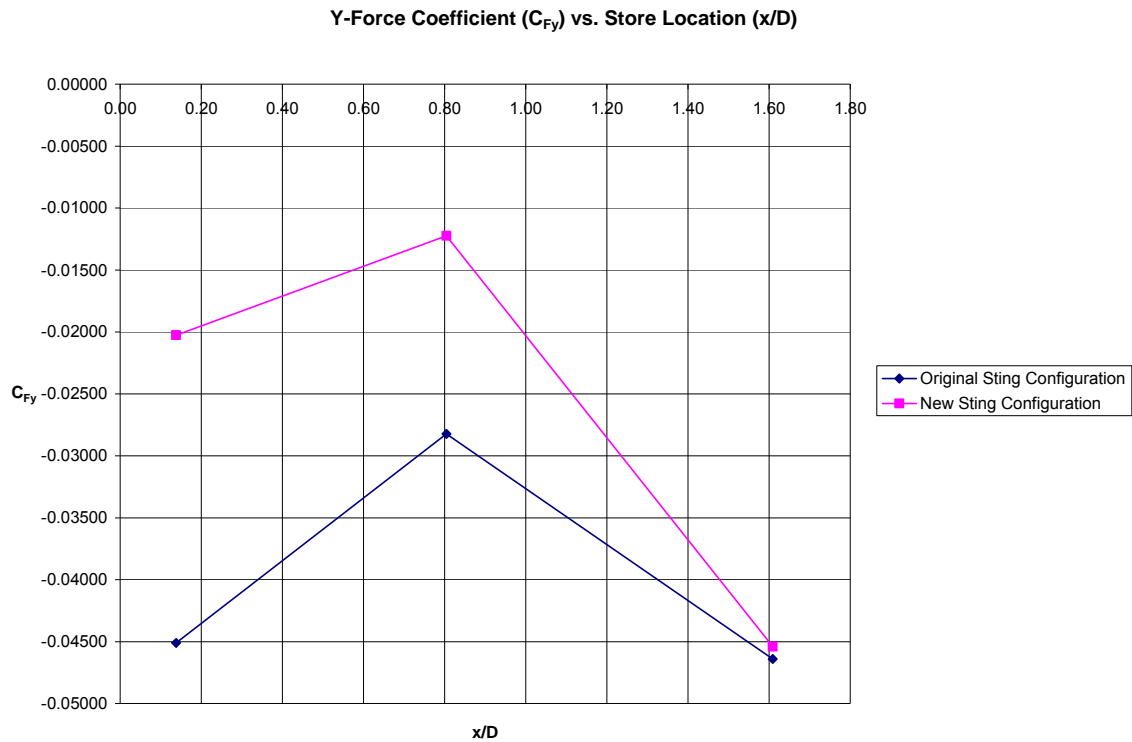


Figure 4.17: Plot of Y-component force imparted to store.

seen for stage 1 that the new strut accounts for a 45% reduction in force coefficient. For stage 2 the new strut accounts for a 42% reduction in the force coefficient indicating that the new strut is unanimously superior at reducing load disturbances in the base region.

Figure 4.18 is a plot of the z-component coefficient of forces. For stage 1 and 2, the new strut accounts for approximately a 30% reduction in the z-component forces.

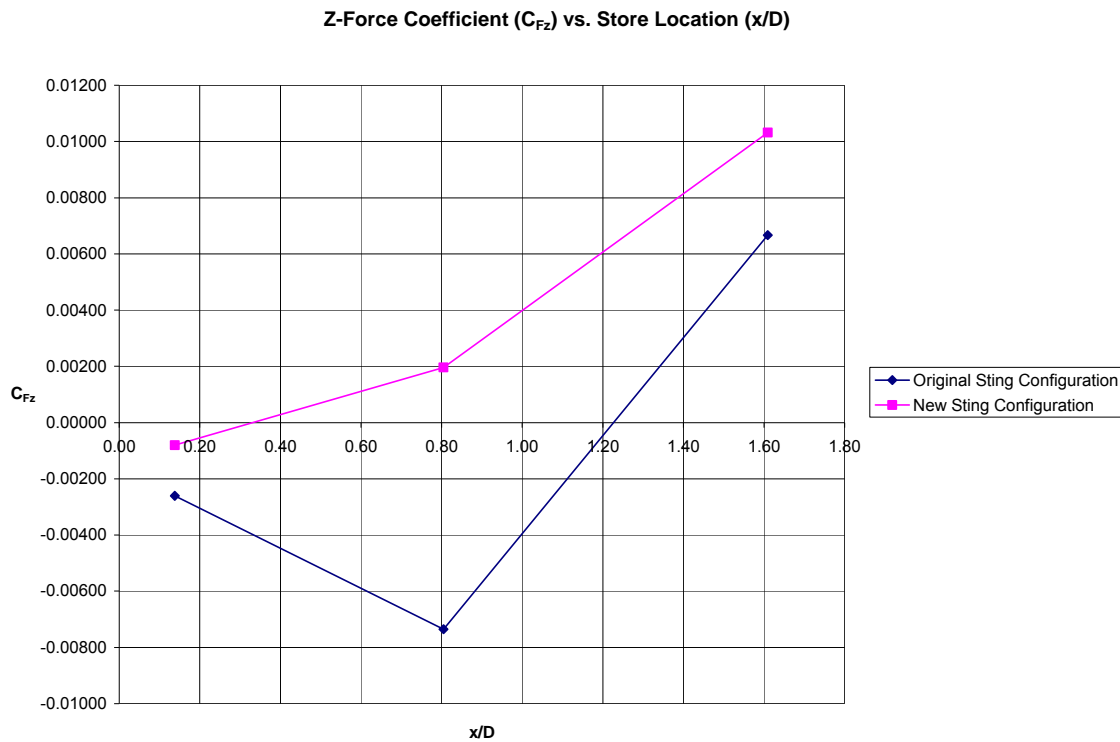


Figure 4.18: Plot of Z-component force imparted to store.

An interesting observation is that the new strut causes the z-component force to transition from negative to positive (left to right looking from the store's base towards the tip). A small perturbation in the base flow field would likely initiate a small oscillation whereas a large perturbation generated by the strut would generate a large oscillation. The magnitude of the change in force from stage 2 to stage 3 for the new strut is .00836

whereas the magnitude of change in force from stage 2 to stage 3 for the original strut is .01403. The change in magnitude for the original strut is 68% greater than the magnitude of change for the new strut. This method of analysis indicates the new strut is superior to the original strut.

To validate this method, figures 4.19 and 4.20 show the same y and z component force coefficients with Simko's computationally determined y and z-component coefficients added. Note that his forces are only for the original strut and cone with cavity. At $x/D = .22$, Simko's results are within 10% of the current results for the original strut configuration. At this location the new strut comparatively demonstrates nearly a 50% reduction in the force coefficient which is comparable with

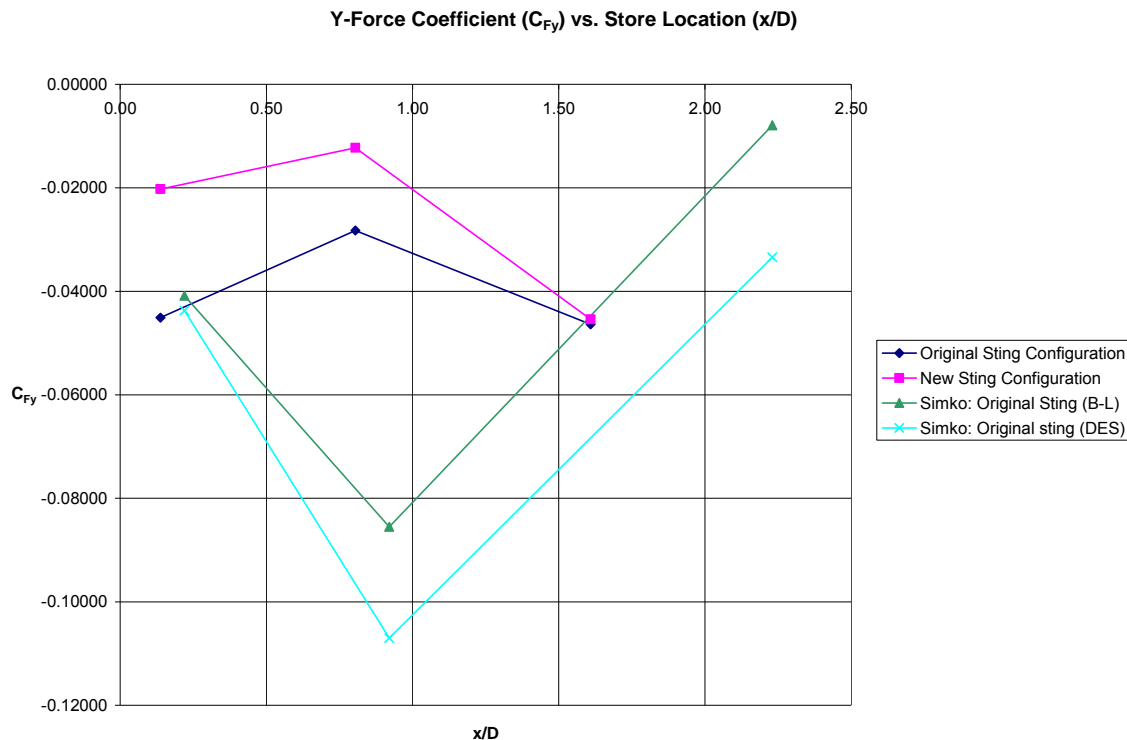


Figure 4.19: Comparative Plot of Y-component force imparted to store.

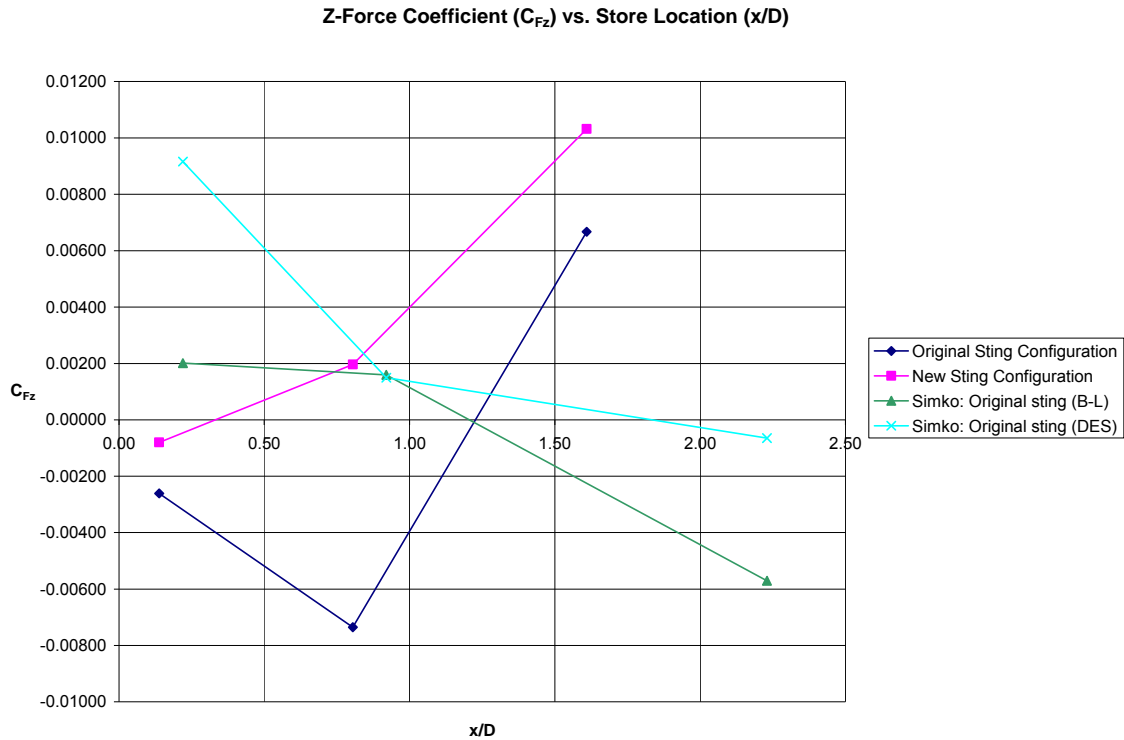


Figure 4.20: Comparative Plot of Z-component force imparted to store.

the 45% reduction seen previously from current results alone. Although Simko's stage 2 results don't coincide with the current results for the original strut, the new strut demonstrates significant improvement over all results for the original strut. The new strut demonstrates better reduction in y-component forces in stages 1 and 2 than the original strut as compared with k-ε, B-L or DES. Current data doesn't extend to x/D=2.23. Simko's B-L and DES models show little agreement with the k-ε model for the original strut in trend. Since we are only concerned with magnitudes, it is important to point out that the magnitudes for x/D=.14 (current) and x/D=.22 (Simko, B-L) vary by 29% with each other for the original strut. When these magnitudes are compared with the new strut, they both vary by more than 60%. For stage 1 (x/D=.14 current or .22 Simko), the

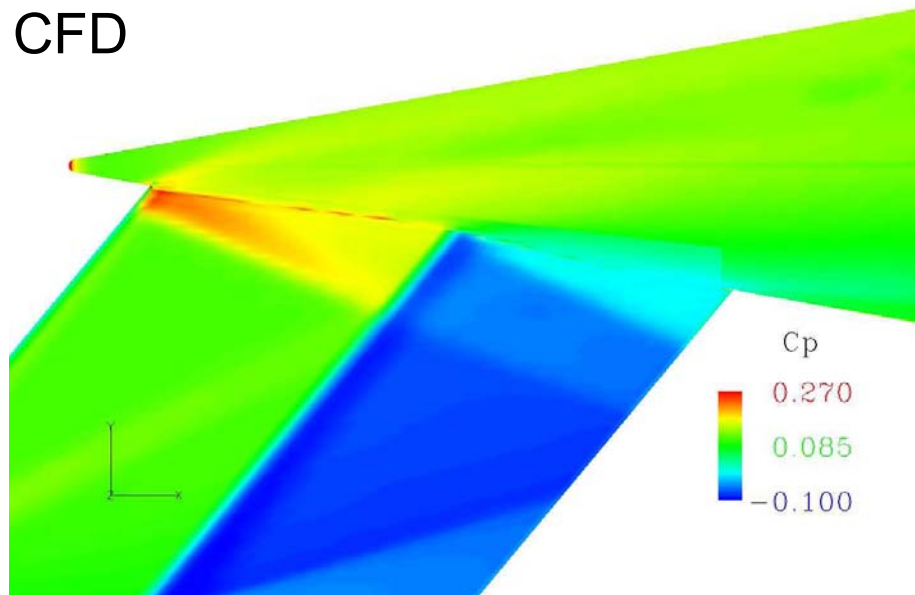
DES model is given less attention since it's magnitude lies outside of the magnitude range of the B-L and k- ϵ models for both struts. Therefore, although current z-component results do not closely match they tend to support the conclusion that the new strut provides better reduction in z-component forces than the original, namely in the near base region or x/D less than or equal to 0.50 with the exception of the DES model at $x/D=.22$.

Analysis of the y and z component forces adds credibility to the findings from the flow visualizations. The use of different methods of analysis strengthens the conclusion that the new strut is superior in mitigating base flow disturbances. The last method consists of pressure distributions to completely resolve the superior strut.

4.4 Cone and Strut Comparison

In addition to the force coefficients and visualization comparison of the store and cone base region, one last method seeks to examine the cone and strut without the store. In previous experimental research a Pressure-Sensitive Paint (PSP) model was made [21, 22]. Additionally, CFD research used pressure coefficient contours on the strut and cone to observe the pressure distribution and compare the strut effects [21, 36]. These are comparatively depicted in Figure 4.21. The high pressure region associated with the free stream flow impinging upon the cone and strut can be identified. Additionally, the general shape and relative location of the conical shock wave interacting with the strut can be seen. Both methods show general agreement in the range of pressure coefficients (C_p) and the visual effects. This validates the CFD predictions with the actual experimental results quantified via the PSP. The reference area used to calculate the C_p

CFD



PSP

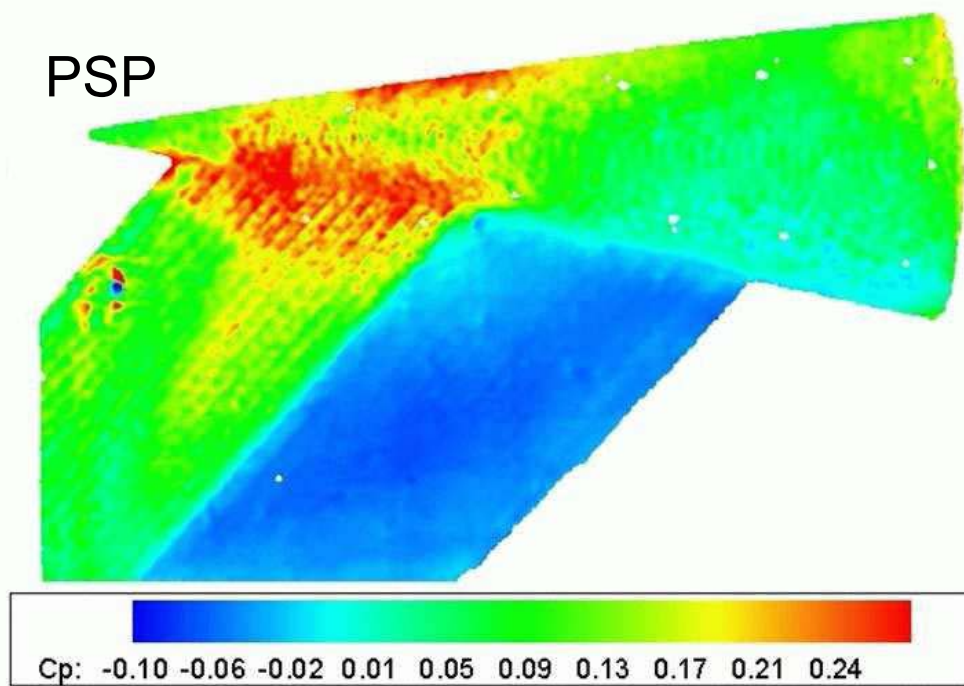


Figure 4.21: Pressure Sensitive Paint and CFD comparison of C_p [36].

is $A_{\text{ref}} = 363.5 \text{ mm}^2$. Present research has utilized the CFD to develop a comparative contour plot of pressure coefficient. The calculated reference area is $(A_{\text{ref}}) = 366 \text{ mm}^2$ which is within 1% of Simko's calculated reference area [36]. Figure 4.22 depicts the pressure coefficient contours of both the original strut and new strut. In general the contour plot of the original strut in Figure 4.22 agrees with the CFD and PSP images in Figure 4.21. This lends further support to the current CFD and previous research methods and results. Comparing the original strut with the new strut reveals that the new strut mitigates the effects of turning flow up into the cone. The centerline is identified and the ovals indicate that the new strut retards higher pressure flow towards the top surface of the cone. It also reveals that the top and aft portion of the cone is subjected to a lower range of pressure coefficients, a result of the reduce turning of the flow up into the cone. The boxes and angled arrows indicate the high pressure region incident where the shock waves interact on the strut is also mitigated by the new strut. Current research comparatively demonstrates good agreement with previous research in the strut effects on the original strut and cone. The coefficient of pressure distributions on the new strut and cone indicate the desired improvements over the original strut.

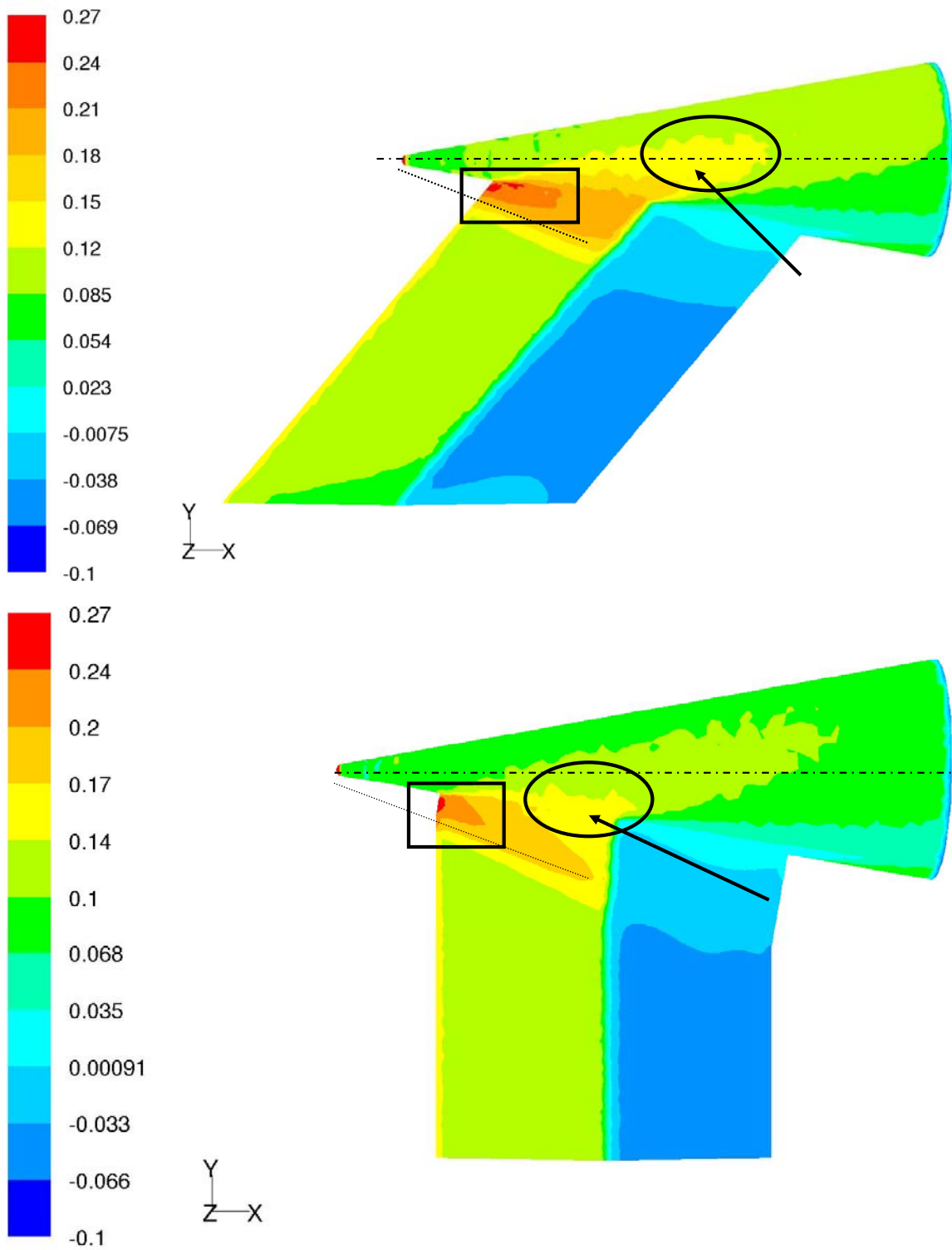


Figure 4.22: Original and New Strut comparison of C_p .

4.5 Cone Base Pressure

Another indicator of strut performance is the base pressure plots of the cone. The base pressure plots were obtained by selecting a line perpendicular to the conical axis of the cone approximately 1 mm behind the base of the cone. The pressure coefficient is calculated using the cone's reference area ($A_{ref} = 366 \text{ mm}^2$). In the following pages, several plots display the calculated pressure coefficients. Since the earlier contour plots showed general symmetry in the top views, only the side view is examined to evaluate symmetry. The cone's base region falls between 42 mm ($4.20\text{e}+01$) and 66 mm ($6.60\text{e}+01$) as measured from the wind tunnel floor. Figures 4.23a and b compare the cone's base pressure plot at stage 1 ($x/D=0.14$). The new strut improves the symmetry of the base region by nearly 100%. This can be seen at the starting points, indicated by the circles. The difference between the circled endpoints is approximately $0.085 - 0.075 = 0.010$ or around 5% of the total range of pressure coefficients in the plot. The lowest values of C_p near the center of the cone's base remain relatively unaffected from the strut effects. As discussed earlier, the stage 2 plots do not present as strong of an indication of the benefit of the new strut with respect to the symmetry of the base flow. This is shown in Figure 4.24a and b. It appears that the new strut may decrease the flow symmetry in this stage. This is the only stage that shows the small hump in the near base region between 50 and 60 mm shifting. A similar conclusion is drawn from observations of the contour plots. The shifting of the pressure in the near base region takes place very close to the tip of the store. With unsteady effects dominating as the store transitions out of the cone's base region, it is likely that the store introduces the degradation of symmetry to a

greater effect than the strut. Therefore it is possible that the asymmetry seen in the edges of the base region in stage 2 is amplified by the store transitioning out of the base region. Since some convergence issues were encountered when calculating stage 2, it is logical to assume that unsteady and non-linear effects from the store's presence are presiding in this situation. Therefore the CFD results in stage 2 at best provide an approximation of what is taking place. This conclusion is drawn because moving onto stage 3 the base pressure sees much better symmetry as a result of the new strut without the store's presence in the cone's base region as seen in Figure 4.25a and b. Differentiating the original strut endpoints results in ~ 0.015 . Differentiating the new strut endpoints results in ~ 0.006 . Comparing the relative difference in pressure coefficient indicates that the new strut improves the stage 3 flow symmetry by approximately 60%.

Based on the analysis it is safe to conclude the new strut accounts for a reasonable improvement in base flow symmetry for stages 1 and 3. The new strut coupled with the unsteady and non-linear effects of the store transitioning out of the cone base region account for a notable deterioration in symmetry. The combination of analytical techniques from the CFD adds further evidence to the proposition that the thin, sharp edged, combination strut with a diamond-shaped cross-section is among the optimal configurations for an underbody mount.

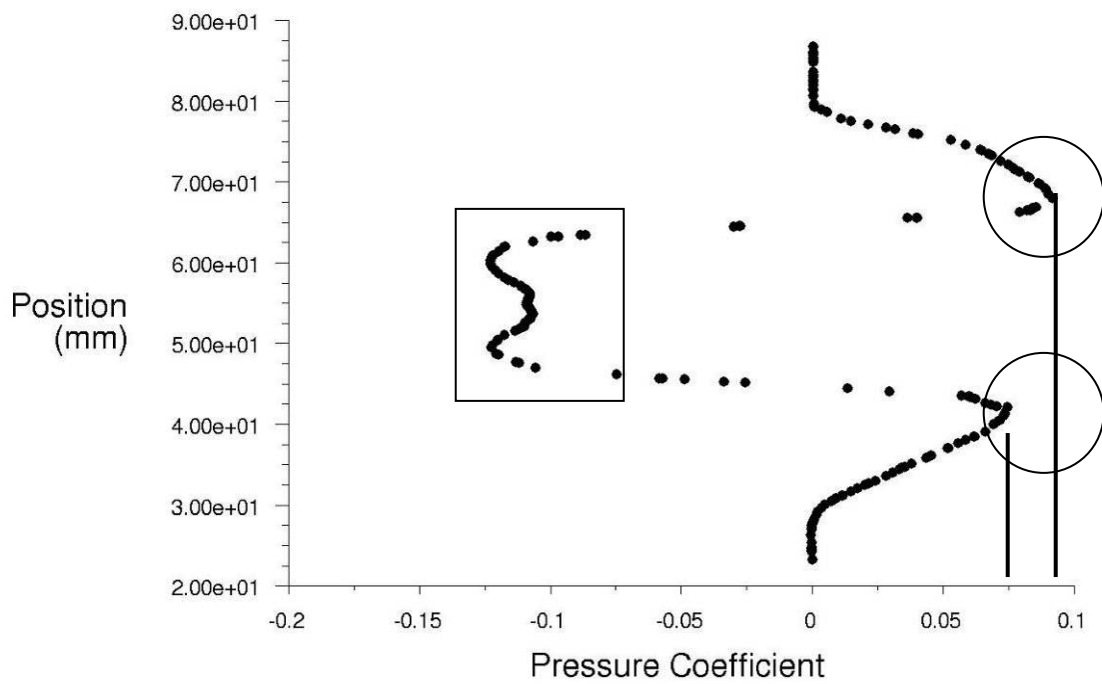


Figure 4.23a: Original Strut, Base Pressure Plot ($x/D=0.14$).

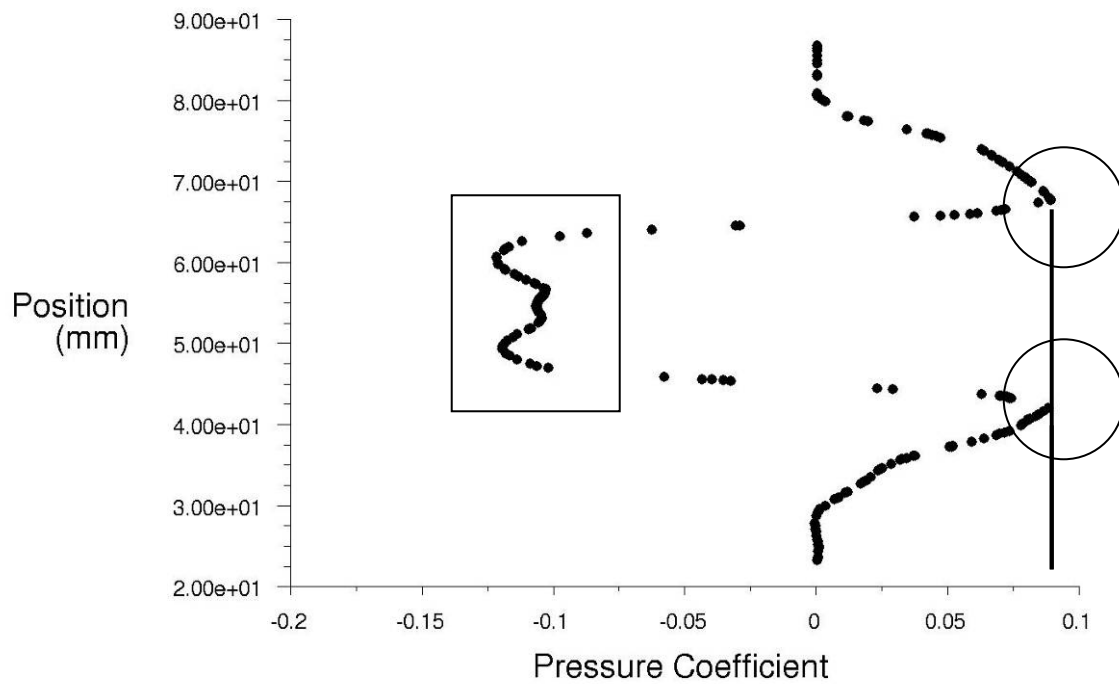


Figure 4.23b: New Strut, Base Pressure Plot ($x/D=0.14$).

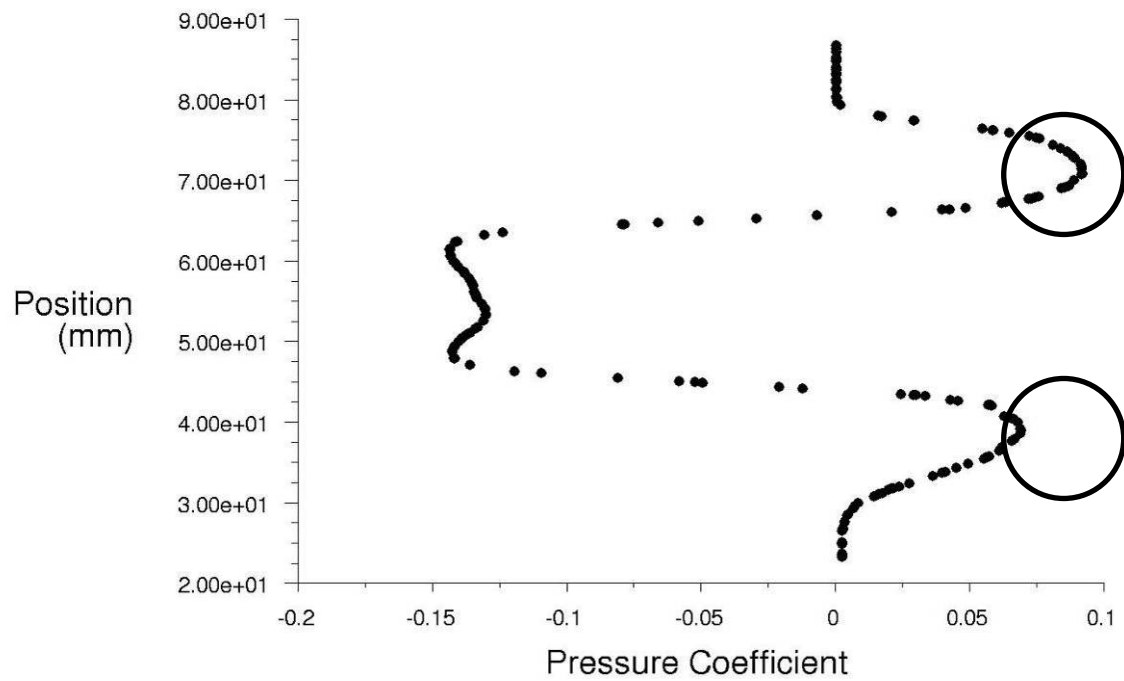


Figure 4.24a: Original Strut, Base Pressure Plot ($x/D=0.80$)

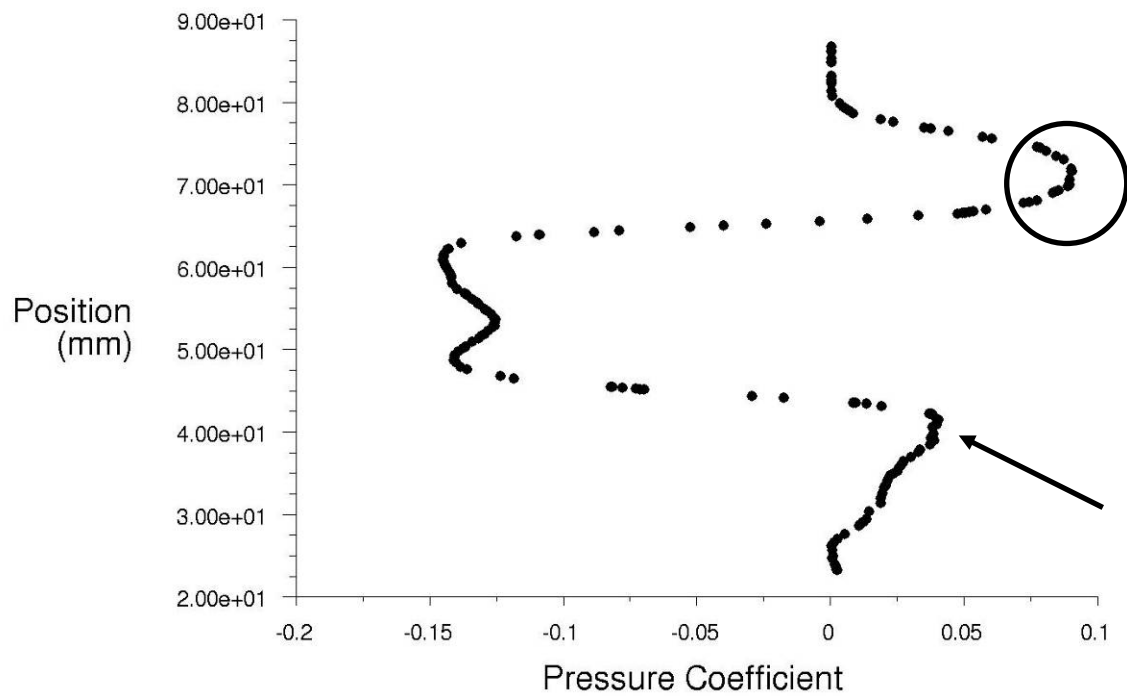


Figure 4.24b: New Strut, Base Pressure Plot ($x/D=0.80$)

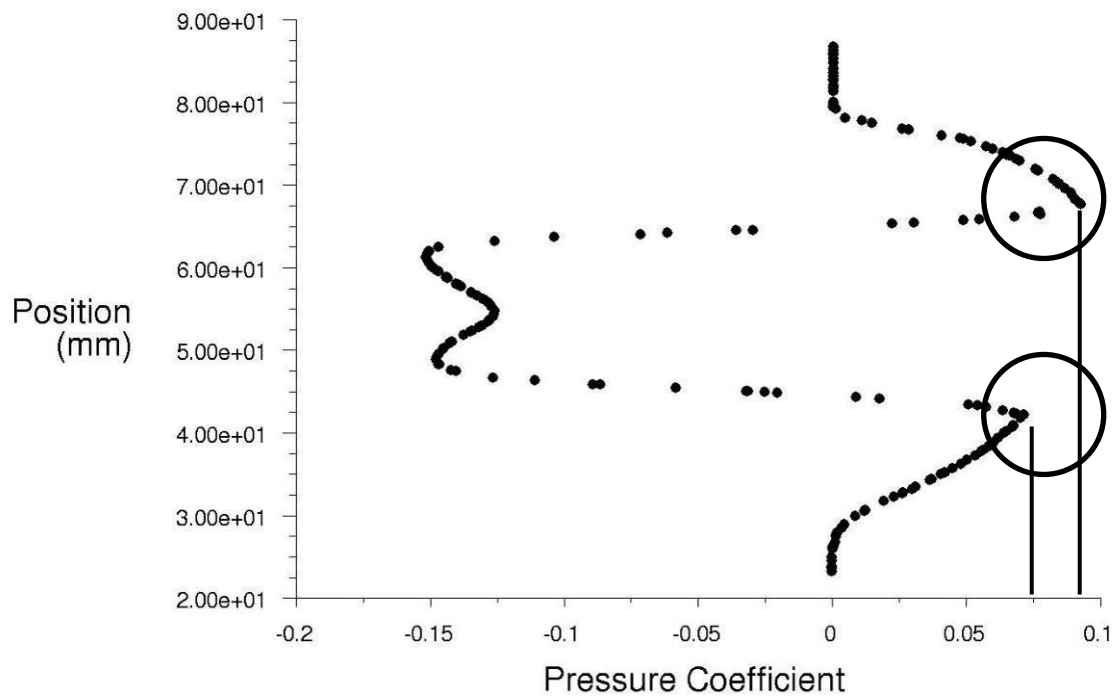


Figure 4.25a: Original Strut, Base Pressure Plot ($x/D=1.61$)

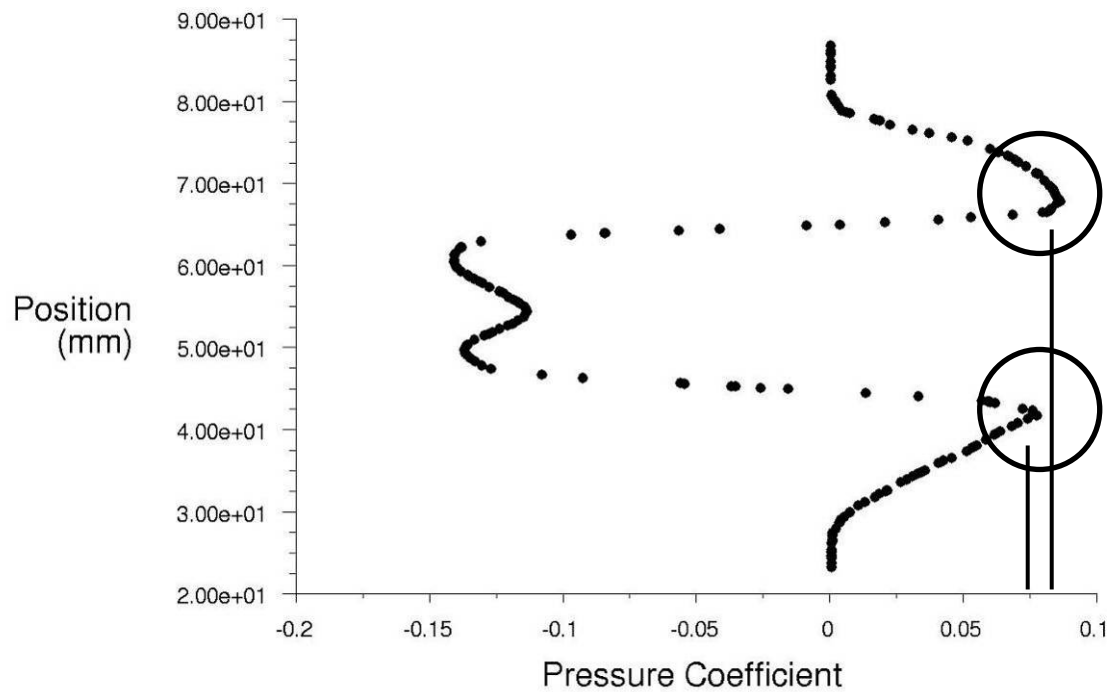


Figure 4.25b: New Strut, Base Pressure Plot ($x/D=1.61$).

A final point of analysis is to compare the effect of the struts on the axial loads. Figure 4.26 compares the axial force coefficients between the new and original struts. The x-direction signifies positive stream wise direction from the readers left to right. The y-direction denotes horizontal-plane increments, in which positive corresponds to bottom-to-top. The z-direction denotes vertical-plane increments, in which positive is directed out of the page. It is apparent that for incrementing stages, the original strut accounts for a more linear relation of the axial loads while the new strut accounts for lower values in the near and far wake regions with a notable spike in the middle. Averaging the original strut coefficients and then the new strut coefficients indicates that the new strut accounts for a 2% average increase in the axial loads acting on the store.

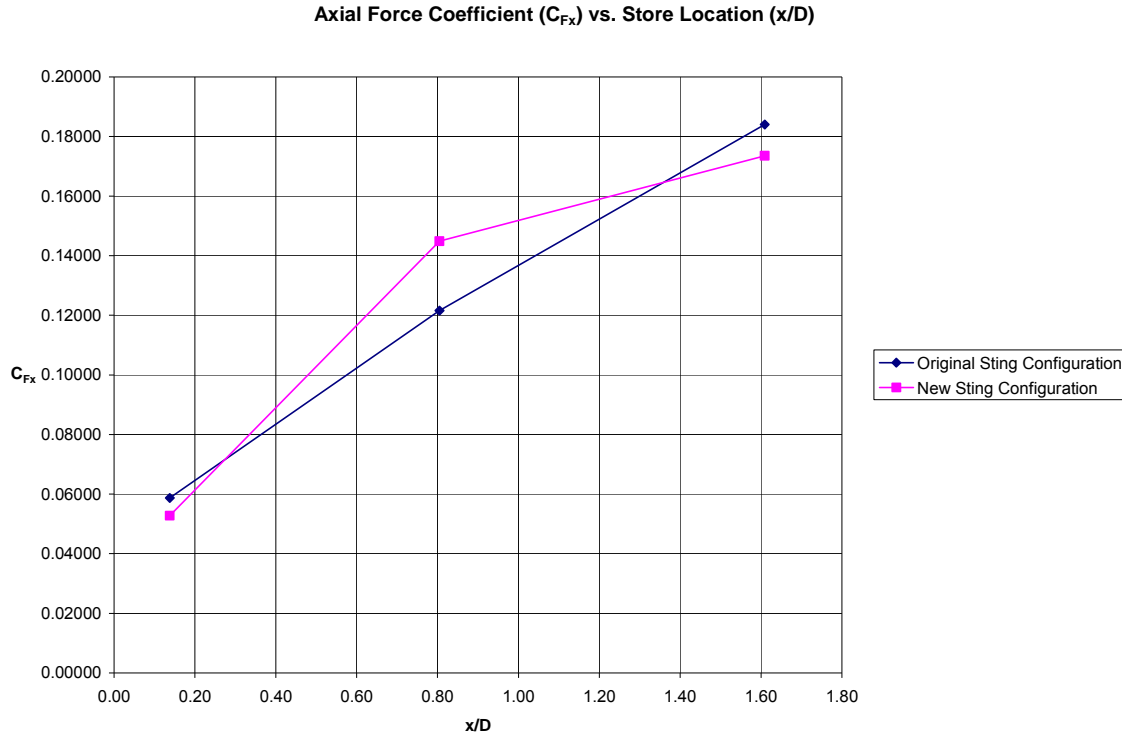


Figure 4.26: Plot of Axial Force Coefficients.

V. Results and Analysis of the Axial Loads

5.1 Chapter Overview

This chapter includes the CFD and experimental results as they pertain to the axial loading on the store. To simplify the analysis, the axial loads are presented as non-dimensional force coefficients. Various sections highlight a particular method in which the force coefficients are analyzed. The second section introduces CFD predictions. These values and trends should match to some degree the values obtained from the experimental data. The third section introduces the experimentally obtained values and trends. The fourth section presents comparative plots evaluating the correspondence of experimental data to CFD data.

5.2 CFD Axial Force Coefficients

The highlighted column in Table 5.1 denotes the axial force coefficients determined from the current CFD. These values are plotted in Figure 5.1 to better observe the trend. As expected, as the store retreats from the cone's base region the axial force increases. The increase in axial loading appears to be smooth without any violent transitions or surges. The greatest increase in loading is seen between stages 1 and 2 where the slope of the line is approximately 0.14 as compared to the slope of the line between stages 2 and 3, which is 0.04. By the time the store is at stage 2 or half of the store's length, 80% of the increase in axial load has occurred.

New Strut Configuration, Entire Store				
Stage	x/D	C_{Fx}	C_{Fy}	C_{Fz}
1	0.14	0.05276	-0.02027	-0.00080
2	0.80	0.14486	-0.01224	0.00196
3	1.61	0.17353	-0.04540	0.01032

Table 5.1: Coefficient of Forces (C_F).

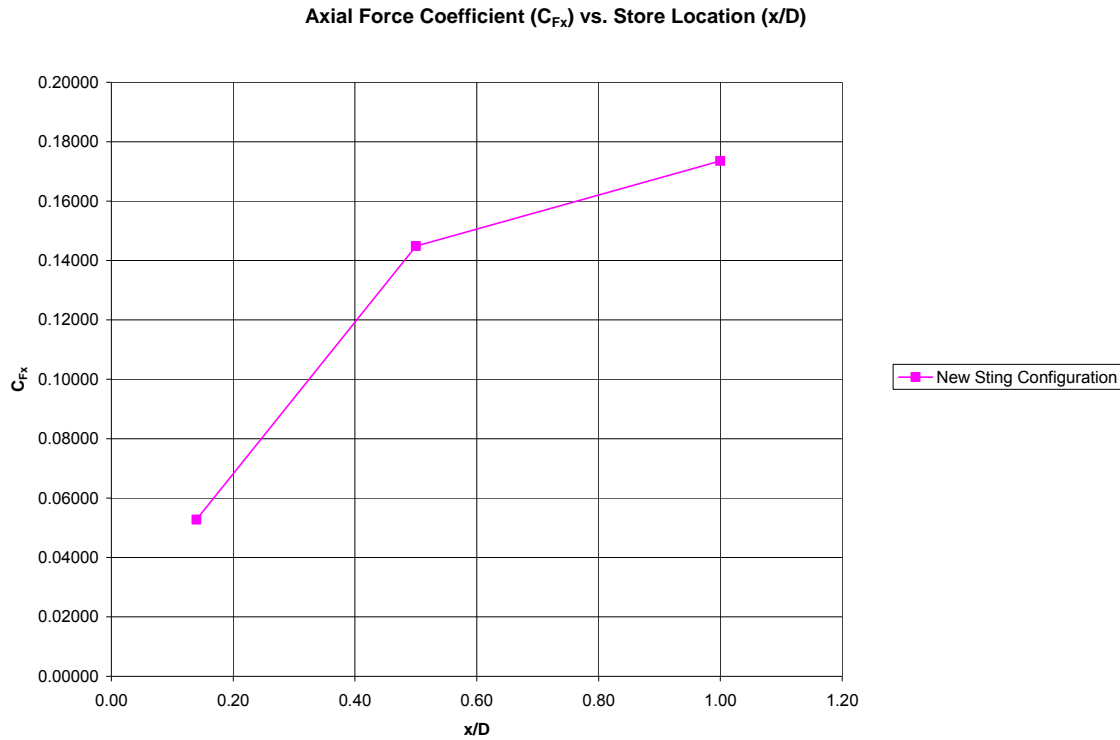


Figure 5.1: Axial Forces (C_F) from CFD for New Strut.

Comparing current CFD results with previous CFD results has helped validate the current computational research and results so far. In like manner comparing the current CFD load predictions with previous CFD load predictions should result in a confident CFD prediction from which to compare the experimental results. Figure 5.2 shows a comparative plot of the current CFD with previous CFD research results available. The plot compares the force coefficients on the store in supersonic base flow. As indicated in the legend, the current CFD predictions are based on a solid cone only. Simko concluded that the Baldwin-Lomax (B-L) turbulence model gives valid approximations for the base region while the Detached Eddy Simulation (DES) is proven to be adequate for computing shear layers and separated flows [36]. Therefore the best standard to compare

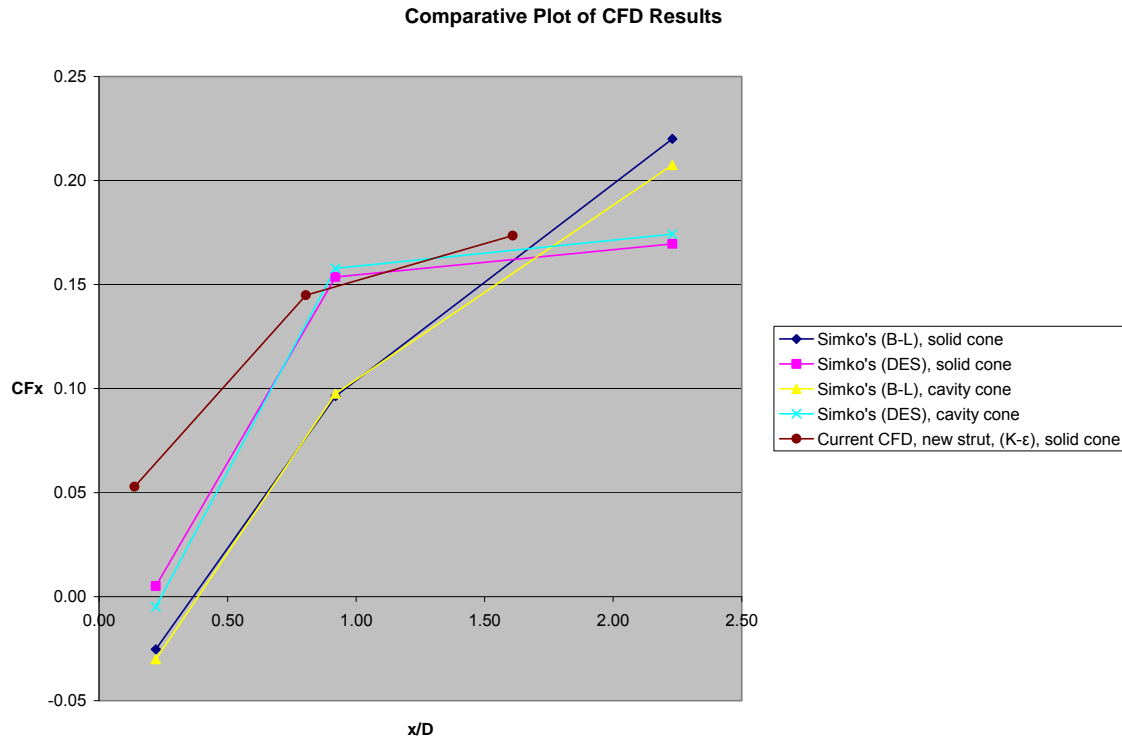


Figure 5.2: Comparative plot of current and previous CFD results.

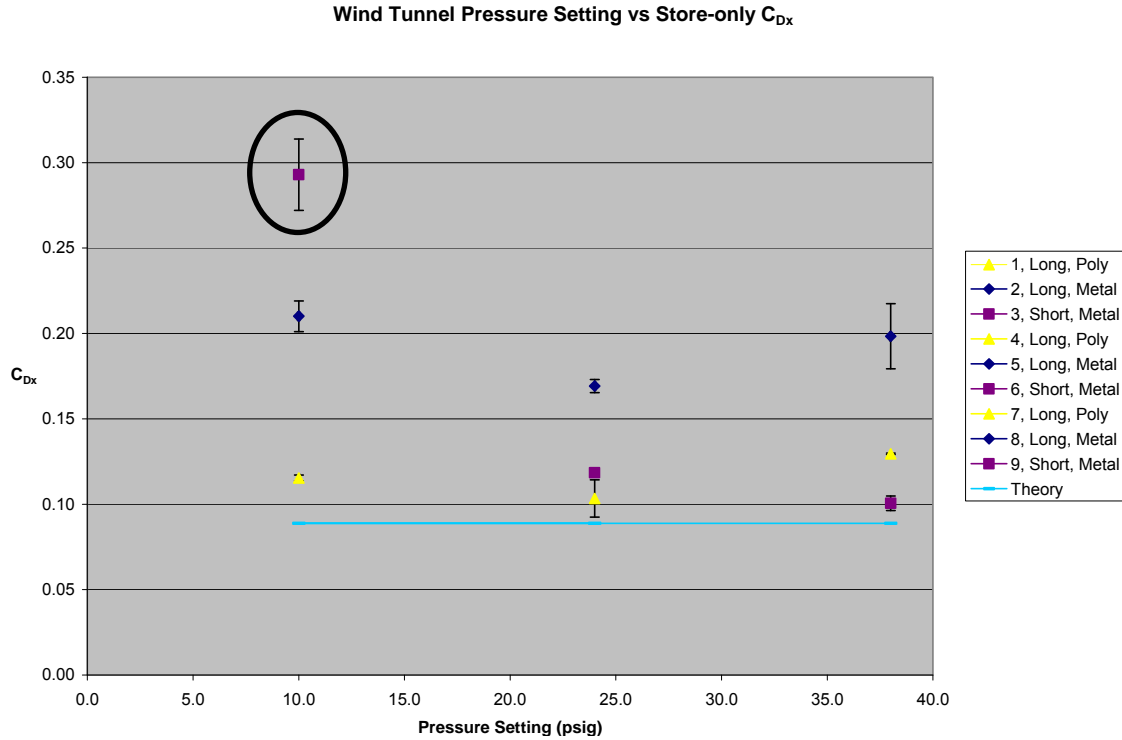
current research to is the DES and the B-L models for the solid cone, with a slant towards the DES model due to its strength with separated flows [36, 45]. These are identified by the light blue and magenta data series respectively. When comparing current k-ε results with Simko's results for the near base region ($x/D = 0.14$ to $x/D = 0.22$), it is apparent that computational determination of the of axial force coefficients it is more dependent on the type of turbulence model implemented than whether the cone is solid or has a cavity. It can be concluded the physics of the cavity cone as compared to the solid cone are difficult for the varying turbulence models to agree on. Since Jung concluded the cavity had little effect on the cone's base pressure [21], it should follow the cavity also has little effect on the axial loads in the base region when the store is not in the cavity. Overall,

the CFD results indicate that regardless of turbulence model or cavity/no cavity, the general aerodynamic effect is an increase in axial loading as the store transitions from $x/D=0.14$ to $x/D=2.23$. For the solid cone and original sting, comparing the magnitudes from the current steady state k- ϵ model with the unsteady DES model reveals an order of magnitude variance for stage 1. However, for stage 2 and stage 3 only a 6% and a 3% variance is seen respectively. Obviously the steady state k- ϵ model tends to over-predict the axial loading on the store, especially in the cone's base region. Additionally, 50% of the cases, the two current k- ϵ models plus Simko's DES model of the solid cone, indicate the store never sees a negative axial load in the "transition" region. The second DES model (cone with cavity) shows that at $x/D=.22$ the store's axial load is -0.004854 which is effectively 0.00 or a "null" force. Based on these observations, the current steady-state k- ϵ model is comparable to the previous CFD models completed. It is concluded that the k- ϵ model provides a confident prediction that is slightly high when compared to the previous results.

5.3 Experimental Axial Force Coefficients

Before examining the force coefficients on a store immersed in a complex base region, it is useful to first examine the axial coefficients present on the store exposed only to free stream air flow. Figure 5.3 depicts the axial force results for the various configurations tested. Since more than one run was performed at each respective setting, the error bars account for the deviation from the average as computed using Equation (3.11). The theoretical predictions were made using the Taylor-Maccoll solver to deduce

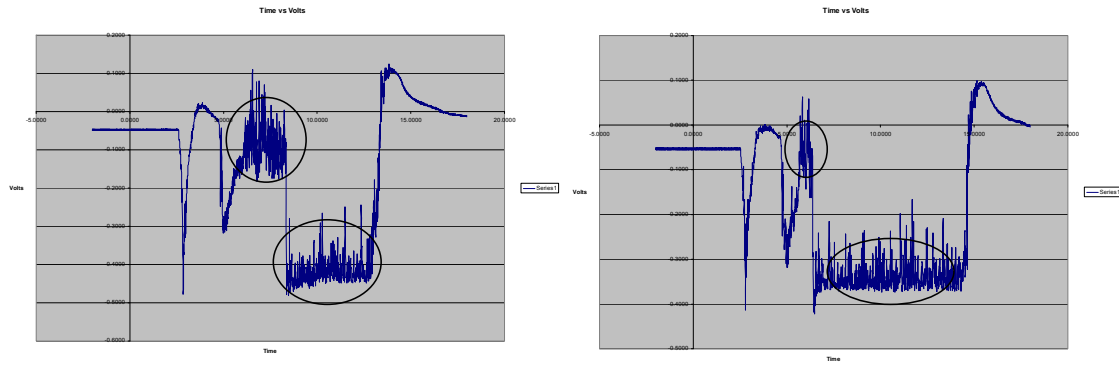
P_c/P_∞ where P_c is the pressure distribution over the surface of the cone and P_∞ is the supersonic pressure. The value for P_∞ was derived by accounting for the base pressure



and averaging the values across each respective tunnel pressure setting (see Appendix D).

The store's base pressure was approximated using the free stream supersonic pressure of 8066 Pascals. Since base pressures are typically lower than free stream supersonic pressures [21:15, 19] (hence the increased drag) this will result in a theoretical value that is slightly higher than the actual. In Figure 5.3 the triangles relate the long extender and polymer store, the squares relate the short extender with the metal store and the diamonds relate the long extender and the metal store. The circled data point is identified because it does not follow the trend for the short extender and metal store. Additionally, the force coefficient value is exceptionally high, deviating significantly from the theoretical value.

The calculated error present for this set of runs is the highest magnitude in error of all the runs for the entire test indicating an anomaly. Figure 5.4 displays the time vs. voltage plots generated from the oscilloscope for the anomalous data point. In both plots a sharp transition occurs in the data trend. Of all the data runs completed these two are the only ones that indicate the anomaly. Figures 5.5 and 5.6 display the data plots for the long extender with the metal store and long extender with the polymer store at a wind tunnel stagnation pressure setting of 10Psi. Comparing the 10Psi plots among each other reveals the polymer store generates the cleanest plot without the high frequency oscillations. It appears the polymer store receives less excitation from transverse forces and axial buffeting. As discussed in chapter 3, this is due to the lower moment of inertia from the lighter polymer store as compared to the heavier metal store. There are several causes for the deviation of the force coefficients from the theoretical values and the apparent mitigation of higher frequency oscillations by the polymer store. A few causes include a lower base pressure than the estimated supersonic pressure for the store, roughness of the store, mass of the store and composition. Composition deals with added physics not intuitively obvious. Namely it was noticed that when the metal store is attached to either threaded sting it tended to cause resonating vibrations when excited – similar to that observed when striking a tuning fork. Due to the lower mass and less dense material, the polymer store reduced the inertia on the end of the extender and thereby lowered the natural frequency transmitted through the extender and sensed by the load cell.



Metal Store, Short Extender, 10 psi, run 1

Metal Store, Short Extender, 10 psi, run 2

Figure 5.4: Time vs. Voltage Plot, Run 1 and 2 – short extender, metal store, 10psi.

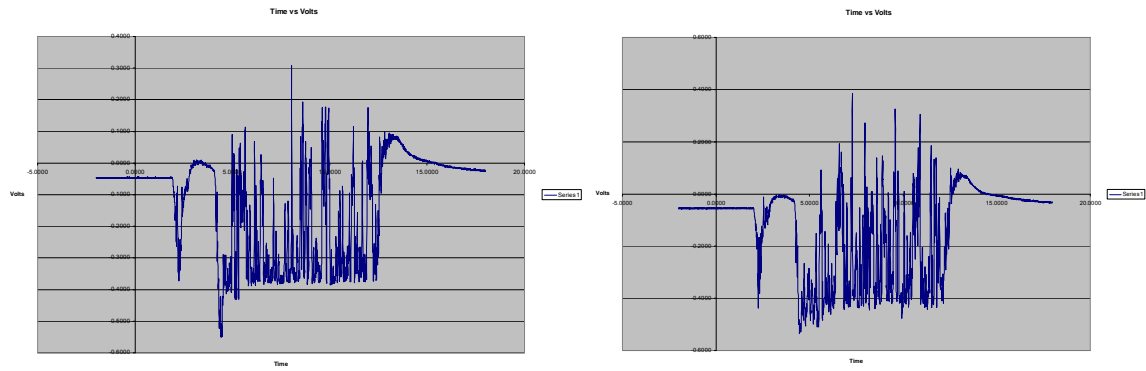


Figure 5.5: Time vs. Voltage Plot, Run 1 and 2 – long extender, metal store, 10psi.

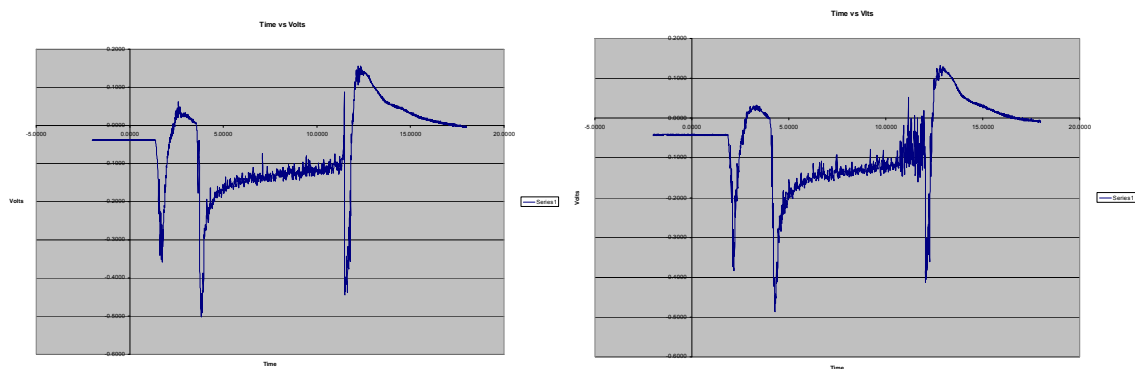


Figure 5.6: Time vs. Voltage Plot, Run 1 and 2 – long extender, poly. store, 10psi.

Figure 5.7 displays the empirical force coefficients for the secondary configuration and Figure 5.8 displays the force coefficients for the tertiary configuration. The error bars represent the relative statistical error between multiple runs at the same

x/D . Between the two plots the largest error is seen in the short extender data series run-1. It is assumed that the short extender and metal store are imparting the greatest stress on the load cell resulting in the wide range of measurements. When comparing these sets of results it is apparent that they significantly differ in magnitude and trend, especially between $x/D = 0.0$ and $x/D = 1.3$. Conclusions from previous experimental and CFD works indicate that the store transitions from negative to positive axial loading between $x/D=0.22$ and $x/D=0.92$ [21, 38, 41]. Recall from chapter 3 that the only difference between the secondary and tertiary configuration is the different length stings. A preliminary conclusion is that the secondary configuration appears to have erroneous data as did the short extender data point seen in the store-only plot. The discrepancy in the data appears to be dependent upon the sting.

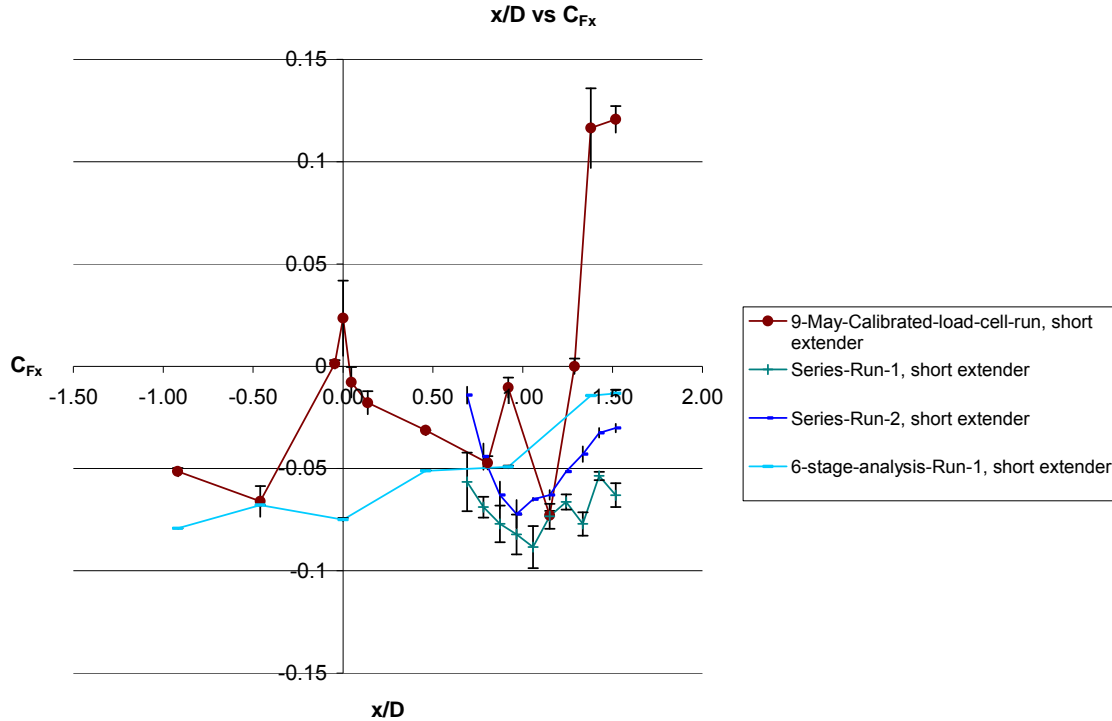


Figure 5.7: Force Coefficients from Secondary Configuration.

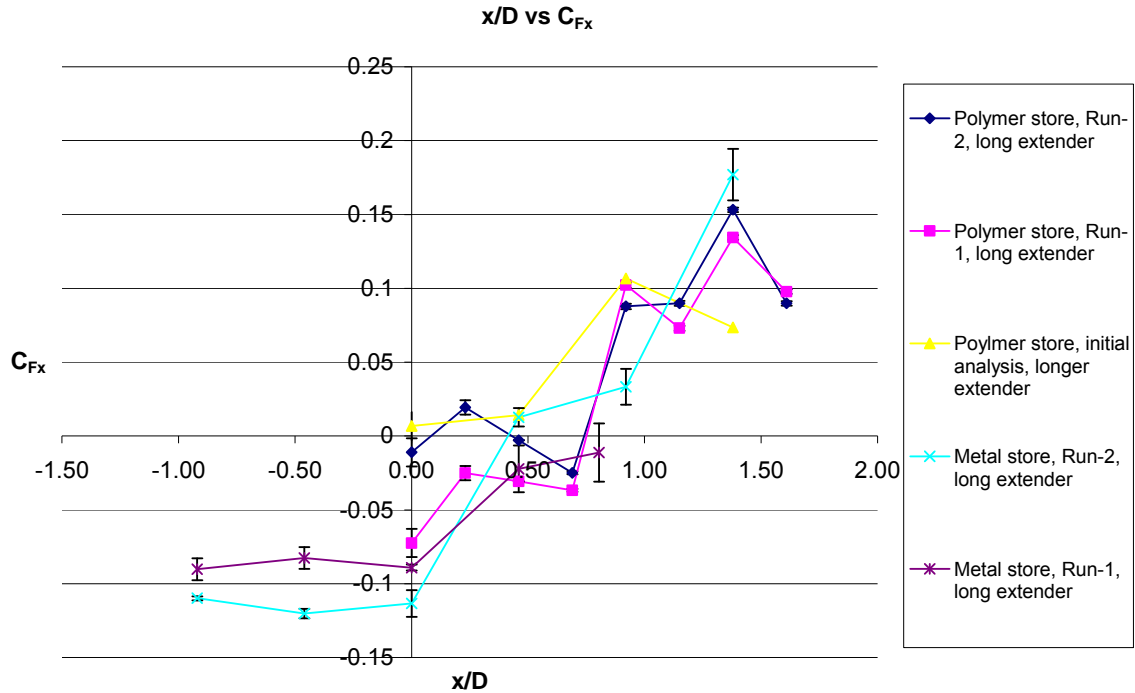


Figure 5.8: Force Coefficients from Tertiary Configuration.

The effects of the sting are dominant in the store's base region since it occupies approximately one-third of the cross-section of the store's base. Furthermore, since lengthening the sting resulted in generating data that seemed to follow the expected trend from previous research, a suitable explanation must address the increase in length. From a 2-dimensional perspective, the area between the store's base, and the nylon coupler and load cell, strongly resemble a cavity. Figure 5.9 shows comparative views and relates them to the dynamics present in a cavity [37, 39]. The load cell and base of the store form an axis-symmetric cavity about the extender and nylon coupler. A 2-dimensional analogy is applied. The length of the exposed region of the short extender and nylon sleeve measures nearly 38 mm and the height of the cavity is dependent on the store's

base which measures nearly 4 mm. Computing L/h yields 9.5 indicating that the 2-dimensional association with a cavity is specifically a closed cavity in which a shear layer traps a rotating flow field inside. As depicted in the small pressure coefficient plot, a positive pressure coefficient is applied in the store's base – the opposite of what is expected from base flow theory. The length of the exposed region of the longer extender measures nearly 60 mm. The L/h value is 15 resulting in the open cavity in which separated flow occurs in the store's base region yielding a negative pressure coefficient on the store's base – much closer to the expected outcome. In the case of the short extender, the back pressure in the base region will result in the store being pushed back towards the cone, even after it has exited the cone's base. This would generate the results seen in the secondary configuration data plot (ref. Figure 5.7). The longer cavity created by the longer extender would result in a low pressure region in the remaining base area of the store better matching the store's base flow if no sting were present. This would accommodate the expected results seen in the tertiary configuration data plot.

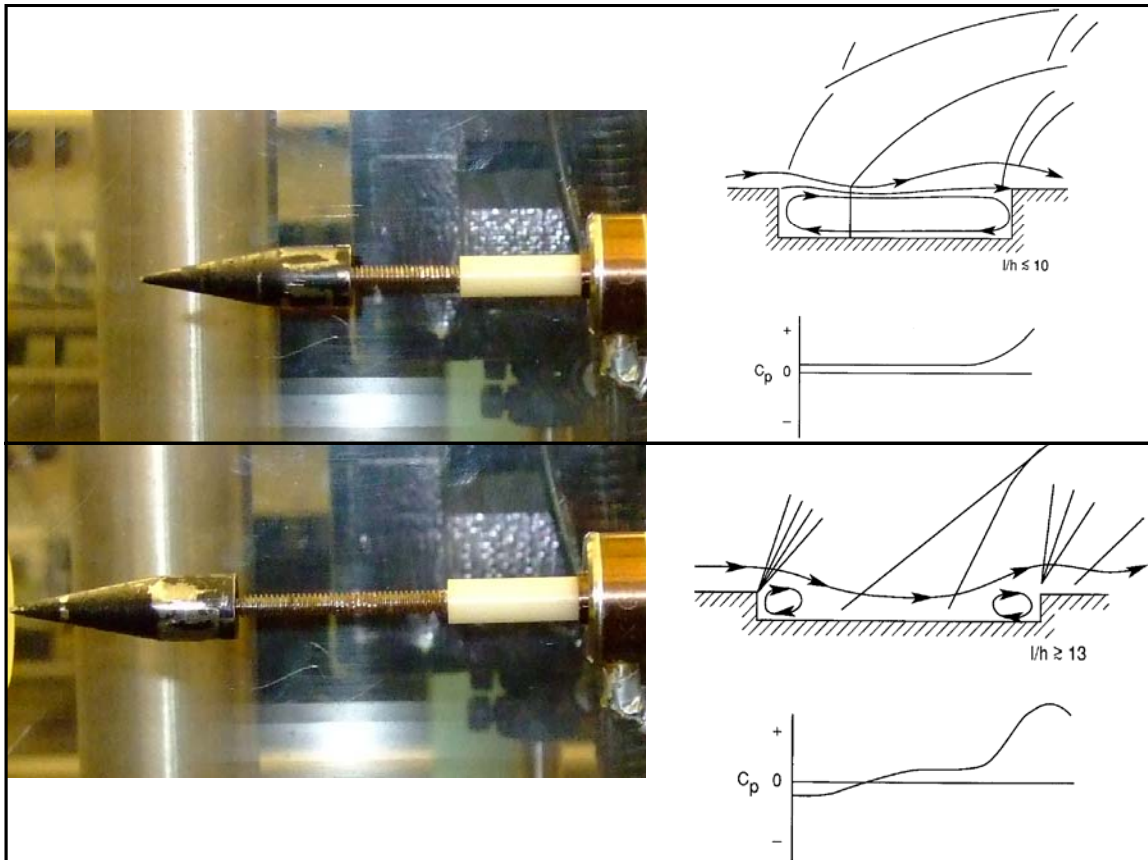


Figure 5.9: Cavity Analogy.

CFD and Experimental Comparison Figure 5.10 displays the CFD predictions with the best results from the experiments in the wind tunnel. The best experimental results include the longer extender. For each data point the coefficient was calculated as discussed previously and then the average coefficient was calculated for the specific x/D position. The error bars represent the relative statistical error between multiple runs at the same x/D for a particular location (x/D) as computed by Equation (3.11). The calculated statistical error for each individual run as calculated by Equation (3.12) is not specifically identified on the plots but ranges between 1 and 3 grams-force per individual run. The error accounts for repeatability variations between multiple runs

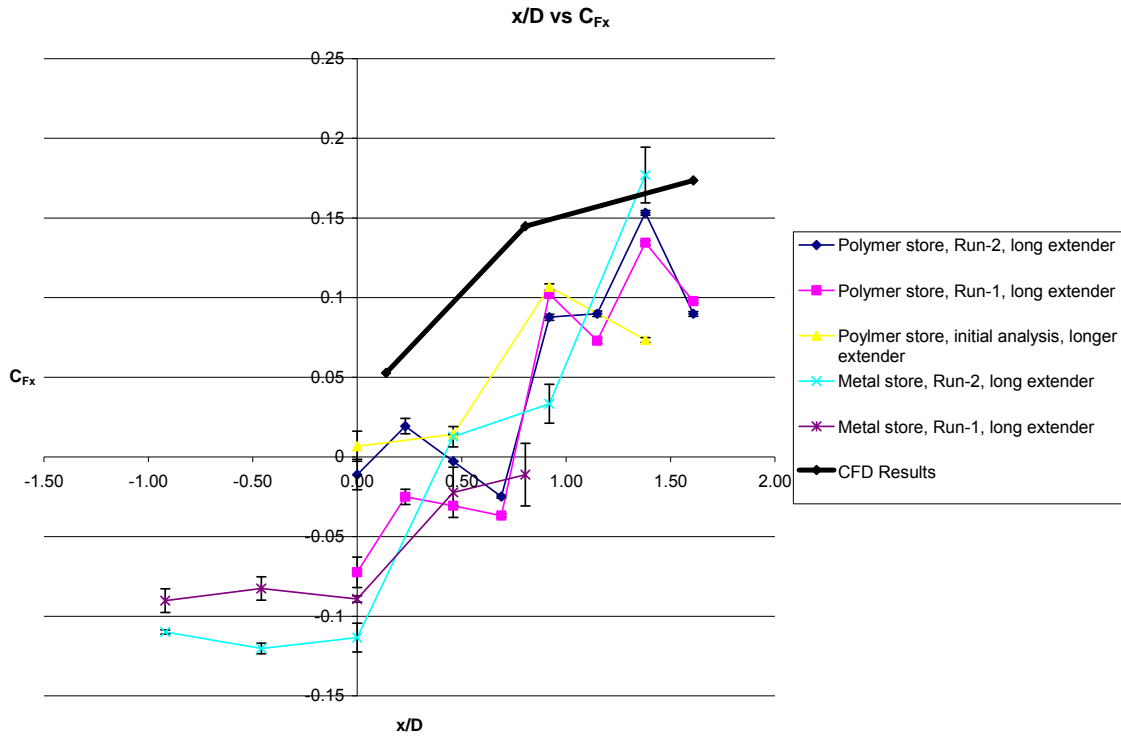


Figure 5.10: CFD versus Experimental Data with Longer Extender.

at a given x/D . These variations in the load cell are a result of store mass, cavity effects ($x/D = 0.0$), axial and transverse buffeting and extender length. In general, the experimental results alone demonstrate that when the tip of the store is inside the cavity of the cone, the store is subjected to a negative axial coefficient of force. Previous researcher has revealed a void of recorded pressure or load data for the store when the store is inside the cavity of the cone. Therefore, standing empirical evidence indicates that when the tip of the store is inside the cone's cavity, negative coefficients of axial force will prevail. This tends to agree with, and strengthen conclusions from many researchers on the presence of a region of reversed flow in the near base region of the store [23, 21, 30, 35, 38].

The experimental data tends to match the trend of the CFD very well while the magnitudes show some variation. Reasons for the variation are the difference in the cone (cavity) and exclusion of the sting effects on the store in the CFD data. It is hypothesized that if the cavity was incorporated into the CFD model and the reduction in base pressure was modeled in the CFD, the values would match very closely. The cavity would have its effect when the tip of the store was near thereby increasing the negative force coefficient on the store in the near base region of the cone. This would shift the experimental points up in magnitude. If the sting was modeled with the CFD, the base pressure of the store would see an increase and an associated decrease in drag would take effect shifting the computational data points down in magnitude.

To better compare the experimental results with CFD predictions figures 5.11 and 5.12 separate out the polymer store and the metal store. Although data is limited on the metal store, very good comparisons can be made between the CFD and the polymer store results. For the polymer store results, comparing the closest experimental data run with the CFD at corresponding stages, the CFD is approximately 25% higher than the experimental for the last two stages.

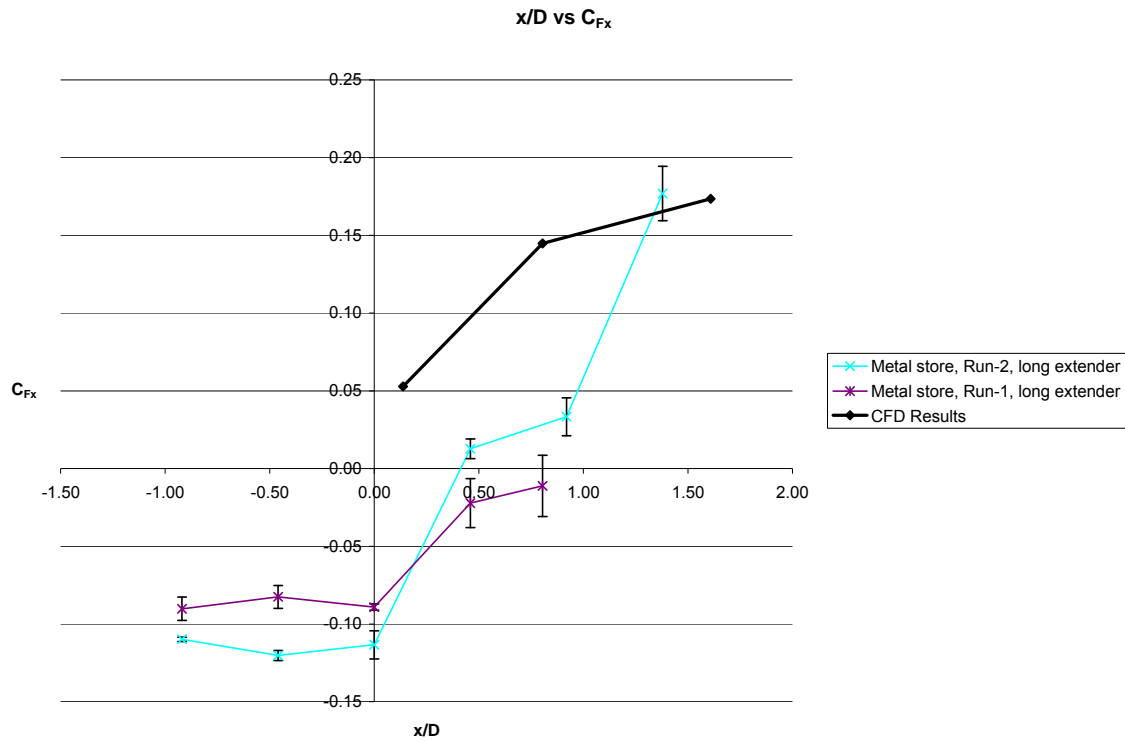


Figure 5.11: CFD versus Metal Store with longer extender.

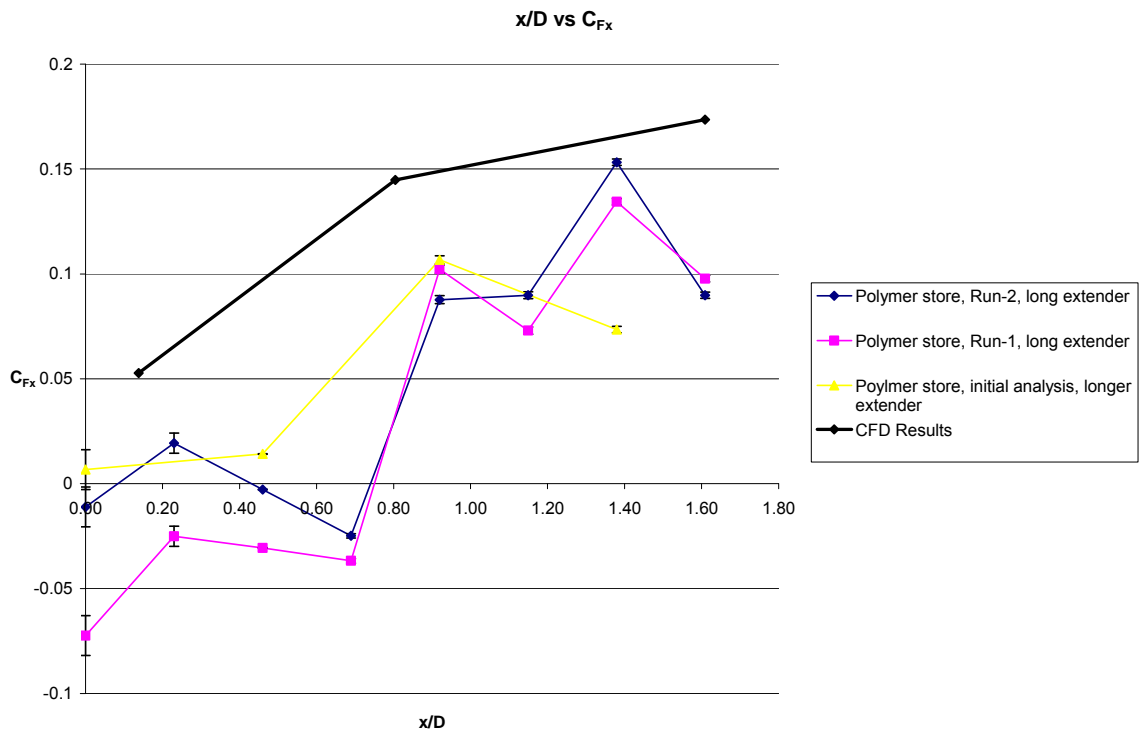


Figure 5.12: CFD versus Polymer Store with longer extender.

Figure 5.13 depicts the combined CFD results with the experimental results. As seen, there tends to be very good correlation between this experimental data set and all of

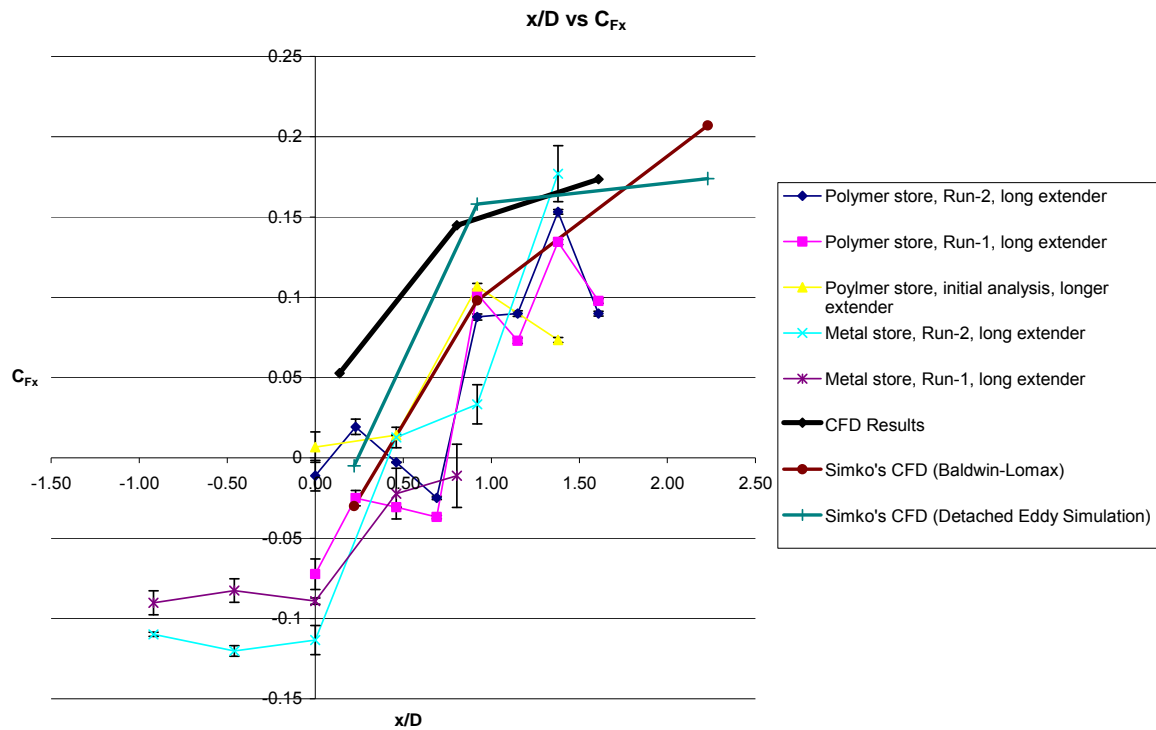


Figure 5.13: CFD predictions and Tertiary Configuration.

the CFD-predicted trends and most of the CFD-predicted coefficients of force. When looking at the transition range ($0.14 < x/D < 0.92$), the experimental data points can be seen bouncing across the various magnitudes predicted by the CFD. Additionally, in this case all transitions occur at or before reaching $x/D = 0.92$. To gain another perspective on the variation in the experimental data, Figure 5.14 depicts the CFD results with the Tertiary configuration except without the connecting trend lines. Since the legend for Figure 5.14 is the same as for Figure 5.13, it has been eliminated from the plot for larger representation. Simko's solid cone CFD models have also been eliminated for more accurate comparison with the experimental set-up. Here it can be seen how well the CFD

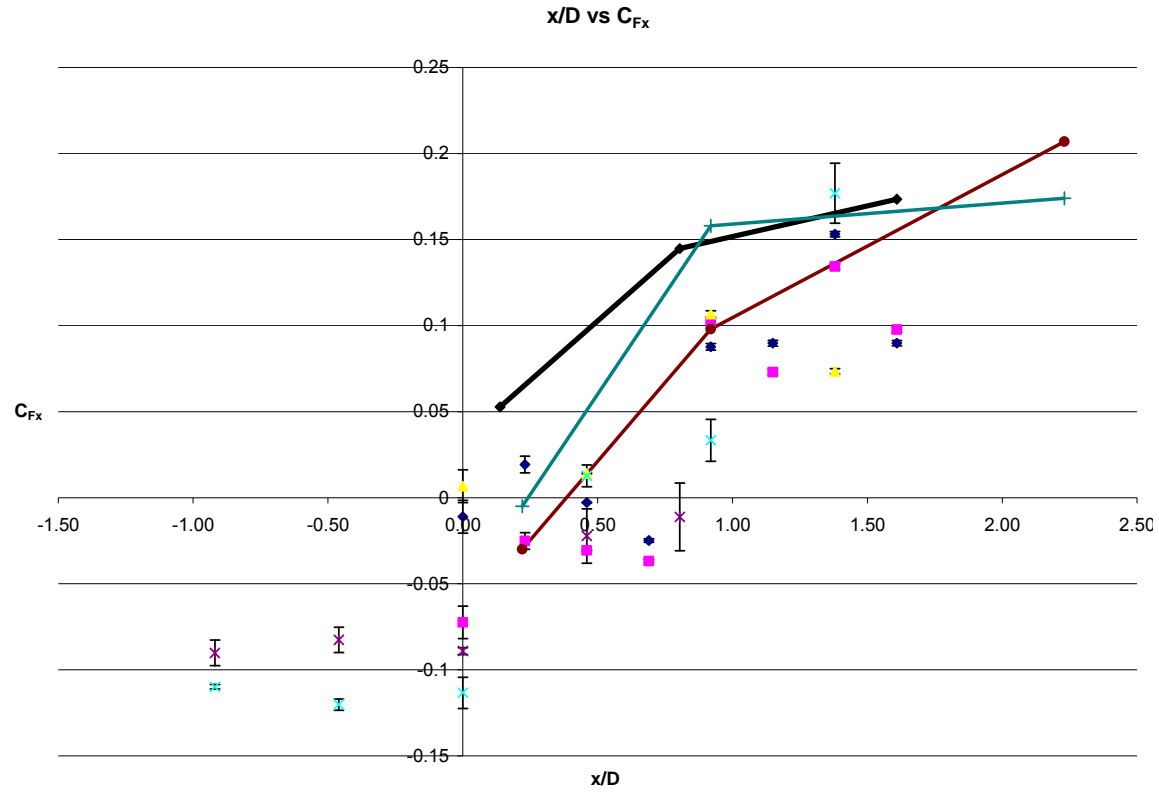


Figure 5.14: Data plot of CFD predictions and Tertiary Configuration.

predictions, especially the k- ϵ model, match with the experimental data given the solid cone used and the steady-state assumption. As identified previously, the greatest discrepancy lies in the near base region at $x/D = 0.14$.

VI. Conclusions and Recommendations

6.1 Chapter Overview

This chapter summarizes the conclusions drawn from the analysis and discussion of the results. Recommendations are provided for near-term and long-term research goals.

6.2 Conclusions

Based on the impending needs of the USAF, an investigation was recently launched to investigate aft dispense of stores at supersonic speeds. The current research encompassed in this document entertained a CFD study followed by an experimental investigation. The CFD was used to generate a model of the experiment prior to conducting the experimental wind tunnel tests. Three objectives were identified to limit and direct the scope of current research.

Prior to conducting the experimental investigation, the CFD study was implemented to meet objectives 1 and 2. The purpose of the CFD was to evaluate the new strut designed to reduce fluctuations in the airflow aft of the cone, and predict the axial loads acting on the store in various locations behind the store. Flow visualizations were successfully generated using *Fluent* 6.2. Multiple cut-planes were generated to observe various dimensions of the flow field. The oblique conical shock was identified and verified. The construct of the cone and store base regions and velocities were identified and analyzed as well as the effects of the strut on the cone and the cone's base region. In comparing the present and previous CFD results on store dispense in the base region, 50% identify a suction force drawing the store back to the cone while the other

50% indicated a neutral or pushing force at x/D less than or equal to 0.22. CFD results demonstrate base flow predictions are governed more by the selection of the turbulence model than the presence or absence of a cavity in the cone. The new strut was found to be superior to the previous strut in several aspects. In 2 of the three stages, the new strut reduced the transverse forces on the store between 2% and 50%. Mach contour visualizations qualitatively demonstrate the new strut improves base flow symmetry considerably in stages 1 and 3. Pressure contour plots on the original strut and cone match previous researchers while pressure contour plots on the new strut display a sharp reduction in turned flow. Cone base pressure plots coincide with previous experimental results and show a distinct improvement in base symmetry in stages 1 and 3 with the new strut. The new strut accounts for a 27% increase in the distance from the cone's base to the stagnation point in stage 3 ($x/D=1.61$), a significant improvement over the original strut. Based on the successful redesign of the strut, the evidence indicates that a thin, sharp-edged strut with symmetrical cross-section and the combination of vertical and shock-wave orientations should produce an optimal underbody strut. Of the two valid experimental data sets, one coincides with present and previous CFD predicted trends. Actual values showed some disagreement due to turbulence modeling, presence of a cavity in the store, and statistical error present in the experimental data. A significant difference in the results of the two experimental data sets has been identified as the extender used to support the store.

Objective 2 and 3 were completed in the experimental portion of research. The experimental investigation consisted of a strut-mounted cone simulating a parent vehicle

and a sting mounted cone-cylinder store located at various positions behind the cone but along its longitudinal axis. The AFIT 2.5"x 2.5" x 12" test section supersonic wind tunnel was used for the entire experimental portion. Within the wind tunnel, the models were subjected to a free stream Mach number of 2.92 where the local velocity reached approximately 615 m/s. Two experimental configurations generated significantly different results based on the length of the extender used. Analysis of the extender and its geometry indicate resemblance of a 2-dimensional axis-symmetric cavity where the extender and the nylon coupler constitute the length and the load cell and base of the store approximate the height. Applying the physics of open and closed cavities indicated that the shorter extender is a poor selection and the longer extender better facilitates the physics of the store's base flow – resulting in more accurate and desirable experimental force coefficients. While theoretical predictions indicate wind tunnel pressure settings have no affect on coefficients of force, actual test runs demonstrate that varying the wind tunnel pressure setting results in varying axial force coefficients. Therefore, when testing it is important to ensure all test runs are completed at the same wind tunnel pressure setting. Analysis of the load cell performance indicates that although the load cell appears to be simpler to mount in a wind tunnel test, the particular brand and model used may not be adequate for collection of accurate axial load data in supersonic conditions. The load cell responded poorly to off-axis loading, a common occurrence in a supersonic wind tunnel environment. The calculated statistical error favored the polymer store with the long extender. Although the error calculations determined non-dimensional error margins, the error of the individual runs indicate that the short extender and metal store

can be assigned approximately a 13% error while the long extender and polymer store are assigned approximately a 6% error. Acquisition and processing of the load cell output data required a non-trivial system to convert the load signal into usable data.

6.3 Recommendations

The present study was successful in identifying and implementing a better strut and obtaining axial force coefficients. However there is still much that can be done to better understand the dynamic environment of aft dispense. The recommended steps are discussed in terms of CFD and Experimental.

Recommendations Regarding CFD A relatively straight-forward task would be to conduct a similar CFD study. However, the recommendation is to implement a different turbulence model. Since there is some debate between $k-\omega$ and $k-\epsilon$ for application to separated flows, a time-accurate $k-\omega$ solution would be beneficial in resolving the use of turbulence models. Based on the experimental results obtained here, it would be worthwhile to incorporate negative x/D evaluations. Since modeling the store tip inside the parent cone has not been done yet, the results would be valuable in providing further visibility. In the experimental results, regardless of the set-up and sting used, whenever the store tip was inside the cavity there was a respectable suction force.

Another recommendation that is perhaps a little more involved is laying the basis for a dynamic simulation. Simko used overset grids and this was also successfully done by Sahu for a time-accurate solution. Sahu used overset chimera grids to study the dynamic transition of a very small store being ejected [41]. Mimicking his study would produce very useful results in the way of dynamic store separation.

A final recommendation for CFD is to generate a more accurate replica of the wind tunnel model. Since the studies contained herein were relatively new, in terms of obtaining axial load data, the several adjustments to the test set-up were not anticipated based on lessons learned from previous studies. It may be worthwhile to perform a few basic experimental runs first to solidify the test procedures and set-up. Once this is complete, modeling the environment surrounding the store (i.e. the extender, load cell and support) will answer a lot of questions that slowed current research down.

Recommendations Regarding Experimental Testing The current study has undoubtedly uncovered a wealth of knowledge and questions regarding supersonic wind tunnel testing. The primary recommendation is to continue wind tunnel testing using the new strut. It has proven superior in many ways to the original swept strut, especially in mitigating turning of the flow, and base flow interference. Using the current geometries, a series of wind tunnel tests should be conducted using different length extender rods equivalent to, or longer than what was used in the tertiary configuration. Obviously a significant alteration to the experimental data obtained was switching out the shorter sting for the longer. All that would be needed is fabrication of the necessary insert threaded couplers. Eight to ten tests conducted at varying x/D with various length and diameter extenders may better pinpoint the nature of the extender-rod sting interference that caused the anomalous data sets presented herein.

A second recommendation is to also take load measurement data using the original swept sting to compare to the new sting. Using Schlieren photographic imaging

and PSP to thoroughly and collectively study the far wake would also be beneficial in rectifying information and data for that area.

A third recommendation is to perform an investigation into alternate ways of developing the data acquisition system. Inclusion of the oscilloscope was initially an unplanned decision but proved to be the most beneficial of all. Reviewing a few catalogs for some good signal processing equipment would be a worthwhile investment for future experiments with the miniature electric load cell. Introducing an alternate method of measuring the axial loads should not be excluded. While the load cell generated accurate trends and reasonable magnitudes, error was introduced. Incorporating a multiple degree-of-freedom balance or a similar load cell from another manufacturer would provide adequate sources of comparative measurements.

A final and more luxurious recommendation is to introduce another parent vehicle. While the cone presents a simple supersonic geometry, a 2-dimensional symmetric cone or “flattened” cone may better match the structure of a supersonic or hypersonic carrier vehicle such as the X-43A [25].

6.4 Summary

In summary, a significant project was undertaken to evaluate a new strut computationally and then generate predictions for a wind tunnel environment. The wind tunnel tests revealed agreement with the CFD however additional issues arose that require further testing to validate. It is the desire of the author to continue to see advancements in the field of aft store release, base flows, and high-velocity weaponry.

APPENDIX

Appendix A: Initial Calculations for the Oblique Conical Shock

Supersonic Cone
Version 1.0.1
Written by: Joseph A. Huwaldt
April 30, 2005

Clear All

M_∞ ☐ Manually Input

θ_c (deg) ☐ Manually Input

θ_s (deg) ☐ Manually Input

$M_\infty > 1$

Shock Wave

M_s

θ_c

θ_s

Semi-Infinite Half-Cone

T_{Tc}/T_c ☐ Manually Input

T_c/T_∞ ☐ Manually Input

M_c ☐ Manually Input

P_{Tc}/P_c ☐ Manually Input

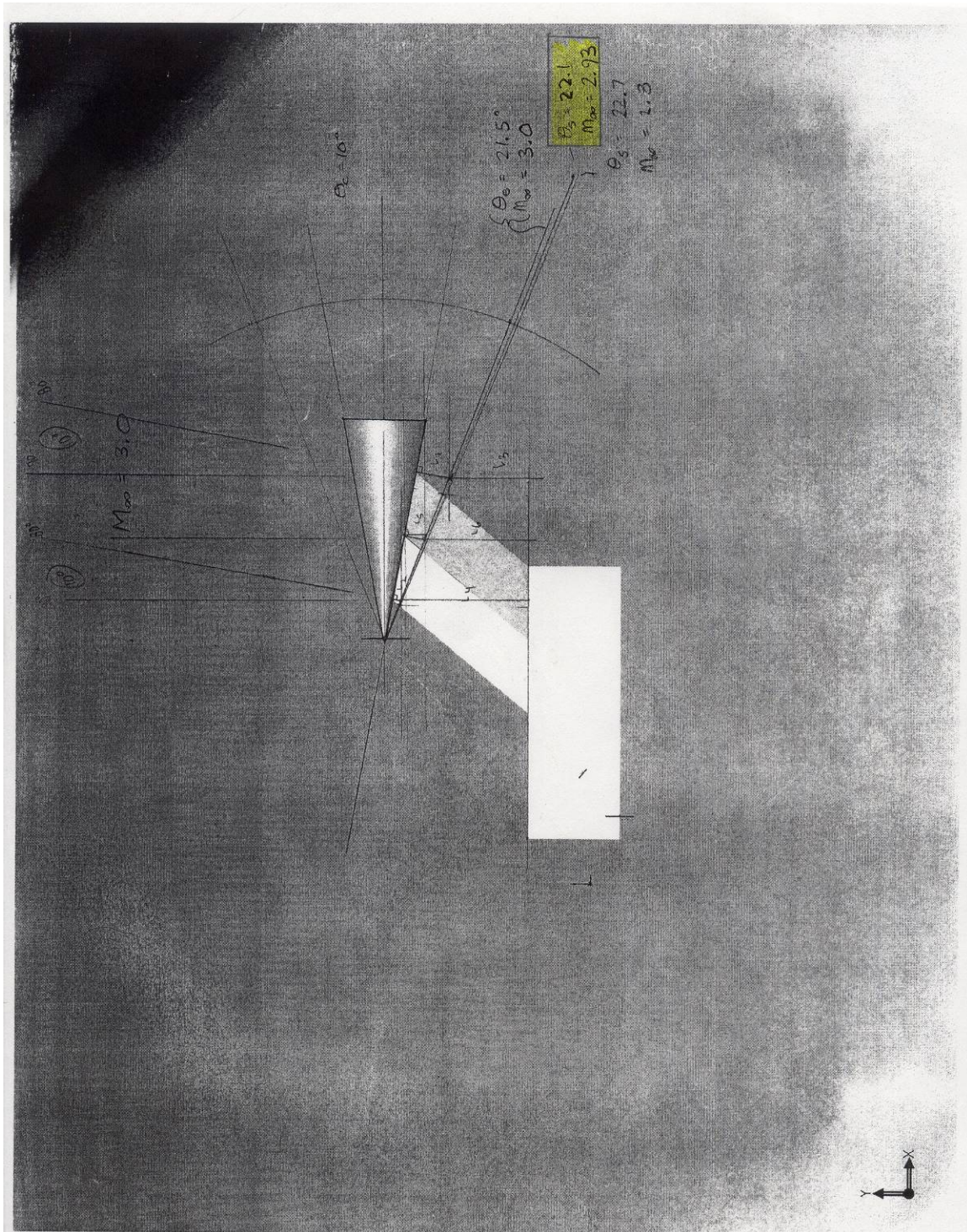
P_c/P_∞ ☐ Manually Input

P_{Tc}/P_c ☐ Manually Input

P_c/P_∞ ☐ Manually Input

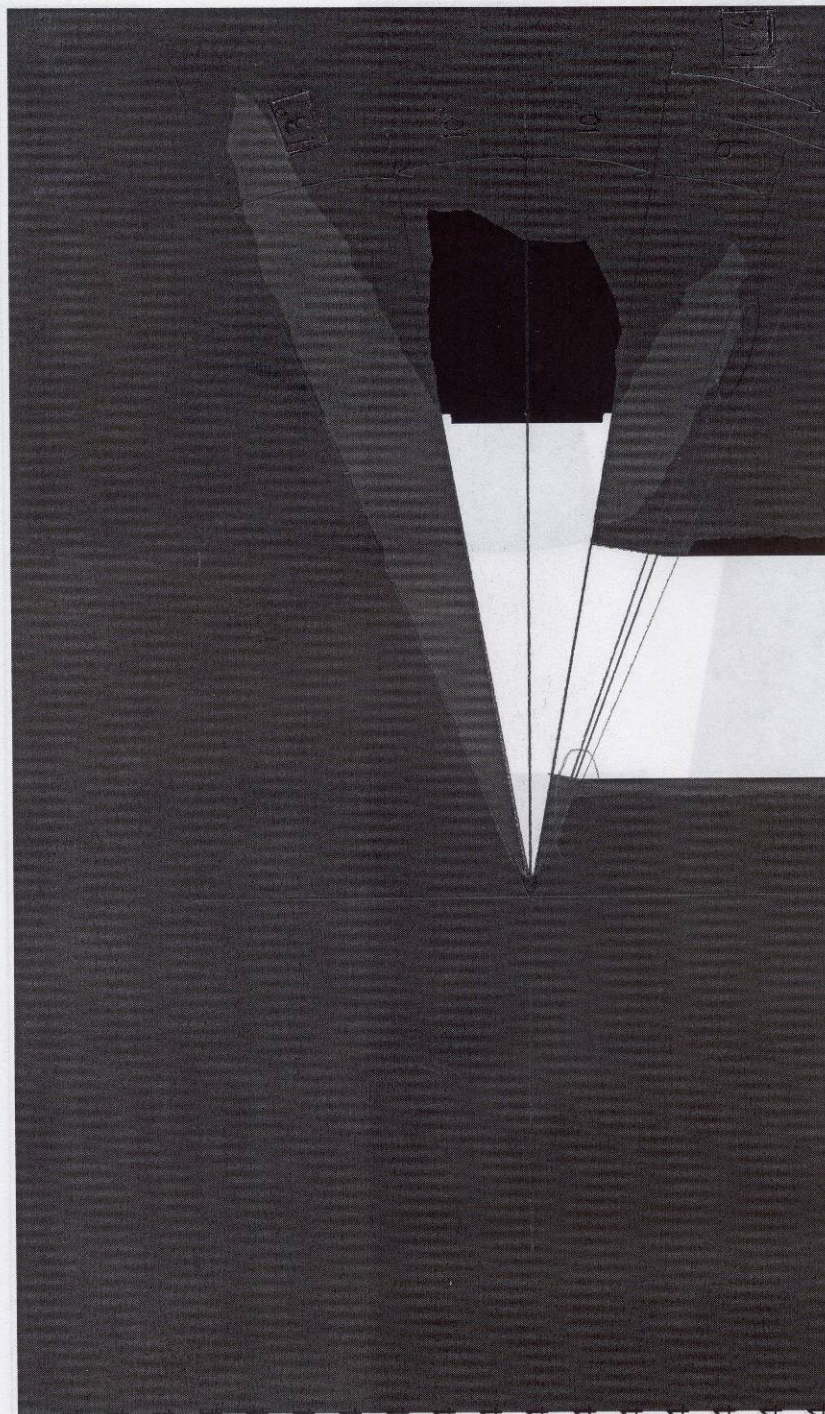
P_{Tc}/P_c ☐ Manually Input

P_c/P_∞ ☐ Manually Input



7.15e+04
6.79e+04
6.44e+04
6.08e+04
5.72e+04
5.36e+04
5.01e+04
4.65e+04
4.29e+04
3.94e+04
3.58e+04
3.22e+04
2.86e+04
2.51e+04
2.15e+04
1.79e+04
1.44e+04
1.08e+04
7.22e+03
3.64e+03
7.21e+01

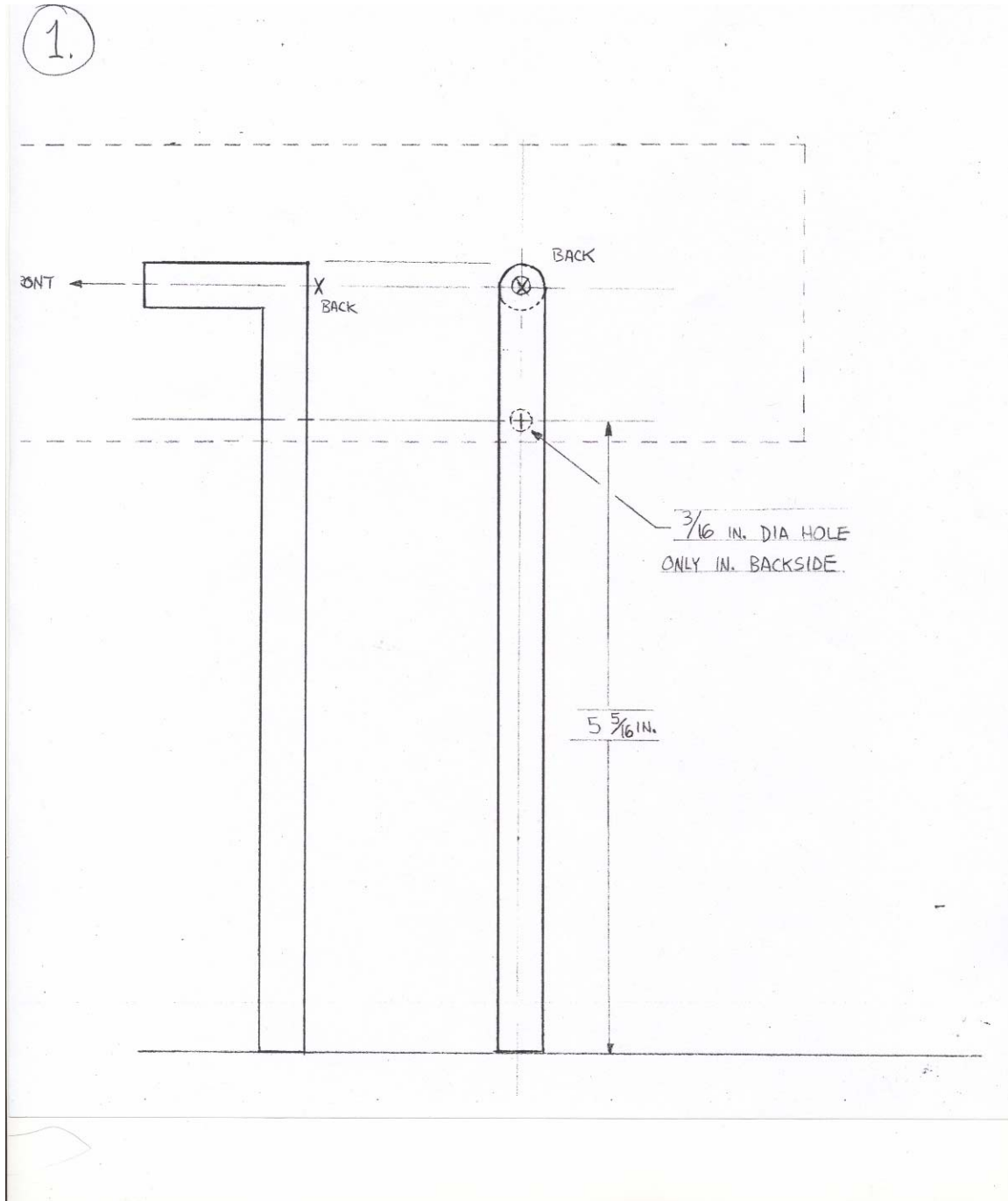
Y
Z—X



Top = $23^\circ \Rightarrow 23.0^\circ$
Bottom $\approx 20.6 \Rightarrow 21.0^\circ$
AVERAGE ANGLE $\Rightarrow 22.0^\circ$

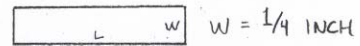
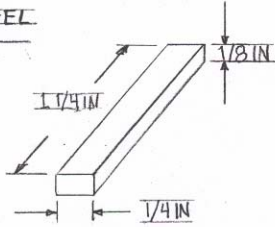
13.50

Appendix B: Experimental Modification, Drawings for Brace Attachment



ASSEMBLY PARTS

2 PARTS, STEEL
BRACES

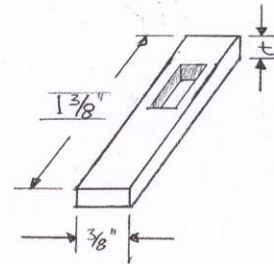
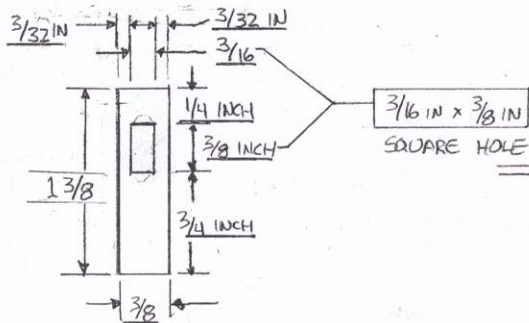


$$W = \frac{1}{4} \text{ INCH}$$

$$L = 1 \frac{1}{2} \text{ INCH}$$

$$t = \frac{1}{8} \text{ INCH}$$

1 PART, STEEL



$$t = \frac{1}{8} \text{ INCH}$$

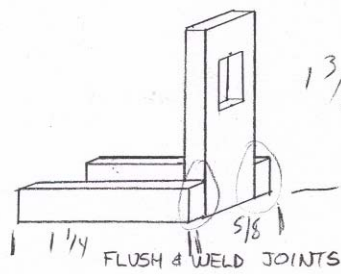
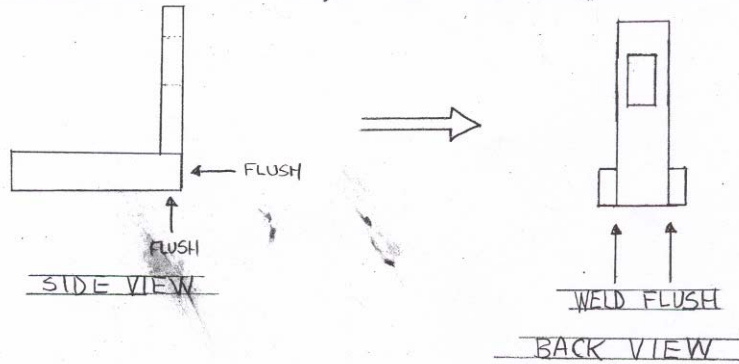
$$W = \frac{3}{8} \text{ INCH}$$

$$L = 1 \frac{3}{8} \text{ INCH}$$

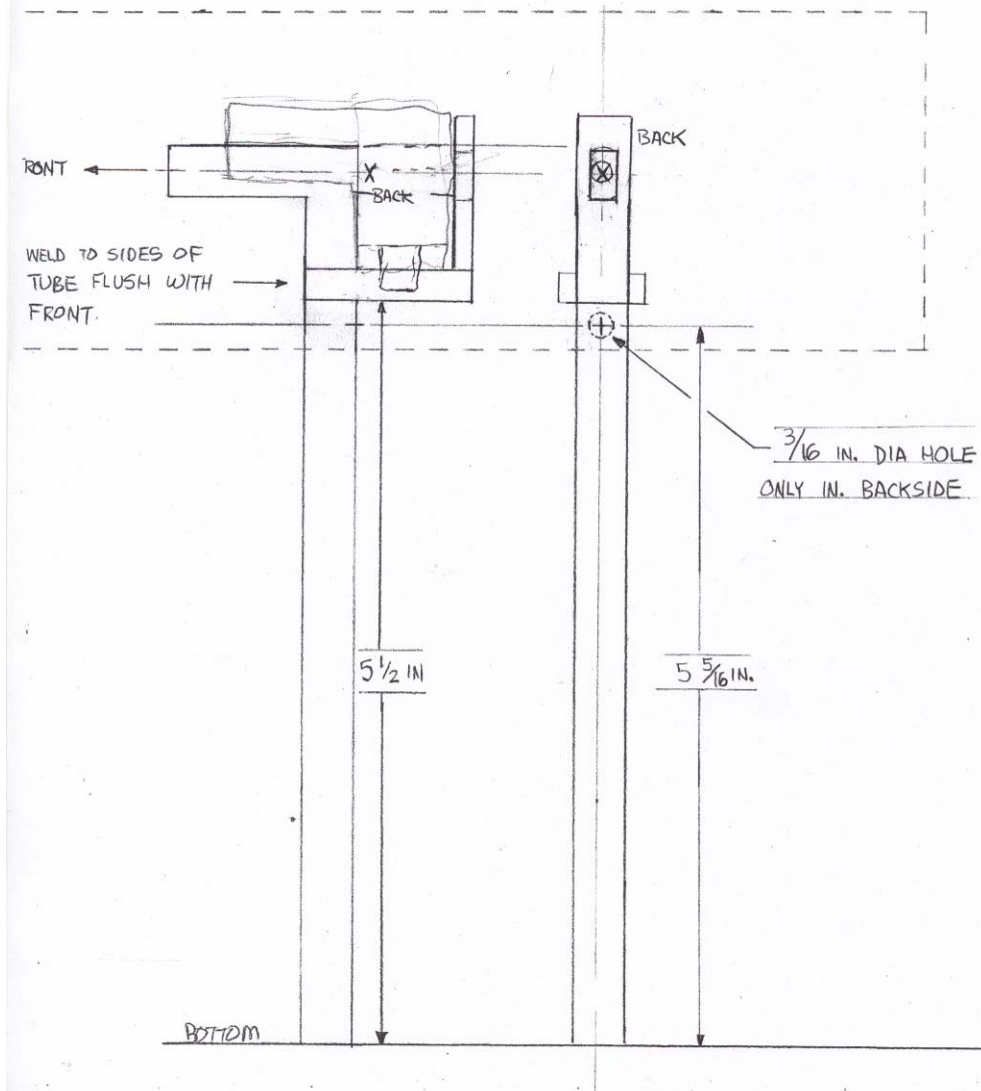
$$t = \frac{1}{8} \text{ INCH}$$

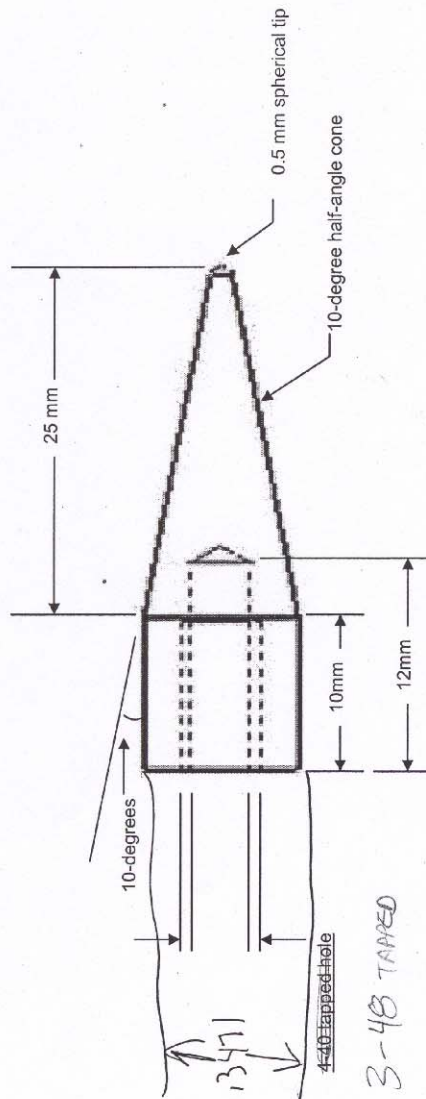
ASSEMBLY DRAWING 1

WELD THE 2 BRACES TO BACK PLATE, FLUSH ON SIDES AND BOTTOMS



ASSEMBLY DRAWING 2





Tolerance (+-) :

0.1mm or .005 inch

Drawing: Alpha-1

Capt Matt Burkinshaw
AFIT/ENY

Appendix C: Load Cell Specification and Calibration Documents

www.honeywell.com/sensing

Honeywell
Sensotec Sensors

1-888-282-9891

www.sensotec.com


Precision Miniature Load Cells

Model 31 and 34


WELDED STAINLESS

RUGGED, SMALL SIZE

TENSION/COMPRESSION



Model 31
(Tension/Compression)



Model 34
(Tension/Compression)

Models 31 and 34, Precision Miniature load cells measure both tension and compression load forces of 50 grams to 10,000 lb. These models are our highest accuracy, rugged miniature load cells. Model 31's welded, stainless steel construction is designed to eliminate or reduce to a minimum, the effects of off-axis loads. (The internal construction assures excellent long term stability for ranges 1000 grams and above.) A modification permits this model to be completely welded for underwater applications. The Model 31 tension/compression load cell has male threads while the Model 34 tension/compression load cell has female threaded load attachments. High accuracies of 0.15-0.25% full scale are achieved. Each bonded strain gage unit is built of welded 17-4 PH stainless steel for additional ruggedness. All load cells that have ranges 10 lb. have a small electrical zero balance circuit board which is in the lead wire (approximately 1"x .087" thick). This balance board does not have to be the same temperature as the transducer. Applications include cable tension and electromechanical parts testing.

AL311 AR

Dimensions (inches)

Model 31 (Order Code AL311)

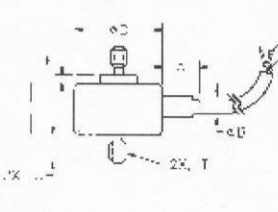
Available Ranges*	T Thread	D"	H"	C"	F"	A"	B"
50; 150; 250 500; g.	#6-32 UNC	1.00	0.75	0.25	0.11	0.50	0.38
1,000 g.; 5; 10 lb.	#6-32 UNC	0.75	0.45	0.25	0.05	0.31	0.19
25; 50; 100 lb.	#10-32 UNF	1.00	0.52	0.25	0.03	0.50	0.25
250; 500; 1,000 lb.	1/4-28 UNF	1.00	0.52	0.38	0.03	0.50	0.25
2,000; 3,000 lb.	3/8-24 UNF	1.00	0.72	0.50	0.03	0.50	0.38
4,000; 5,000 lb.	1/2-20 UNF	1.25	0.94	0.63	0.03	0.50	0.38
7,500; 10,000 lb.	3/4-16 UNF	1.38	1.10	0.88	0.03	0.50	0.38

* Stocked ranges are in bold face print.

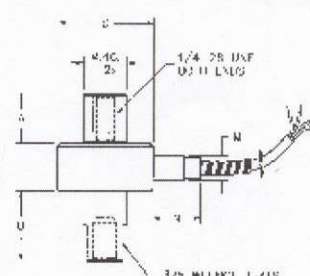
Notes: Model 31 load cells ≤250 grams have overload stops. For custom cells without overload stops consult SENSOTEC.

Model 34 (Order Code AL312)

Available Ranges	D"	H"	A"	B"	M"	N"
50; 150; 250; 500 g.	1.00	1.75	0.52	0.52	0.38	0.50
1,000 g.; 5; 10 lb.	0.75	1.75	0.60	0.72	0.19	0.31
25; 50; 100 lb.	1.00	1.75	0.52	0.72	0.25	0.50
250; 500; 1,000 lb.	1.00	2.00	0.75	0.75	0.25	0.50



Model 31 Male Threads
(Tension/Compression)



Model 34 Female Threads
(Tension/Compression)

3-48 FEMALE INSERT

137

1-888-282-9891

Options (See Appendix)

Temperature compensated 1b, 1c, 1f; Special calibration 30a, 30b

Premium Options: 1d, 1e, 1g, 1h (<=25 lb.), 1i; 6d; 9a (<=5 lb.)

Accessories: Rod end attachments for Model 31

	Model 31 (Male Threads) (Tension/Compression) Order Code AL311	Model 34 (Female Threads) (Tension/Compression) Order Code AL312
PERFORMANCE		
Load Ranges.....	50 g to 10,000 lb.	50 g to 1,000 lb.
Non-Linearity/Hysteresis (max)		
50 to 1,000 g.....	±0.15% F.S.	±0.15% F.S.
5 to 250 lb.....	±0.15% F.S.	±0.15% F.S.
500 to 10,000 lb.....	±0.2% F.S.	±0.2% F.S.
Non-Repeatability (max)		
50 to 1,000 g.....	±0.1% F.S.	±0.1% F.S.
5 to 10,000 lb.....	±0.05% F.S.	±0.05% F.S.
Output (standard)		
50 to 150 g (semi).....	0.1mV/V/g max	0.1mV/V/g
250 to 500 g (semi).....	20mV/V	20mV/V
1,000 g.....	1.5mV/V (nominal)	1.5mV/V (nom)
5 lb. to 10,000 lb. (foil).....	2mV/V	2mV/V
Resolution.....	Infinite	Infinite
ENVIRONMENTAL		
Temperature, Operating.....	-65° F to 250° F	-65° F to 250° F
Temperature, Compensated.....	60° F to 160° F	60° F to 160° F
Temperature Effect		
-Zero/Span (max)		
50 to 500 g.....	0.015% F.S./° F	0.015% F.S./° F
1,000 g.....	0.005% F.S./° F	0.005% F.S./° F
5 to 10,000 lb.....	0.005% F.S./° F	0.005% F.S./° F
ELECTRICAL		
Strain Gage Type.....	Foil or Semiconductor	Foil or Semiconductor
Excitation (Calibration)		
50 g to 10 lb.....	5.00VDC	5.00VDC
20 lb. to 10,000 lb.....	10.0VDC	10.0VDC
Insulation Resistance.....	5000 megohm @ 50VDC	5000 megohm @ 50VDC
Bridge Resistance		
50 to 500 g.....	500 ohms (semi)	500 ohms (semi)
1,000 gms.....	350 ohms (foil)	350 ohms (foil)
5 to 10,000 lb.....	350 ohms (foil)	350 ohms (foil)
Shunt Calibration Data.....	Included	Included
Wiring Code (std).....	#1 (See Pg. AP-8)	#1 (See Pg. AP-8)
Electrical Termination (std).....	Teflon cable (5 ft.)	Teflon cable (5 ft.)
MECHANICAL		
Overload, Safe.....	50% over capacity	50% over capacity
Thread Size.....	See table	See table
Deflection -Full Scale.....	0.0005"-0.0020"	0.0005"-0.0020"
Casing material.....	17-4 PH Stainless	17-4 PH Stainless
Weight (nom).....	1.6 oz.	2.5 oz.
IN-LINE AMPLIFIERS (Optional)		
Outputs Available.....	±5VDC, 4-20mA	±5VDC, 4-20mA

NOTES *Standard calibration for tension/compression load cells is in tension only.

General Information

How to order (See Pg. AP-19)

Load cell selection flow chart (See Pg. LO-1)

Installation Note: Maximum torque for installation of Model 31 in ranges less than 25 lb. is 12 lb.-in.

LOAD
MINIATURE

LO-19

Honeywell

Honeywell

Sensotec Sensors

2080 Arlingate Lane

Columbus, Ohio 43228 U.S.A.

Phone: 614-850-5000

Fax: 614-850-1111

URL: <http://www.sensotec.com>

E-mail: service@sensotec.com

Certificate of Calibration

Product Identification

Product Type: Load Cell

Serial Number: 1104026

Model: 31

Part Number: 060-1426-02

Order Code: AL311AR

Product Specifications

Full Scale Range: 1000 grams

Calibrated At: 1000 grams

Tension

$$1g = 0.005 \text{ VDC} = 5 \text{ mV}$$

Excitation: 5 VDC

Input Impedance: 355 Ω

Output Impedance: 354 Ω

Electrical Leakage: ∞ Meg Ω

Calibration Data

Calibration Factor: 1.0358 mV/VDC

Shunt Cal Factor: 0.4424 mV/V

Shunt Cal Resistor: 200k Ω

Wiring Code

UNAMP#1,4-COND,CBL

COLOR	DESIGNATION
RED	(+)EXCITATION
BLACK	(-)EXCITATION
GREEN	(-)OUTPUT
WHITE	(+)OUTPUT

001-0333-01

Certification Information

Type of Calibration: Standard

Calibration Date: 03/22/2006

Certificate Number: 086-0000-00

Calibration Procedure: 072-LC75-10

Notes: Instruments used in the calibration of this product have been calibrated to standards traceable to the National Institute of Standards and Technology (NIST). A calibration uncertainty ratio of 4:1 has been maintained unless otherwise stated.

If you have any questions concerning this certificate of calibration, or for recalibration or repair of this product, please visit our website at <http://www.sensotec.com/service.htm> or call our service department at (614) 850-5000.

This is a quality record.

Approved and Certified By:

Ester Gozon

Ester Gozon, Quality Manager

Printed: 7/18/2006

Page 1 of 1

SENSOTEC

MODEL 31 LOAD CELL INSTALLATION INSTRUCTIONS

The Model 31 load cell with a low range capacity requires some care in handling and installation to avoid permanent damage to the load cell.

1. The Model 31 load cell is shipped with the active threaded stud removed. The active threaded stud has threads on both ends and should be finger tightened into the load cell body.
2. The threaded stud on the base of the load cell is machined as an integral part of the load cell. The base can be threaded into the customer's part by grasping the main body of the load cell, rotating load cell and cable assembly until finger-tight.
3. Caution should be used when attaching the active threaded stud to the customer's fixture. The customer's fixture should not be threaded below the shoulder at the bottom of the active threaded stud. The customer's fixture should not be tightened more than 12 in.-lbs. which is about finger-tight. No wrenches should be used in assembling these parts.

4. The tension or compression force to be measured must be applied as much as possible in a vertical direction along the center line of the mounting studs.

50%

MAL ≈ 150%

5. Bending moment or torsion forces in excess of 12 in.-lbs. could cause permanent damage to the load cell. DECREASED ACCURACY

The Model 31 load cell is available with optional mechanical overload stops for both tension and compression. The mechanical stops will usually protect the load cell from forces in the tension and compression direction, however, the load cell may be damaged by either a bending moment or excessive torque during installation. The optional mechanical overload stops will not protect the cell from bending moments due to excessive torque of the threads. The most obvious result of damage to the load cell is the residual unbalance of the strain gage bridge. The strain gage bridge is balanced at the factory to within two percent of the full rated output in millivolts. The addition of the customer's fixture will change the zero balance depending upon the weight of the fixture. Excessive unbalance can be attributed to damage resulting from excess torque or bending moment.

The Model 31 load cell has two welded stainless steel diaphragms on the top and bottom side of the active element to protect the load cell from the effects of off axis loading. For example, a 100% full scale load applied at 90 degrees to the base of the active stud would create a maximum error of only 1.5%. A 100% full scale bending moment load applied at 90 degrees to the vertical axis of the load cell and two inches above the surface of the load cell would create a maximum error of only 2.50%.

7/00: 003-0048-00

Appendix D: Calculation Spreadsheets

Series-4, Saturday 19 May: Long extender tests

Metal Store

Constants:

Mach 2.92
 T 110 K
 R 287.05 J/kg*K
 V 614 m/s
 A_{ref} 6.63E-05 m²
 D 21.75 mm

Dist. (mm)	Load Cell Load (g)	Free- stream Load (g)	Load (N)	Test Section Press. (psig)	Test Section Press. (Pa)	Density (kg/m ³)	C_{Dx}	x/D	Average C_{Dx}	Metal Store, Run-1 Error	Metal Store, Run-1 Error %
-20	30	-30	-0.2942	1.27	8758.62	0.2774	-0.0849	-0.92	-0.0902	0.0075	8.2863
-20	34	-34	-0.3334	1.28	8827.59	0.2796	-0.0955	-0.46	-0.0826	0.0073	8.8885
-10	32	-32	-0.3138	1.31	9034.48	0.2861	-0.0878	0	-0.0891	0.002	2.2448
-10	28	-28	-0.2746	1.3	8965.52	0.2839	-0.0774	0.46	-0.0222	0.0158	71.119
0	31	-31	-0.3040	1.27	8758.62	0.2774	-0.0877	0.805	-0.0112	0.0197	176.47
0	32	-32	-0.3138	1.27	8758.62	0.2774	-0.0905				
10	12	-12	-0.1177	1.29	8896.55	0.2818	-0.0334				
10	4	-4	-0.0392	1.3	8965.52	0.2839	-0.0111				
17.5	9	-9	-0.0883	1.29	8896.55	0.2818	-0.0251				
17.5	-1	1	0.0098	1.3	8965.52	0.2839	0.0028				

Dist. (mm)	Load Cell Error Load (g)	Free- stream Load (g)	Load (N)	Test Section Press. (psig)	Test Section Press. (Pa)	Density (kg/m ³)	C_{Dx}	x/D	Metal Store, Run-1 Sample Error %
-20	3.94140	3.94140	0.0387	1.27	8758.62	0.2774	0.0112	-0.92	13.1380
-20	3.87941	3.87941	0.0380	1.28	8827.59	0.2796	0.0109	-0.92	11.4100
-10	3.56208	3.56208	0.0349	1.31	9034.48	0.2861	0.0098	-0.46	11.1315
-10	3.72521	3.72521	0.0365	1.3	8965.52	0.2839	0.0103	-0.46	13.3043
0	2.94579	2.94579	0.0289	1.27	8758.62	0.2774	0.0083	0	9.5025
0	3.13650	3.13650	0.0308	1.27	8758.62	0.2774	0.0089	0	9.8016
10	3.81312	3.81312	0.0374	1.29	8896.55	0.2818	0.0106	0.46	31.7760
10	3.12535	3.12535	0.0306	1.3	8965.52	0.2839	0.0086	0.46	78.1337
17.5	3.94332	3.94332	0.0387	1.29	8896.55	0.2818	0.0110	0.805	43.8147
17.5	3.38163	3.38163	0.0332	1.3	8965.52	0.2839	0.0093	0.805	338.1627

Metal Store, Run-1

Series-4, Saturday 19 May: Long extender tests

Metal Store

Constants:

Mach 2.92
T 110 K
R 287.05 J/kg*K
V 614 m/s
A_{ref} 6.63E-05 m⁴
D 21.75 mm

Dist. (mm)	Load Cell Load (g)	Free- stream Load (g)	Load (N)	Test Section Press. (psig)	Test Section Press. (Pa)	Density (kg/m ³)	C _{Dx}	x/D	Average C _{Dx}	Metal Store, Run-2 Error	Metal Store, Run-2 Error %
-20	40	-40	-0.3923	1.32	9103.45	0.2883	-0.1089	-0.92	-0.10985	0.0013	1.2267
-20	37	-37	-0.3628	1.20	8275.86	0.2621	-0.1108	-0.46	-0.12023	0.0032	2.6766
-10	43	-43	-0.4217	1.31	9034.48	0.2861	-0.1180	0.00	-0.11338	0.0091	7.9835
-10	45	-45	-0.4413	1.32	9103.45	0.2883	-0.1225	0.46	0.01269	0.0063	49.727
0	39	-39	-0.3825	1.31	9034.48	0.2861	-0.1070	0.92	0.03332	0.0122	36.561
0	44	-44	-0.4315	1.32	9103.45	0.2883	-0.1198	1.38	0.17693	0.0175	9.8666
10	-6	6	0.0588	1.32	9103.45	0.2883	0.0163				
10	-2	2	0.0196	1.33	9172.41	0.2905	0.0054				
10	-6	6	0.0588	1.32	9103.45	0.2883	0.0163				
20	-17	17	0.1667	1.33	9172.41	0.2905	0.0459				
20	-8	8	0.0785	1.33	9172.41	0.2905	0.0216				
20	-12	12	0.1177	1.33	9172.41	0.2905	0.0324				
30	-69	69	0.6767	1.31	9034.48	0.2861	0.1893				
30	-60	60	0.5884	1.31	9034.48	0.2861	0.1646				

Dist. (mm)	Load Cell Error Load (g)	Free- stream Load (g)	Load (N)	Test Section Press. (psig)	Test Section Press. (Pa)	Density (kg/m ³)	C _{Dx}	x/D	Metal Store, Run-2 Sample Error %
-20	0.75829	0.75829	0.0074	1.32	9103.45	0.2883	0.0021	-0.92	1.895717
-20	1.16644	1.16644	0.0114	1.20	8275.86	0.2621	0.0035	-0.92	3.152546
-10	1.25020	1.25020	0.0123	1.31	9034.48	0.2861	0.0034	-0.46	2.907448
-10	1.63663	1.63663	0.0160	1.32	9103.45	0.2883	0.0045	-0.46	3.636954
0	1.36668	1.36668	0.0134	1.31	9034.48	0.2861	0.0037	0.00	3.504299
0	1.70298	1.70298	0.0167	1.32	9103.45	0.2883	0.0046	0.00	3.870405
10	1.48930	1.48930	0.0146	1.32	9103.45	0.2883	0.0041	0.46	24.82162
10	1.77563	1.77563	0.0174	1.33	9172.41	0.2905	0.0048	0.46	88.78158
10	1.29754	1.29754	0.0127	1.32	9103.45	0.2883	0.0035	0.46	21.6257
20	1.78081	1.78081	0.0175	1.33	9172.41	0.2905	0.0048	0.92	10.47536
20	1.28479	1.28479	0.0126	1.33	9172.41	0.2905	0.0035	0.92	16.05992
20	1.18365	1.18365	0.0116	1.33	9172.41	0.2905	0.0032	0.92	9.863712
30	1.06114	1.06114	0.0104	1.31	9034.48	0.2861	0.0029	1.38	1.537888
30	0.85659	0.85659	0.0084	1.31	9034.48	0.2861	0.0023	1.38	1.427645

Metal Store, Run-2

Polymer Store

RUN 1

Constants:

Mach 2.92

T 110 K

R 287.05 J/kg*K

V 614 m/s

A_{ref} 6.63E-05 m²

D 21.75 mm

Dist. (mm)	Load Cell Load (g)	Free- stream Load (g)	Load (N)	Test Section Press. (psig)	Test Section Press. (Pa)	Density (kg/m ³)	C _{Dx}	x/D	Average C _{Dx}	Polymer Store, Initial Run Error	Polymer Store, Initial Run Error %
0	-5	5	0.0490	1.34	9241.38	0.29268	0.01341	0.00	0.00617	0.01023	165.818
0	0.4	-0.4	-0.0039	1.35	9310.34	0.29486	-0.0011	0.46	0.01415	0.00016	1.11355
10	-5	5	0.0490	1.26	8689.66	0.2752	0.01426	0.92	0.10672	0.00191	1.79014
10	-5	5	0.0490	1.28	8827.59	0.27957	0.01404	1.38	0.07347	0.0015	2.04571
20	-40	40	0.3923	1.33	9172.41	0.29049	0.10807				
20	-39	39	0.3825	1.33	9172.41	0.29049	0.10537				
30	-27	27	0.2648	1.34	9241.38	0.29268	0.07241				
30	-28	28	0.2746	1.35	9310.34	0.29486	0.07453				

Dist. (mm)	Load Cell Error Load (g)	Free- stream Load (g)	Load (N)	Test Section Press. (psig)	Test Section Press. (Pa)	Density (kg/m ³)	C _{Dx}	x/D	Polymer Store, Initial Run Sample Error %
0	0.74722	0.74722	0.0073	1.34	9241.38	0.29268	0.002	0.00	14.9444
0	0.82239	0.82239	0.0081	1.35	9310.34	0.29486	0.00219	0.00	205.597
10	0.62300	0.62300	0.0061	1.26	8689.66	0.2752	0.00178	0.46	12.4601
10	0.78061	0.78061	0.0077	1.28	8827.59	0.27957	0.00219	0.46	15.6122
20	0.90968	0.90968	0.0089	1.33	9172.41	0.29049	0.00246	0.92	2.2742
20	0.99345	0.99345	0.0097	1.33	9172.41	0.29049	0.00268	0.92	2.54732
30	0.62205	0.62205	0.0061	1.34	9241.38	0.29268	0.00167	1.38	2.30388
30	0.64455	0.64455	0.0063	1.35	9310.34	0.29486	0.00172	1.38	2.30195

Polymer Store, Initial Run

Polymer Store

4-June-run-1

Constants:

Mach 2.92
T 110 K
R 287.05 J/kg*K
V 614 m/s
A_{ref} 6.63E-05 m²
D 21.75 mm

Dist. (mm)	Load Cell Load (g)	Free-stream Load (g)	Load (N)	Test Section Press. (psig)	Test Section Press. (Pa)	Density (kg/m ³)	C _{Dx}	Polymer Store, Run-1 Error	x/D	Polymer Store, Run-1 Error %
0	26	-26	-0.2550	1.29	8896.55	0.281755	-0.072426	0.00062	0.00	0.85052
5	9	-9	-0.0883	1.29	8896.55	0.281755	-0.025071	0.00017	0.23	0.67744
10	11	-11	-0.1079	1.29	8896.55	0.281755	-0.030642	0.0006	0.46	1.96866
15	13	-13	-0.1275	1.27	8758.62	0.277387	-0.036783	0.00063	0.69	1.70379
20	-35	35	0.3432	1.23	8482.76	0.26865	0.102253	0.00077	0.92	0.74827
25	-26	26	0.2550	1.28	8827.59	0.279571	0.072992	0.00134	1.15	1.83068
30	-49	49	0.4805	1.31	9034.48	0.286123	0.134411	0.00096	1.38	0.71533
35	-34	34	0.3334	1.25	8620.69	0.273018	0.097742	0.00079	1.61	0.8121

Dist. (mm)	Load Cell Error Load (g)	Free-stream Load (g)	Load (N)	Test Section Press. (psig)	Test Section Press. (Pa)	Density (kg/m ³)	C _{Dx}	Error	x/D
0	0.76253	0.76253	0.0075	1.29	8896.55	0.281755	0.002124	0.00062	0.00
5	0.21024	0.21024	0.0021	1.29	8896.55	0.281755	0.000586	0.00017	0.23
10	0.74673	0.74673	0.0073	1.29	8896.55	0.281755	0.00208	0.0006	0.46
15	0.76377	0.76377	0.0075	1.27	8758.62	0.277387	0.002161	0.00063	0.69
20	0.90308	0.90308	0.0089	1.23	8482.76	0.26865	0.002638	0.00077	0.92
25	1.64130	1.64130	0.0161	1.28	8827.59	0.279571	0.004608	0.00134	1.15
30	1.20866	1.20866	0.0119	1.31	9034.48	0.286123	0.003315	0.00096	1.38
35	0.95211	0.95211	0.0093	1.25	8620.69	0.273018	0.002737	0.00079	1.61

Polymer Store, Comparative Run-1

Polymer Store

4-June-run-2

Constants:

Mach 2.92
T 110 K
R 287.05 J/kg*K
V 614 m/s
A_{ref} 6.63E-05 m²
D 21.75 mm

Dist. (mm)	Load Cell Load (g)	Free-stream Load (g)	Load (N)	Test Section Press. (psig)	Test Section Press. (Pa)	Density (kg/m ³)	C _{Dx}	Polymer Store, Run-2 Error	x/D	Polymer Store, Run-2 Error %
0	4	-4	-0.0392	1.30	8965.52	0.283939	-0.011057	0.00069	0.00	6.24094
5	-7	7	0.0686	1.30	8965.52	0.283939	0.019349	0.0006	0.23	3.09029
10	1	-1	-0.0098	1.29	8896.55	0.281755	-0.002786	0.00073	0.46	26.1665
15	9	-9	-0.0883	1.30	8965.52	0.283939	-0.024878	0.00076	0.69	3.05538
20	-31	31	0.3040	1.27	8758.62	0.277387	0.087714	0.00105	0.92	1.20264
25	-32	32	0.3138	1.28	8827.59	0.279571	0.089836	0.00065	1.15	0.7187
30	-55	55	0.5394	1.29	8896.55	0.281755	0.153209	0.00083	1.38	0.54204
35	-31	31	0.3040	1.24	8551.72	0.270834	0.089836	0.00083	1.61	0.92736

Dist. (mm)	Load Cell Error Load (g)	Free-stream Load (g)	Load (N)	Test Section Press. (psig)	Test Section Press. (Pa)	Density (kg/m ³)	C _{Dx}	Error	x/D
0	0.8608	0.8608	0.0084	1.30	8965.52	0.283939	0.002379	0.00069	0.00
5	0.7459	0.7459	0.0073	1.30	8965.52	0.283939	0.002062	0.0006	0.23
10	0.9023	0.9023	0.0088	1.29	8896.55	0.281755	0.002513	0.00073	0.46
15	0.9482	0.9482	0.0093	1.30	8965.52	0.283939	0.002621	0.00076	0.69
20	1.2856	1.2856	0.0126	1.27	8758.62	0.277387	0.003638	0.00105	0.92
25	0.7930	0.7930	0.0078	1.28	8827.59	0.279571	0.002226	0.00065	1.15
30	1.0280	1.0280	0.0101	1.29	8896.55	0.281755	0.002864	0.00083	1.38
35	0.9913	0.9913	0.0097	1.24	8551.72	0.270834	0.002873	0.00083	1.61

Polymer Store, Comparative Run-2

Wednesday-Thursday, 9-10 May Wind Tunnel results

9-May-Calibrated-load-cell-run, short extender

Constants:

Mach 2.92
T 110 K
R 287.05 J/kg*K
V 614 m/s
A_{ref} 6.63E-05 m²

Dist. (mm)	Load Cell Load (g)	Freestream Load (g)	Load (N)	Test Section Press. (psia)	Test Section Press. (Pa)	Density (kg/m ³)	C _{Dx}	x/D	Average C _{Dx}	Error
-20.0	19	-19	-0.1863	1.36	9379.31	0.297044	-0.0502	-0.92	-0.05136	0.002
-20.0	19	-19	-0.1863	1.30	8965.52	0.283939	-0.05252	-0.46	-0.06606	0.007
-10.0	27	-27	-0.2648	1.36	9379.31	0.297044	-0.07134	-0.05	0.001256	0.002
-10.0	23	-23	-0.2256	1.36	9379.31	0.297044	-0.06077	0.00	0.023497	0.018
-1.0	0	0	0.0000	1.41	9724.14	0.307965	0	0.05	-0.0078	0.007
-1.0	-1	1	0.0098	1.43	9862.07	0.312333	0.002513	0.14	-0.01784	0.006
0.0	-13	13	0.1275	1.38	9517.24	0.301412	0.033851	0.46	-0.03125	0.000
0.0	-17	17	0.1667	1.39	9586.21	0.303596	0.043949	0.80	-0.0472	0.003
0.0	-15	15	0.1471	1.38	9517.24	0.301412	0.039059	0.92	-0.01044	0.005
0.0	0	0	0.0000	1.39	9586.21	0.303596	0	1.15	-0.07294	0.002
0.0	-2	2	0.0196	1.53	10551.72	0.334174	0.004697	1.29	-1.9E-05	0.004
0.0	-8	8	0.0785	1.48	10206.90	0.323254	0.019424	1.38	0.116434	0.019
1.0	5	-5	-0.0490	1.38	9517.24	0.301412	-0.01302	1.52	0.120682	0.007
1.0	1	-1	-0.0098	1.39	9586.21	0.303596	-0.00259			
3.0	9	-9	-0.0883	1.34	9241.38	0.292676	-0.02414			
3.0	5	-5	-0.0490	1.35	9310.34	0.29486	-0.01331			
3.0	6	-6	-0.0588	1.34	9241.38	0.292676	-0.01609			
10.0	12	-12	-0.1177	1.38	9517.24	0.301412	-0.03125			
10.0	12	-12	-0.1177	1.38	9517.24	0.301412	-0.03125			
17.5	19	-19	-0.1863	1.38	9517.24	0.301412	-0.04948			
17.5	17	-17	-0.1667	1.36	9379.31	0.297044	-0.04492			
20.0	6	-6	-0.0588	1.38	9517.24	0.301412	-0.01562			
20.0	5	-5	-0.0490	1.37	9448.28	0.299228	-0.01311			
20.0	5	-5	-0.0490	1.38	9517.24	0.301412	-0.01302			
20.0	2	-2	-0.0196	1.37	9448.28	0.299228	-0.00525			
20.0	2	-2	-0.0196	1.38	9517.24	0.301412	-0.00521			
25.0	28	-28	-0.2746	1.35	9310.34	0.29486	-0.07453			
25.0	27	-27	-0.2648	1.36	9379.31	0.297044	-0.07134			
28.0	-1	1	0.0098	1.37	9448.28	0.299228	0.002623			
28.0	1	-1	-0.0098	1.35	9310.34	0.29486	-0.00266			
30.0	-40	40	0.3923	1.40	9655.17	0.305781	0.10267			
30.0	-50	50	0.4903	1.38	9517.24	0.301412	0.130197			
33.0	-47	47	0.4609	1.39	9586.21	0.303596	0.121505			
33.0	-49	49	0.4805	1.36	9379.31	0.297044	0.12947			
33.0	-45	45	0.4413	1.38	9517.24	0.301412	0.117178			
33.0	-44	44	0.4315	1.38	9517.24	0.301412	0.114574			

First Calibrated Load Cell Run.

Saturday, 12 May, Wind Tunnel results

Series-Run-1, short extender

Constants:

Mach 2.92
T 110 K
R 287.05 J/kg*K
V 614 m/s
A_{ref} 6.63E-05 m²

Dist. (mm)	Load Cell Load (g)	Freestream Load (g)	Load (N)	Test Section Press. (psia)	Test Section Press. (Pa)	Density (kg/m ³)	C _{Dx}	x/D	Average C _{Dx}	Error
15.0	23	-23	-0.22555	1.24	8551.724	0.270834	-0.06665	0.69	-0.05651	0.014
15.0	16	-16	-0.15691	1.24	8551.724	0.270834	-0.04637	0.78	-0.0689	0.005
17.0	24	-24	-0.23536	1.19	8206.897	0.259913	-0.07247	0.87	-0.07703	0.009
17.0	22	-22	-0.21575	1.21	8344.828	0.264282	-0.06534	0.97	-0.08223	0.010
19.0	29	-29	-0.28439	1.25	8620.69	0.273018	-0.08337	1.06	-0.08839	0.010
19.0	24	-24	-0.23536	1.22	8413.793	0.266466	-0.07069	1.15	-0.07331	0.006
21.0	31	-31	-0.30401	1.25	8620.69	0.273018	-0.08912	1.24	-0.06637	0.004
21.0	26	-26	-0.25497	1.24	8551.724	0.270834	-0.07535	1.33	-0.07709	0.006
23.0	33	-33	-0.32362	1.24	8551.724	0.270834	-0.09563	1.43	-0.05361	0.002
23.0	28	-28	-0.27459	1.24	8551.724	0.270834	-0.08114	1.52	-0.06305	0.006
25.0	27	-27	-0.26478	1.25	8620.69	0.273018	-0.07762			
25.0	24	-24	-0.23536	1.25	8620.69	0.273018	-0.06899			
27.0	24	-24	-0.23536	1.25	8620.69	0.273018	-0.06899			
27.0	22	-22	-0.21575	1.24	8551.724	0.270834	-0.06375			
29.0	28	-28	-0.27459	1.24	8551.724	0.270834	-0.08114			
29.0	25	-25	-0.24517	1.23	8482.759	0.26865	-0.07304			
31.0	19	-19	-0.18633	1.24	8551.724	0.270834	-0.05506			
31.0	18	-18	-0.17652	1.24	8551.724	0.270834	-0.05216			
33.0	23	-23	-0.22555	1.23	8482.759	0.26865	-0.06719			
33.0	20	-20	-0.19613	1.22	8413.793	0.266466	-0.05891			

Verification Series Run-1

Sunday-Monday, 13-14 May, Wind Tunnel results
 Series-Run-2, short extender

Constants:

Mach 2.92
 T 110 K
 R 287.05 J/kg*K
 V 614 m/s
 A_{ref} 6.63E-05 m²

Dist. (mm)	Load Cell Load (g)	Freestream Load (g)	Load (N)	Test Section Press. (psia)	Test Section Press. (Pa)	Density (kg/m ³)	C_{Dx}	x/D	Average C_{Dx}	Error
15.0	6	-6	-0.05884	1.26	8689.655	0.275202	-0.01711	0.69	-0.01417	0.004
15.0	4	-4	-0.03923	1.28	8827.586	0.279571	-0.01123	0.78	-0.04416	0.006
17.0	16	-16	-0.15691	1.18	8137.931	0.257729	-0.04872	0.87	-0.06296	0.007
17.0	13	-13	-0.12749	1.18	8137.931	0.257729	-0.03959	0.97	-0.07219	0.007
19.0	22	-22	-0.21575	1.17	8068.966	0.255545	-0.06757	1.06	-0.06508	0.001
19.0	19	-19	-0.18633	1.17	8068.966	0.255545	-0.05836	1.15	-0.06293	0.002
21.0	24	-24	-0.23536	1.28	8827.586	0.279571	-0.06738	1.24	-0.05154	0.000
21.0	27	-27	-0.26478	1.26	8689.655	0.275202	-0.077	1.33	-0.04294	0.004
23.0	23	-23	-0.22555	1.28	8827.586	0.279571	-0.06457	1.43	-0.03255	0.002
23.0	23	-23	-0.22555	1.26	8689.655	0.275202	-0.06559	1.52	-0.03018	0.002
25.0	22	-22	-0.21575	1.29	8896.552	0.281755	-0.06128			
25.0	23	-23	-0.22555	1.28	8827.586	0.279571	-0.06457			
27.0	18	-18	-0.17652	1.25	8620.69	0.273018	-0.05175			
27.0	18	-18	-0.17652	1.26	8689.655	0.275202	-0.05133			
29.0	16	-16	-0.15691	1.26	8689.655	0.275202	-0.04563			
29.0	14	-14	-0.13729	1.25	8620.69	0.273018	-0.04025			
31.0	12	-12	-0.11768	1.26	8689.655	0.275202	-0.03422			
31.0	11	-11	-0.10787	1.28	8827.586	0.279571	-0.03088			
33.0	11	-11	-0.10787	1.25	8620.69	0.273018	-0.03162			
33.0	10	-10	-0.09807	1.25	8620.69	0.273018	-0.02875			

Verification Series Run-2

Run-1, Monday 14 May
6-stage-analysis-Run-1, short extender

Constants:

Mach 2.92
T 110 K
R 287.05 J/kg*K
V 614 m/s
A_{ref} 6.63E-05 m²

Dist. (mm)	Load Cell Load (g)	Freestream Load (g)	Load (N)	Test Section Press. (psia)	Test Section Press. (Pa)	Density (kg/m ³)	C _{Dx}	x/D	Average C _{Dx}	Error
-20.0	28.00	-28.00	-0.2746	1.27	8758.621	0.2774	-0.0792	-0.92	-0.07923	0.000
-20.0	28.00	-28.00	-0.2746	1.27	8758.621	0.2774	-0.0792	-0.46	-0.06791	0.000
-10.0	24.00	-24.00	-0.2354	1.27	8758.621	0.2774	-0.0679	0.00	-0.07492	0.001
-10.0	24.00	-24.00	-0.2354	1.27	8758.621	0.2774	-0.0679	0.46	-0.05113	0.000
0.0	25.00	-25.00	-0.2452	1.19	8206.897	0.2599	-0.0755	0.92	-0.0492	0.001
0.0	24.00	-24.00	-0.2354	1.16	8000	0.2534	-0.0743	1.38	-0.01437	0.000
10.0	18.00	-18.00	-0.1765	1.27	8758.621	0.2774	-0.0509	1.52	-0.01324	0.002
10.0	18.00	-18.00	-0.1765	1.26	8689.655	0.2752	-0.0513			
20.0	16.00	-16.00	-0.1569	1.18	8137.931	0.2577	-0.0487			
20.0	17.00	-17.00	-0.1667	1.23	8482.759	0.2687	-0.0497			
30.0	5.00	-5.00	-0.049	1.25	8620.69	0.273	-0.0144			
30.0	5.00	-5.00	-0.049	1.25	8620.69	0.273	-0.0144			
33.0	5.00	-5.00	-0.049	1.26	8689.655	0.2752	-0.0143			
33.0	5.00	-5.00	-0.049	1.27	8758.621	0.2774	-0.0141			
33.0	4.00	-4.00	-0.0392	1.27	8758.621	0.2774	-0.0113			

6 Stage Analysis Run

Original Strut Configuration, Entire Store				
Stage	x/D	C _{Fx}	C _{Fy}	C _{Fz}
1	0.14	0.05875	-0.45100	-0.00261
2	0.80	0.12160	-0.02823	-0.00736
3	1.61	0.18400	-0.04640	0.00667

New Strut Configuration, Entire Store				
Stage	x/D	C _{Fx}	C _{Fy}	C _{Fz}
1	0.14	0.05276	-0.02027	-0.00080
2	0.80	0.14486	-0.01224	0.00196
3	1.61	0.17353	-0.04540	0.01032

Original Strut Configuration, Store Tip				
Stage	x/D	C _{Fx}	C _{Fy}	C _{Fz}
1	0.14	-0.03712	-0.02726	-0.00381
2	0.80	0.01470	-0.02070	-0.00329
3	1.61	0.11760	-0.04710	0.00759

New Strut Configuration, Store Tip				
Stage	x/D	C _{Fx}	C _{Fy}	C _{Fz}
1	0.14	-0.03686	-0.00450	-0.00105
2	0.80	0.01667	-0.00428	0.00124
3	1.61	0.10542	-0.03652	0.01108

Simko: Original Strut, Solid Cone					
Stage	x/D	B-L: C _{Fy}	DES: C _{Fy}	B-L: C _{Fz}	DES: C _{Fz}
1	0.22	-0.040847	-0.043723	0.002015	0.009159
2	0.92	-0.085526	-0.107020	0.001600	0.001493
3	2.23	-0.790250	-0.033413	-0.005707	-0.000644

Collective CFD Data

Store without Cone analysis

No Cone

Constants:

Mach 2.92
T 110 K
R 287.05 J/kg*K
V 614 m/s
A_{ref} 6.63E-05 m²

Theoretical Values:

P_{Tc}/P_c 21.579
P_c/P_∞ 1.53
A_{ref} 5.4E-05 m²

Config.	Load Cell Load (g)	Free stream Load (g)	Load (N)	Test Section Press. (psia)	Test Section Press. (Pa)	Density (kg/m ³)	C _{Dx}	Wind Tunnel Press. Setting (psig)	Average C _{Dx}	Store-only Error
1.0	-25	25	0.2452	1.32	9103.45	0.2883	0.0681	24.0	0.0758	0.011
1.0	-30	30	0.2942	1.29	8896.55	0.2818	0.0836	24.0	0.1234	0.0039
2.0	-46	46	0.4511	1.31	9034.48	0.2861	0.1262	24.0	0.0854	0.0015
2.0	-44	44	0.4315	1.31	9034.48	0.2861	0.1207	10.0	0.0815	0.0016
3.0	-31	31	0.3040	1.32	9103.45	0.2883	0.0844	10.0	0.1501	0.009
3.0	-32	32	0.3138	1.33	9172.41	0.2905	0.0865	10.0	0.2093	0.0209
4.0	-20	20	0.1961	0.87	6000	0.19	0.0826	38.0	0.1228	0.0004
4.0	-19	19	0.1863	0.85	5862.07	0.1857	0.0803	38.0	0.1945	0.0191
5.0	-37	37	0.3628	0.85	5862.07	0.1857	0.1564	38.0	0.0954	0.0043
5.0	-34	34	0.3334	0.85	5862.07	0.1857	0.1437			
6.0	-46	46	0.4511	0.85	5862.07	0.1857	0.1945			
6.0	-53	53	0.5198	0.85	5862.07	0.1857	0.2241			
7.0	-49	49	0.4805	1.43	9862.07	0.3123	0.1231			
7.0	-45	45	0.4413	1.32	9103.45	0.2883	0.1225			
8.0	-67	67	0.6570	1.33	9172.41	0.2905	0.1810			
8.0	-77	77	0.7551	1.33	9172.41	0.2905	0.2080			
9.0	-37	37	0.3628	1.35	9310.34	0.2949	0.0985			
9.0	-36	36	0.3530	1.40	9655.17	0.3058	0.0924			

Theory

24.00	-	-	0.25795	1.3133	9057.47	0.2869	0.0888
10.00	-	-	0.16760	0.85	5885.06	0.1864	0.0888
38.00	-	-	0.26711	1.36	9379.31	0.297	0.0888

1, Long, Poly 24psig
2, Long, Metal 24psig
3, Short, Metal 24psig
4, Long, Poly 10psig
5, Long, Metal 10psig
6, Short, Metal 10psig
7, Long, Poly 38psig
8, Long, Metal 38psig
9, Short, Metal 38psig

Runs without Cone (Store-only).

Bibliography

1. Anderson, Dale A. and others. *Computational Fluid Mechanics and Heat Transfer*. Hemisphere Publishing Corporation, 1984.
2. Anderson, John D. *Modern Compressible Flow with Historical Perspective*. 2nd Ed. McGraw-Hill, 1990
3. August, Henry and others. "Leeside Separation of Hypersonic Weapons." ADA318744: Hughes Aircraft, 1993.
4. August, Henry. "Novel Aerodynamic Designs of a Hypersonic Warfighter." AIAA Paper 2006-240.
5. Bjorge S. T., Reeder, M. F., Subramanian C., and Crafton J. *Flow Around an Object Projected From a Cavity into a Supersonic Freestream*. Technical Report 04-1253, Reno, NV: AIAA, Jan 2004.
6. "Bombing Anywhere On Earth in Less Than Two Hours." Space Daily, Nov 27, 2003. <http://www.spacedaily.com/news/rocketscience-03zzr.html>
7. Boswell B. A. and Dutton C. "Flow Visualizations and Measurements of a Three-Dimensional Supersonic Separated Flow," AIAA Journal, 39(1):113-121 (Jan 2001).
8. Boswell B. A. and Dutton C. "Velocity Measurements in a Three-Dimensional Compressible Base Flow," AIAA Paper 2002-0292.
9. Burt, M., P. Miller and J. Agrell. "Transonic and Supersonic Flowfield Measurements about Axisymmetric Afterbodies for Validation of Advanced CFD Codes." AGARD Conference Proceedings, CP-535:9-1 to 9-28 (July 1994).
10. Catalano, George D. and Sturek, Walter B. "A Numerical Investigation of Supersonic Flow Past an Aft Body." AIAA Paper 2000-4520.
11. Dayman, Bain Jr. *Free-Flight Hypersonic Viscous Effects on Slender Cones*. AIAA Journal Vol. 3, #8: 1392-1400 (August 1965).
12. Dayman, Bain Jr. *Optical Free-Flight Wake Studies*. JPL Technical Report 32-364. Pasadena, 1 October 1962.
13. Dayman, Bain Jr. *Simplified Free-Flight Testing in a Conventional Wind Tunnel*. JPL Technical Report 32-346. Pasadena, 1 November 1962.

14. Dayman, B. Jr. and Kurtz, D. W. "Forebody Effects on Drogue Drag in Supersonic Flow." *Journal of Spacecraft*, Vol. 5, No. 11: 1335-1340 (November 1968).
15. Dutton, J. C. and others. "Recent Progress on High-Speed Separated Base Flows." AIAA Paper 1995-0472.
16. De Feo, D. M. and Shaw, S. T. "Turbulence Modeling and Supersonic Base Flows." AIAA Paper 2007-1083.
17. Eckert, D. "Correction of Support Influences on Measurements with Sting Mounted Wind Tunnel Models." AGARD Conference Proceedings, CP-535: 31, 1-11 (July 1994).
18. Fluent, Inc., Lebanon, NH. *Fluent 6.2 User's Guide*, 2005.
19. Herrin, J. L. and Dutton, J. C. "Supersonic Base Flow Experiments in the Near Wake of a Cylindrical Afterbody." *AIAA Journal*, Vol. 32, #1: 77-83 (January 1994).
20. Janssen, J. R. and J. C. Dutton. "Time-Series Analysis of Supersonic Base-Pressure Fluctuations." *AIAA Journal*, Vol 42, #3: 605-613 (March 2004).
21. Jung, T. P. *Wind Tunnel Study of Interference Effects Relating to Aft Supersonic Ejection of a Store*. MS Thesis, Graduate School of Engineering, Air Force Institute of Technology (AETC), Wright-Patterson AFB, OH, Dec 2005. AFIT/GAE/ENY/05-04.
22. Jung, T.P. and Reeder, Mark F., Maple, Raymond C. "Wind Tunnel Study of Interference Effects Relating to Aft Supersonic Ejection of a Store."
23. Kastengren Alan J., Dutton J. Craig, Elliot, Gregory S. "Recompression Shock Unsteadiness in Supersonic Blunt-Base Cylinder Wakes." AIAA Paper 2005-315.
24. Kawai, Soshi and Fujii, Kozo. "Computational Analysis of the Characteristics of Subsonic, Transonic and Supersonic Base Flows." AIAA Paper 2005-5156.
25. Liever, Peter A., Engelund, Walter C. and others. "Stage Separation Analysis of the X-43A Research Vehicle." AIAA Paper 2004-4725.
26. Martellucci, A. and A. Agnone. "Measurements of the Turbulent Near Wake of a Cone at Mach 6," *AIAA Journal*, Vol. 4, #3: 385-391 (March 1966).

27. Mather, T. and J. C. Dutton. "Base Bleed Experiments with a Cylindrical Afterbody in Supersonic Flow." AIAA 95-0062, January 1995.
28. Menezes V., Takayama K. and others. "Drag Reduction by Controlled Base Flow Separation." Journal of Aircraft Vol. 43, No. 5 (September –October 2006).
29. Newman, Gary and others. "On the Aerodynamics/Dynamics of Store Separation from Hypersonic Aircraft." AIAA Paper 1992-2722.
30. Nichols R. H. and others. "Calculation of High Speed Base Flows." AIAA Paper 92-2679-CP, (pgs. 614-623).
31. Ottens, H.B.A. and others. "Computational Study of Support Influence on Base Flow of a Model in Supersonic Flow". AIAA Paper 2001-2638.
32. Ober, Curtis C., Kiehne Thomas M. and others. "A Computational Study of the Aerodynamics of a Body Immersed in a Supersonic Wake." AIAA Paper 94-3519 (pgs. 506-516).
33. Paciorri, Renato and others. "Evaluation of Turbulence Modeling in Supersonic Afterbody Computations." AIAA Paper 2001-3039 (June 2001).
34. Peltier, Donald Wallace. "Performing Particle Image Velocimetry in a Supersonic Wind Tunnel Using Carbon Dioxide as the Seed Material." MS Thesis, Graduate School of Engineering, Air Force Institute of Technology (AETC), Wright-Patterson AFB, OH, Mar 2006. AFIT/GAE/ENY/07-J17.
35. Persson, Mathias and Rizzi, Arthur. "Aerodynamics of Hypervelocity Missiles." <http://www.psci.kth.se/prog.rep./12.pdf#search=%22%22Aerodynamics%20of%20Hypervelocity%20Missiles%22%22>
36. Prewitt N. C., Belk D. M., and Maple R. C. "Multiple-Body Trajectory Calculations Using the Beggar Code," Journal of Aircraft, 36(5):802-808 (Sep 1999).
37. Rizzetta, Donald P., Visbal, Miguel R. "Large-Eddy Simulation of Supersonic Cavity Flowfields Including Flow Control." AIAA Journal, Vol. 41, #8: 1452 (Aug 2003).
38. Simko, R. J. *Store Separations From a Supersonic Cone*. MS Thesis, Graduate School of Engineering, Air Force Institute of Technology (AETC), Wright-Patterson AFB, OH, Mar 2006. AFIT/GAE/ENY/06-M29.

39. Stallings, Robert L. Jr., Plentovich, Elizabeth B. and others. "Effect of Passive Venting on Static Pressure Distributions in Cavities at Subsonic and Transonic Speeds." NASA Technical Memorandum 4549 (June 1994).
40. "Statement of General Lance Lord at Hearings on FY 2006 Defense Authorization Budget Request for Space Activities."
<http://www.spaceref.com/news/viewstr.html?pid=15798>
41. Sahu Jubaraj, Nietubicz Charles J. "Application of Chimera Technique to Projectiles in Relative Motion." AIAA Paper 93-3632-CP.
42. Tucker, P. Kevin and Shyy, Wei. "A Numerical Analysis of Supersonic Flow over an Axisymmetric Afterbody." AIAA Paper 93-2347.
43. Huwaldt, Joseph A. "Supersonic Cone Program." 30 April, 2005.
<http://homepage.mac.com/jhuwaldt/java/Applications/SupersonicCone/index.html>
44. Wilcox, F. Jr. "Tangential, Semisubmerged, and Internal Store Carriage and Separation at Supersonic Speeds." AIAA Paper 91-0198.
45. Wilcox, D. C. *Turbulence Modeling for CFD*. DCW Industries Inc., November 2006.
46. Kiemele, Mark J. and Schmidt, Stephen R. *Basic Statistics: Tools for Continuous Improvement*. Air Academy Press, 1990.

Vita

Captain Burkinshaw graduated from Jordan-Elbridge High School, Jordan New York in 1996 in the top 10% of his class. He attended Syracuse University and graduated in May of 2001 with a Bachelor of Science degree in Aerospace Engineering. While at Syracuse University, Captain Burkinshaw was a member of the Air Force Reserve Officer Training Corps. and advanced to the position of Vice Commander. Captain Burkinshaw's first assignment was at the Air Logistics Center, Tinker Air Force Base. There he was assigned to the Propulsion Product Group Manager's Staff and later the F-15/F-16 Fighter Propulsion Directorate. Upon completion of his Master's degree in Aeronautical Engineering, Captain Burkinshaw will be assigned to the Computational Sciences Branch, Air Force Research Laboratory.

REPORT DOCUMENTATION PAGE				Form Approved OMB No. 074-0188	
<p>The public reporting burden for this collection of information is estimated to average 1 hour per response, including the time for reviewing instructions, searching existing data sources, gathering and maintaining the data needed, and completing and reviewing the collection of information. Send comments regarding this burden estimate or any other aspect of the collection of information, including suggestions for reducing this burden to Department of Defense, Washington Headquarters Services, Directorate for Information Operations and Reports (0704-0188), 1215 Jefferson Davis Highway, Suite 1204, Arlington, VA 22202-4302. Respondents should be aware that notwithstanding any other provision of law, no person shall be subject to a penalty for failing to comply with a collection of information if it does not display a currently valid OMB control number.</p> <p>PLEASE DO NOT RETURN YOUR FORM TO THE ABOVE ADDRESS.</p>					
1. REPORT DATE (DD-MM-YYYY) 14-06-2007		2. REPORT TYPE Master's Thesis		3. DATES COVERED (From – To) Nov 2006 – Sept 2007	
4. TITLE AND SUBTITLE COMPARATIVE STUDY OF AERODYNAMIC INTERFERENCE DURING AFT DISPENSE OF MUNITIONS				5a. CONTRACT NUMBER	
				5b. GRANT NUMBER	
				5c. PROGRAM ELEMENT NUMBER	
6. AUTHOR(S) Burkinshaw, Matthew G., Captain, USAF				5d. PROJECT NUMBER JON 06-159	
				5e. TASK NUMBER	
				5f. WORK UNIT NUMBER	
7. PERFORMING ORGANIZATION NAMES(S) AND ADDRESS(S) Air Force Institute of Technology Graduate School of Engineering and Management (AFIT/EN) 2950 Hobson Way, Building 640 WPAFB OH 45433-8865				8. PERFORMING ORGANIZATION REPORT NUMBER AFIT/GAE/ENY/07-J03	
9. SPONSORING/MONITORING AGENCY NAME(S) AND ADDRESS(ES) Mr. Rudy Johnson - AFRL/VAAI 2130 8 th Street, Bldg 45, room 228 Wright Patterson AFB, OH 45431				10. SPONSOR/MONITOR'S ACRONYM(S) AFRL/VAAI	
				11. SPONSOR/MONITOR'S REPORT NUMBER(S)	
12. DISTRIBUTION/AVAILABILITY STATEMENT APPROVED FOR PUBLIC RELEASE; DISTRIBUTION UNLIMITED.					
13. SUPPLEMENTARY NOTES					
<p>14. ABSTRACT Based on forthcoming USAF needs, an investigation was launched to further the understanding of aft dispense of munitions in a high-speed environment. A computational fluid dynamics (CFD) study was performed followed by a wind tunnel experiment. The study consisted of a strut-mounted cone simulating a parent vehicle and a sting mounted cone-cylinder store situated directly behind the cone. The CFD modeled the test objects inside a supersonic wind tunnel in which the experiments took place. The CFD study consisted of evaluating a new strut designed to reduce asymmetry in the airflow aft of the cone. The CFD study also included predictions of axial loads acting on the store in various locations behind the cone. The experimental study consisted of implementing the new strut and introducing a miniature load cell for comparison to CFD load predictions. The CFD study indicated the newly designed strut lengthened the cone's base region by 27% and reduced transverse forces acting on the store by as much as 50% in two of the three locations evaluated. The experimental studies were successful in obtaining axial force coefficients that matched the CFD trend and were typically within 30% of the magnitudes. It was concluded that the load cell was generally adequate in measuring the axial loading on the store though its accuracy is less than that of a typical wind tunnel balance. The error trends indicate that the polymer store introduces the least amount of statistical error making it the most accurate representation of the results. Significant sources of error include transverse vibrations and axial buffeting observed in the wind tunnel tests.</p>					
15. SUBJECT TERMS Supersonic, store, munitions, aft dispense, aerodynamic, interference, CFD, wind tunnel, experimental, load.					
16. SECURITY CLASSIFICATION OF:			17. LIMITATION OF ABSTRACT	18. NUMBER OF PAGES	19a. NAME OF RESPONSIBLE PERSON
a. REPORT	b. ABSTRACT	c. THIS PAGE			19b. TELEPHONE NUMBER (Include area code)
U	U	U	UU	173	Raymond C. Maple, Lt Col, USAF (937) 255-3636, ext 4577 (Raymond.Maple@afit.edu)